Thermal Fatigue
in Stationary Aluminium Contacts

by

Christopher Ruppert

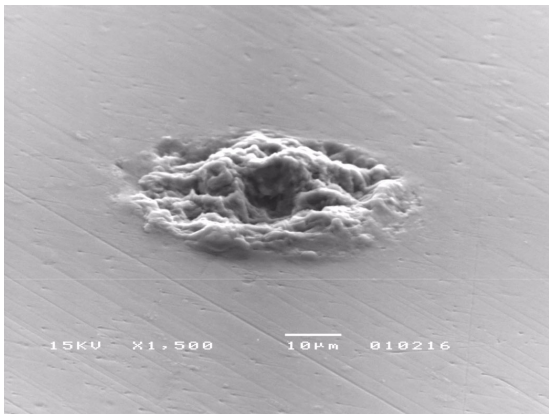

A dissertation submitted to

the Norwegian University of Science and Technology
Department of Electrical Power Engineering

in partial fulfilment of the
requirements for the degree of
doktor ingeniør

December 2001

Preface

This thesis is part of a research program initiated to promote further understanding of basic principles in power engineering. The project was financed by the Norwegian Research Council and all the work was done at the Department of Electrical Power Engineering at the Norwegian University of Science and Technology (NTNU).

The work was carried out under the supervision of Professor Magne Runde (NTNU) and Professor emeritus Jarle Sletbak (NTNU). I would like to extend my gratitude to both of them for being a constant source of inspiration. The practical advice from Pål Ulseth at the Department of Materials Science of SINTEF regarding the preparation of embedded specimens and metallographic imaging should also be acknowledged, as well as the assistance of the technical staff at NTNU in manufacturing the specimens.

Finally, I would like to thank all my friends and colleagues at the Department of Electrical Power Engineering at NTNU and at the Department of Materials Science at SINTEF for creating a stimulating and friendly atmosphere.

Trondheim, December 2001

Christopher Ruppert

Abstract

The conductive area of a stationary electrical contact consists of many small contact spots. The contact spots can be described as narrow metal bridges across the interface between two conductors. Deterioration of a contact is closely related to processes occurring in these microscopic areas. The objective of this work is to clarify the basic mechanisms affecting the reliability and degradation of an electrical contact by closely studying the contact spots.

Particular emphasis has been put on examining the contact spots occurring in aluminium-aluminium interfaces when passing AC. Due to the small thermal capacity of a contact spot the temperature in the contact spot cycles with twice the frequency of the applied AC. The minimum temperature attained during one cycle being the bulk temperature of the conductor, the maximum temperature can in heavily stressed contacts be close to the melting point of the conductor material. In the idealized contact used in the present investigation, this thermal cycling may initiate thermal fatigue processes in the contact spot region.

Microscopic cracks appear in the contact spot region as the result of thermal fatigue processes. The cracks not only lower the mechanical strength of the conductor in close vicinity of the contact spot, they also cause a higher electrical resistivity in these areas.

Alloying a tracer metal in one of the electrodes of the contact allows for closer investigation of the crack propagation as it occurred during the experiments. The tracer migrates into the heated contact spot region of the opposite electrode where the cracks constitute a barrier impairing further diffusion into the electrode. Further information on the thermal fatigue processes in the contact spot region is obtained when examining metallographic images of cross sectioned contact spots. Here it can be seen that the repetitive thermal stresses give rise to clearly localized recrystallisation in the contact spot region.

Thermal fatigue is a well known failure mechanism in mechanical structures. It has to the authors knowledge not previously been associated with the deterioration of contact spots. However, the mechanical damage in the contact spot region caused by the temperature cycling also has a detrimental effect on the electrical behaviour of the contact. It is therefore suggested that thermal fatigue is of considerable importance to the reliability and degradation of stationary electrical contacts.

Contents

List of symbols and abbreviations

a	contact spot radius
A_0	equipotential surface in contact spot
A_a	apparent contact area
A_b	load bearing area
A_c	conducting area
A_t	theoretically determined A_c
A_e	experimentally determined A_c
A_e	equipotential surface distant from contact spot
b	Burgers-vector
b	fatigue strength exponent
c	specific heat
c	fatigue ductility exponent
e	electron charge
E	electric field
E	modulus of elasticity
f_S	sampling frequency
H	hardness
I	current (amplitude)
J	current density
l	length
L	Lorentz-constant
m_e	mass of an electron
n	number of electrons per volume
n	hardening coefficient
N_f	cycles to failure
p	Joule heat
P	mechanical load
r	radius
Q	heat flux
R	Holm-radius
R_c	contact resistance
R_S	series resistor
T	absolute temperatur
T_0	bulk temperature
T_R	temperature of recrystallisation
T_M	melting temperature

T_Θ	temperature in the contact spot
U_c	voltage across the contact
U_m	melting voltage
U_s	softening voltage
V	volume
α	temperature coefficient of electrical resistivity
α	semi-axis of ellipse
β	semi-axis of ellipse
γ	ellipticity
γ_l	linear thermal expansion coefficient
γ_v	coefficient of thermal expansion (volume)
ε	strain
$\dot{\varepsilon}$	strain rate
ε'_f	fatigue ductility coefficient
ϑ	supertemperature
Θ	supertemperature in the contact spot
λ	thermal conductivity
λ_0	thermal conductivity distant from contact spot
μ	ellipsoid parameter
μ	electron mobility
ρ	electrical resistivity
ρ_0	electrical resistivity distant from contact spot
σ	electrical conductivity
σ	stress
σ_g	endurance limit
σ_m	ultimate strength
σ_r	rupture strength
σ_y	yield strength
σ'_f	fatigue strength coefficient
τ	thermal time constant
τ_{SC}	time between two scattering processes
Φ	electric potential
EDA	energy dispersive analysis
HAZ	heat affected zone
HF	high frequency
SEM	scanning electron microscope

1

Introduction

Electrical contacts are of far greater importance in the field of electrical engineering than it might be expected regarding the volume of production as well as revenue, mainly due to the fact that electrical contacts are the weak point in many electrical installations. This holds for any conceivable kind of electrical contact independent of the voltage rating of the device, its material and holds also across the basic classification in stationary, switching or moving contacts. This is in particular remarkable, as the major task of all contact configurations is only to pass electric current from one conductor to another conductor via the interface between them. Generally, it is not very difficult to establish a sufficiently good electrical contact between two conductors. However, it is a challenging exercise to make the contact simple and inexpensive and at the same time reliable over many years.

When mating two electrical conductors the actual electrical contact is established in microscopic areas of metal-to-metal connection, usually referred to as contact spots. It is the processes and phenomena occuring in the microscopic contact spots that are of great importance regarding the electrical behaviour and degradation of the contact. The nature of the degradation mechanisms is very complex, involving aspects of surface chemistry, metallurgy, elasticity theory, thermodynamics and other fields. Continuous exposure of the contact to corrosive environment, thermal or mechanical stresses may cause the contact spots to deteriorate, which in turn results in unacceptable high electrical resistance across the contact.

The intention of the present work is to closely examine processes contributing to the deterioration of contact spots in stationary electrical contacts between aluminium conductors when carrying AC. Aluminium as an electrical conductor is mainly used in transmission lines, cables and bus bars in power engineering applications, but also in the interconnects of integrated circuits and other applications. Amongst the most outstanding advantages of aluminium for electrical engineering purposes are its low density combined with a favourable cost-to-conductivity-ratio and its ability to withstand corrosion. Problematic, on the other hand, are the oxide layer covering the conductor and its ductility, in particular when establishing stationary contacts. The widespread use of aluminium as an electrical conductor and the inherent problems were the reason for choosing aluminium as the subject for the experimental work.

The report begins with an introduction to the theory of stationary electrical contacts followed by a brief review of the essential theory of thermal fatigue in aluminium (Chapter 2). Then a detailed description of the experimental setup is given in Chapter 3. The experimental results are presented in Chapter 4, subdivided into the documentation of the data recorded during the experiments and the presentation of the subsequent SEM and metallographic examinations of the contact spots. An extensive discussion of the validity and significance of the results from the present work follows in Chapter 5. Here the novel approach of thermal fatigue in the contact spot contributing to the degradation of stationary contacts is related to comparable previous findings and practical contact applications. Concluding remarks completing the report follow in chapter 6.

Parts of this work have been published earlier. Chapters 4 and 5 contain excerpts which have been presented in [1].

2

Theoretical Background

2.1 Theory of stationary electrical contacts

2.1.1 The contact surface

The main purpose of a stationary electrical contact is to pass a current between two electrodes as if they were a continuous conductor. The ideal electrical contact would have a resistance corresponding to the bulk resistance of the electrodes. This chapter is meant to give a concise description of the basic theory behind stationary electrical contacts. If not otherwise indicated most of the information given below is taken from Holm's book [2].

When mating two electrodes in order to form an electrical contact the size of the actually conducting metal-to-metal area is by far less than the so called apparent contact area A_a. The apparent contact area is that part of the electrode surface which appears to be in physical contact with the mating electrode. The fact that the area of physical contact is considerably smaller than A_a is due to micro asperities as they appear on every surface - even if it is polished to a high degree. When joining two conductors the physical contact between them is determined by the number of micro asperities on the opposite surfaces touching each other. The combined surface of all micro asperites in physical contact is called the load bearing area A_b. It is only a fraction of the apparent contact area and can be related to the mechanical load P on the electrodes as follows:

$$A_b \sim P / H \tag{2.1}$$

where H is the hardness of the electrode material. It can be seen from (2.1) that given a certain hardness H the load bearing area increases with the mechanical load on the electrodes as the micro-asperities become deformed under the pressure.

The actually conducting metal-to-metal area A_c is considerably smaller than the load bearing area A_b when taking insulating films on the electrodes into consideration. This might be a thin oxide-layer covering the electrodes as in the

case of e. g. aluminium conductors. Oxide film covered micro asperities in physical contact with its corresponding counterpart on the surface of the opposite electrode only contribute to A_c if the oxide film is broken such that metal-to-metal contact is established. These metal bridges connecting the electrodes are commonly referred to as contact spots or a-spots. This is shown schematically in Fig 2.1. Most contacts are expected to have many contact spots.

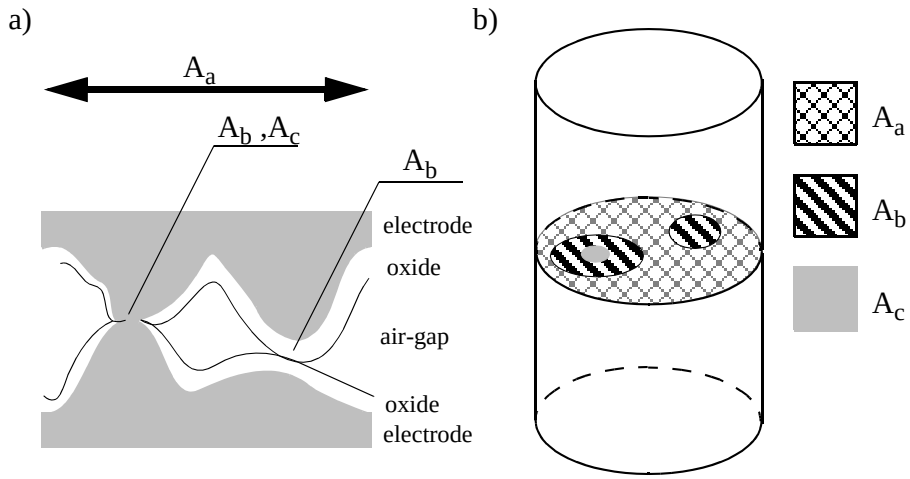

Figure 2.1: Schematic representation of a contact interface
a) Cross-section of surface asperities of oxide covered electrodes. The vertical scale is exaggerated.
b) Transparent cylindrical electrodes in contact. A_c can be seen to be only a minor fraction of A_b, resp. A_a.

The oxide film usually present on aluminium electrodes can be broken in several ways: either by mechanical or by electrical stress. Mechanical rupturing of the oxide film occurs when the load bearing asperities as mentioned above are deformed sufficiently, such that the brittle oxide film covering them cracks locally. This is due to the fact that the rather soft aluminium gives little support to a surface film which is much harder and less ductile. The oxide film breaks into many small flake-like pieces leaving an irregular pattern of minuscule cracks. It has been shown [3] that the underlying aluminium is squeezed through the cracks. When this then meets with aluminium squeezed through cracks on the opposing electrode a metal-to-metal contact is established.

The electrical breaking of the oxide film is called fritting. Here two mechanisms have to be distinguished: A-fritting and B-fritting.

A-fritting of the insulating oxide film with aluminium electrodes appears when the electric field E across the film increases to values in the order of 10^8 V/m. The oxide film on aluminium being usually about 10 nm thick this field is reached with a fritting voltage in the order of 1 V applied to the electrodes. A-fritting starts with the injection of electrons into the insulating film by field emission at one point of the electrode surface. The injected electrons produce a current flow within a narrow path through the film. The cohesion of the film along this path is diminished resulting in a channel crossing the oxide. Molten metal is then attracted into the channel and a contact spot is created. The contact spot subsequently widens with increasing current. This is due to electromechanical forces on the oxide. The process of widening of an existing contact spot is referred to as B-fritting.

2.1.2 The contact resistance

The contact resistance is the resistance as it originates from the fact that the current is forced to pass through the very small actual metallic contact area A_c, in addition to the resistance of the electrodes. The contact resistance depends on the number, the dimensions and the condition of the deformed micro-asperities contributing to A_c. Several types of electrical contacts have to be considered:

Metallic contacts: Both electrodes are in immediate physical contact. The current flow lines in the electrode distant from the contact spot are assumed to be parallel. Close to the contact spot the current flow lines are bent together as shown in Fig. 2.2 This then leads to the constriction resistance as described in detail below.

Quasimetallic contact: In this case the electrodes are covered with an extremely thin film, e.g. an oxide, less than 2 nm thick separating the electrodes such that no metallic contact can be made. These films can easily be penetrated by the electrons due to the tunnel-effect. Thus the contribution to the contact resistance originating from the presence of these extremely thin films is negligible.

Contacts with an electrically conductive layer: Electrodes often are prone to surface contamination resulting in a film of higher resistivity covering the electrode, as e. g. when exposed to a corrosive environment. The thickness of these layers might be in the order of a few hundred nanometer. The resistance arising from such contaminant layers has to be added to the constriction resistance.

An electrical contact between aluminium electrodes is a typical example of a metallic contact. It is of no importance whether the metallic contact was made by

mechanically rupturing the oxide film or by fritting. The sizes of the contact spots connecting the electrodes are usually minute, perhaps only a few micrometer across.

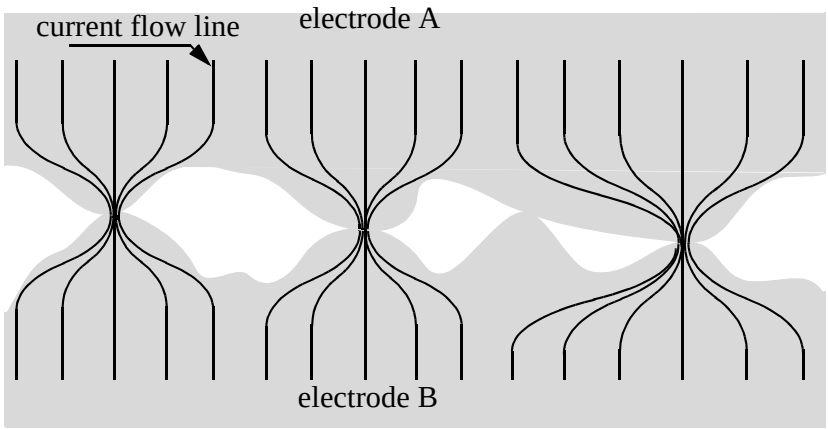

Figure 2.2: The current flow lines are bent together when close to the contact spot. The constriction resistance is due to this effect

The constriction resistance R_c is due to the concentration of current flow lines in the bulk electrode material (see Fig. 2.2). It may be calculated for an idealized circular contact spot of radius a as follows [2], [4]:

$$R_c = (\rho/2\pi a)\cdot \mathrm{atan}(\mu/a) \tag{2.2}$$

The parameter μ identifies the ellipsoidal surface as shown in Fig. 2.3. Equation 2.2 gives the constriction resistance as it appears in the bulk of one electrode. In the case of a long constriction ($\mu \to \infty$) (2.2) becomes

$$R_c = \rho/4a \tag{2.3}$$

As this only describes the constriction resistance in one electrode, the resistance of the complete contact can be expressed as

$$R_c = \rho/2a \tag{2.4}$$

assuming that both electrodes have the same resistivity. From (2.2) it can be seen that the constriction resistance is concentrated in the electrode-bulk very close to the contact spot: within a radius of r = a lies 50% of R_c.

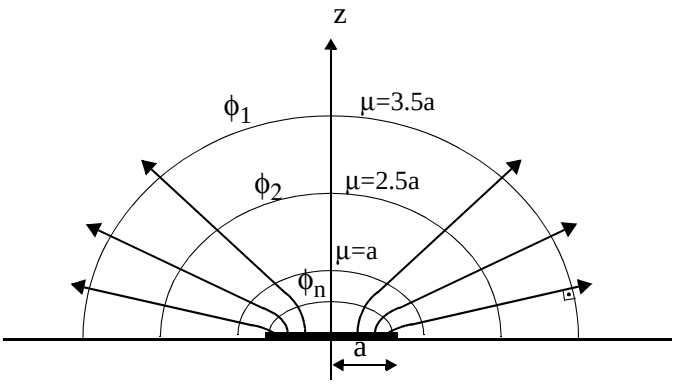

Figure 2.3: Cross sectioned vies of the equipotential surfaces ϕ_n and the current flow lines close to a circular constriction of radius a [2].

When the contact spot is of elliptic shape (2.4) can be adapted by introducing a shape factor f, which is a function of the ellipticity of the contact spot. Defining the contact spot as an ellipse with semi-axes α and β the ellipticity becomes $\gamma^2 = \alpha/\beta$ and the shape factor is expressed as $f = f(\gamma)$. Thus (2.4) is changed to

$$R_c = \rho/2a \cdot f(\gamma) \tag{2.5}$$

where the shape factor $f(\gamma)$ is determined by

$$f(\gamma) = R_c(\alpha,\beta) / R_c(a,a) \tag{2.6}$$

Fig. 2.4 gives an impression of how the constriction resistance of a contact spot is affected by its ellipticity γ, taking the constriction resistance of a circular contact spot with radius a as a reference. There is no analytical solution for the constriction resistance of contact spots with shapes other than elliptic resp. circular but numerical solutions have been published [5]. It appears that the shape of a contact spot has rather little influence on its constriction resistance when comparing it to a circular contact spot of the same area, provided moderate ellipticity with e. g. $\gamma < 10$.

Under laboratory conditions it is possible to make a contact between two electrodes with one single contact spot. In most practical cases, though, the electrodes will be connected by several contact spots, referred to as a multispot contact. If it then can be assumed that these contact spots are sufficiently small and

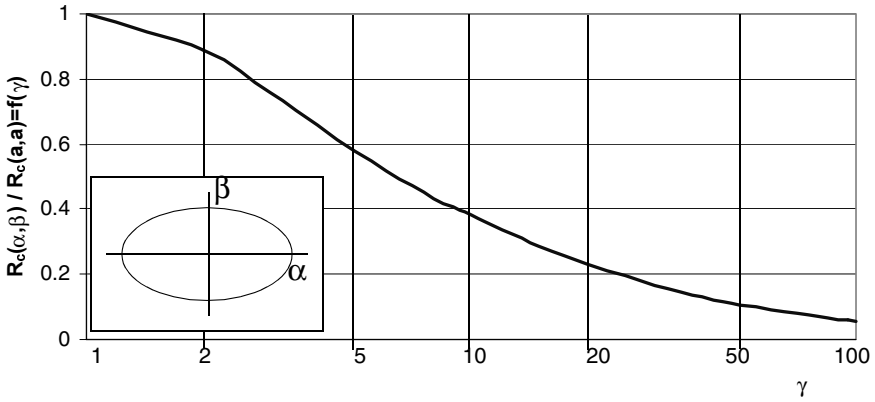

Figure 2.4: Constriction resistance $R_c(\alpha,\beta)$ of elliptic contact spot related to $R_c(a,a)$ of a circular contact spot as a function of γ, with $\alpha\beta = a^2$

not too close to each other, so that any interaction can be excluded, the combined constriction resistance can be calculated as the sum of the constriction resistance of all contact spots connected in parallel

$$R_c^{-1} = \Sigma_n R_n^{-1} \tag{2.7}$$

R_c is the constriction resistance of the contact in total and R_n is the constriction resistance of each of the n contact spots. In Fig. 2.5 a contact with one contact spot is compared to a contact with n contact spots distributed over the electrode surface. For simplicity the contact spots are taken to be circular. The conductive area of the single contact spot is A_I, the conductive area of each of the n contact spots is A_{II}. Using 2.4 to determine the constriction resistance of the contact spots and assuming the conductive area $A_I = n \cdot A_{II}$ it can be shown that [6]

$$R_I = \sqrt{n} \cdot R_{II} \tag{2.8}$$

It is seen that the multispot contact is superior if the total conductive area is the same. Should the above mentioned conditions concerning size and location of the contact spots with the multispot contact not apply and interaction cannot longer be excluded, the approach chosen needs to be adapted. As there exists no analytical solution to this problem the approximation introduced by Holm [7] is presented. When n circular contact spots of radius a are uniformly distributed over an area of radius R on the electrode surface, the contact resistance can be calculated as

$$R_c = \rho(1/2na + 1/2R) \tag{2.9}$$

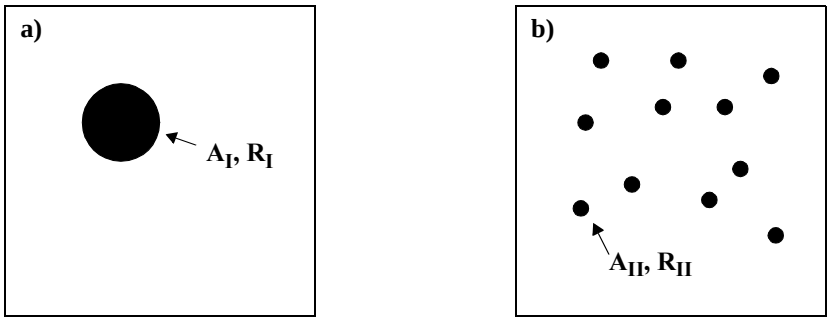

Figure 2.5: Single spot contact (a) compared to multispot contact (b) with conductive area $A_I = n\ A_{II}$, where n is the number of circular contact spots in the multispot surface

Equ. (2.9) corresponds to n single constriction resistances ρ/2a in parallel with an interaction resistance of ρ/2R in series.

In the case the electrodes are made of materials with different resistivity the constriction resistance R_c becomes

$$R_c = (\rho_A + \rho_B)/4a \tag{2.10}$$

where ρ_A and ρ_B are the resistivity of electrodes A and B respectively.

2.1.3 The temperature of a current carrying constriction

When regarding a metallic contact where it can be assumed that neither the electric current nor the heat genereated by the current leave the electrodes until far away from the contact spot, both current and heat flow within the electrodes along the same paths. Moreover, assume that the electrode material is homogenous and both electrodes are of the same material. Then Kohlrausch's well known potential-temperature-relation, from which the elevated temperature in the contact spot can be determined, is valid. Basically, the analogy between current and heat flux can be demonstrated by comparing the following equations:

$$J = 1/\rho(T)\ \text{grad}\ \phi \tag{2.11}$$

and

$$Q = \lambda(T)\ \mathrm{grad}\ T \tag{2.12}$$

J is the current density, Q is the heat flux expressed with the resistivity ρ, the thermal conductivity λ, the potential ϕ and the temperature T respectively. The material properties ρ and λ are only depending on the temperature T. Fig. 2.6 illustrates qualitativly the current flow lines leaving the constriction and then intersecting with the equipotential-surfaces perpendicularly - respectively the lines of heat-flux intersecting with the isothermal surfaces (compare with Fig. 2.3).

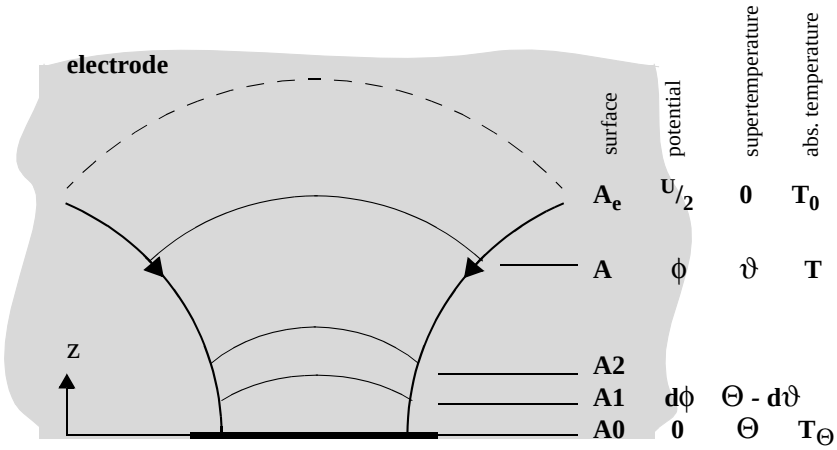

Figure 2.6: Single contact spot of size A_0 with equipotential-isothermal surfaces A at potential ϕ and supertemperature ϑ respectively absolute temperature T within the electrode [2]

The niveau surface A is at temperature T and at potential ϕ. The consecutive niveau surface then is at temperature T+dT and potential ϕ+dϕ. At A_e distant from A_0 the temperature is T_0, the bulk-temperature of the electrode. The potential at A_e is set to U/2. The temperature difference $\vartheta = T - T_0$ is called the supertemperature. The maximum supertemperature Θ is at A_0. Across A_0 there is no heat flow. The heat generated between A_0 and A is $p = I \cdot \phi$. Thus all heat generated between A_0 and A passes through A along the temperature gradient. Equs. (2.11) and (2.12) can be developed into [8, p96]:

$$\phi d\phi = -\lambda(T)\ \rho(T)\ dT \tag{2.13}$$

where integrating (2.13) along the flow lines yields the Kohlrausch equation

$$\frac{\phi^2}{2} = \int_{T}^{T_\Theta} \lambda(T)\rho(T)dT \tag{2.14}$$

which relates the potential drop and temperature on an isothermal niveau surface to the temperature in the contact spot. With the parameters given above and taking the voltage across both electrodes to be U_C (2.14) becomes

$$\frac{U_C^2}{8} = \int_{T_0}^{T_\Theta} \lambda(T)\rho(T)dT \tag{2.15}$$

It has to be pointed out that (2.13), (2.14) and (2.15) are valid under the condition that no heat is accumulated anywhere in the bulk and it is assumed that the process has reached its steady state.

The product of thermal conductivity λ and electrical resistivity ρ as a function of temperature can be expressed by the Wiedemann-Franz-law:

$$\lambda(T)\,\rho(T) = L\,T \tag{2.16}$$

where L is the Lorentz-constant equal to

$$L = 2.45\ 10^{-8}\ V^2 / K^2 \tag{2.17}$$

which is a good approximation for most metals.

Applying the Wiedemann-Franz-law to (2.15) simplifies the solution of the integral to

$$L(T_\Theta^2 - T_0^2) = \frac{U_C^2}{4} \tag{2.18}$$

From (2.18) it is possible to determine the melting voltage across a contact when the maximum temperature T_Θ is set to be the melting temperature of the electrode material.

Greenwood and Williamson [9] developed expression (2.19) giving the temperature distribution within the electrodes across the contact along the z-axis (see Fig. 2.7). The parameter α is the temperature coefficient of the resistivity ρ

as in (2.20). The thermal conductivity λ is assumed to be constant.

$$\operatorname{acos}\frac{1+\alpha\vartheta}{1+\Theta} = \frac{2}{\pi}\operatorname{atan}\left(\frac{z}{a}\right)\operatorname{acos}\frac{1}{1+\alpha\Theta} \tag{2.19}$$

$$\rho = \rho_{20}(1+\alpha\Delta T) \tag{2.20}$$

with ρ_{20} being the electrical resistivity at room temperature (20^oC) and ΔT the temperature difference to room temperature.

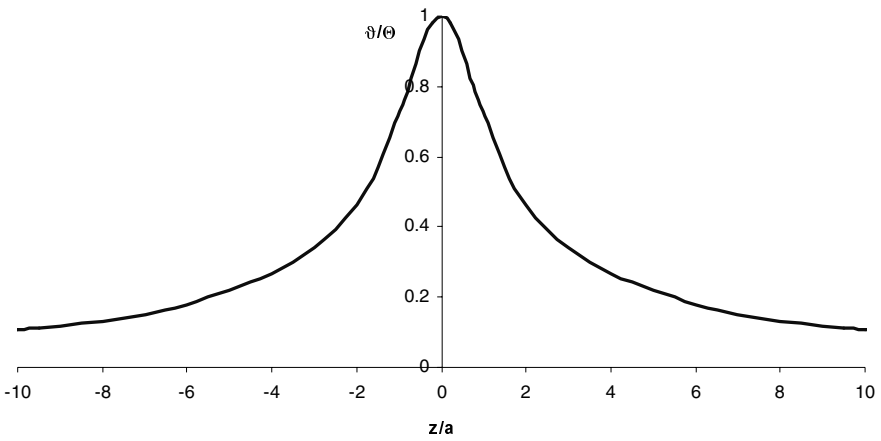

Figure 2.7: Equilibrium distribution of the temperature within the electrodes, with $\alpha = 4.6 \cdot 10^{-3}\ ^oC^{-1}$, $T_\Theta = 600^oC$

From Fig. 2.7 it can be seen, that the temperature decreases almost to that of the bulk over a distance of only a few contact spot radii a. It can be shown that half of the heat is generated within a sphere of radius a from the center of the circular contact spot [10]. This will be referred to as the heat affected zone (HAZ) [11]. The maximum temperature T_Θ occurring in the contact spot plane at $\mu = 0$ (cf. (2.19)) is not longer true when the contact is asymmetric, e. g. $\rho_A > \rho_B$. Then the maximum temperature is located at a distance Δz from the contact spot plane into the electrode with the higher resistivity ρ_A. Δz can be determined as [4, p80]

$$\frac{\Delta z}{a} = \left(\frac{\pi}{2\sqrt{2}}\right)\left(\frac{\rho_{B,\Theta} + \rho_{A,\Theta}}{2\rho_{A,\Theta}}\right)\frac{\Delta U_c}{U_c} \tag{2.21}$$

with ρ_Θ being the resistivity at T_Θ and ΔU_c is the potential drop occurring between $z = 0$ and $z = \Delta z$. It can be shown that the maximum temperature can be assumed to be in the contact spot plane in practical contact applications if ρ_A is of the same order of magnitude as ρ_B.

2.1.4 The influence of temperature on the constriction resistance

The heating of the constriction in the contact spot between two electrodes due to the current causes its temperature to rise. This leads to an increase of the constriction resistance according to the resistivity changing with temperature as shown in (2.20). Assuming a symmetric contact the constriction resistance $R_{c\Theta}$ as it occurs when the contact spot area is at elevated temperature T_Θ can be related to the constriction resistance R_{c0} as shown above in (2.22) as follows:

$$\frac{R_{c0}(\rho_0\lambda_0)}{R_{c\Theta}(\rho\lambda)} = \frac{2}{U_c}\sqrt{\frac{\rho_0\lambda_0}{\alpha}}\,\mathrm{atan}\left(\frac{U_c}{2}\sqrt{\frac{\alpha}{\rho_0\lambda_0}}\right) \tag{2.22}$$

The resistivity ρ_0 in (2.22) is to be set according to the temperature T_0 distant from the contact spot (see Fig. 2.6). The thermal conductivity λ is assumed to be constant ($\lambda = \lambda_0$). Fig. 2.8 illustrates the relation described above for a symmetric aluminium contact with the electrodes kept at room temperature distant from the contact spot. It can be seen that, as expected, $R_{c\Theta}$ increases non linearly with the voltage across the contact U_c, which is related to the temperature in the constriction by (2.15).

2.1.5 Resistance-voltage-characteristic of a constriction

When regarding an experimentally determined R_c-U_c-characteristic for a clean metallic contact (Fig. 2.9) the effects of rising temperature in the constriction with contact voltage U_c and temperature dependency of the constriction resistance R_c can be clarified. Increasing the current and thus increasing the voltage U_c across

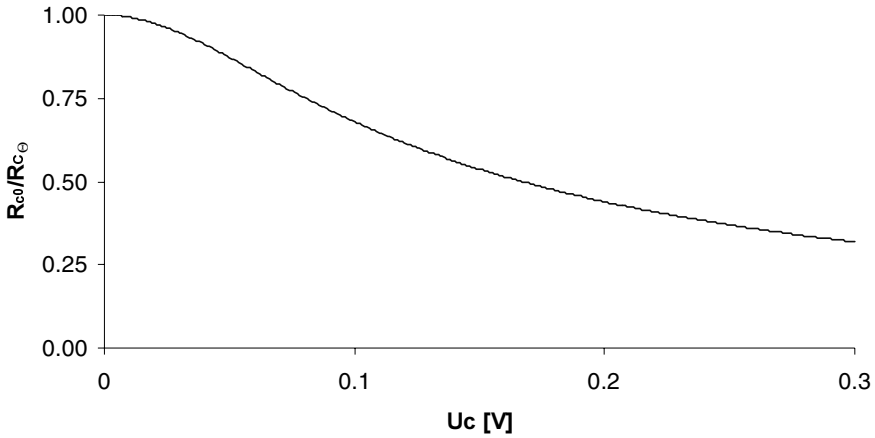

Figure 2.8: Voltage (respectively temperature) dependency of the $R_{c0}/R_{c\Theta}$ ratio in (2.22) with aluminium: $\alpha = 4.6 \cdot 10^{-3}\ ^{o}C^{-1}$, $\rho_{20} = 26.5 \cdot 10^{-9}\ \Omega m$, $\lambda = 222\ Wm^{-1}K^{-1}$

the contact results in a temperature rise of the constriction until the softening temperature of the electrode material is reached (A - B). This is characterised by the softening voltage U_s. Before U_s is reached the R_c-U_c-characteristic is reversible along B-A. As soon as the softening temperature is reached the conducting metal-to-metal area A_c grows with decreasing hardness of the electrode in the vicinity of the contact spot as the electrodes sink together. This again causes a reduction of the constriction resistance R_c (B - C). A further increase of the voltage to the melting voltage U_m is equivalent to the metal close to the contact spot being heated up to its melting point (D). This point on the R_c-U_c-characteristic can only be reached when increasing the current through the contact fast enough so that the electrodes do not sink further together and A_c remains constant. The voltage across the contact cannot be increased above the melting voltage U_m. Any attempt to do so results in immediate melting and subsequent sinking together of the electrodes. This will prompt A_c to grow and R_c to irreversibly decrease according D-E. A lower R_c is with a given current equivalent to a lower U_c and lower temperature in the contact spot. The contact solidifies and the new R_c-U_c-characteristic of the contact is now along E-F. Provided A_c remains constant the new R_c-U_c-characteristic is reversible for voltages below U_s.

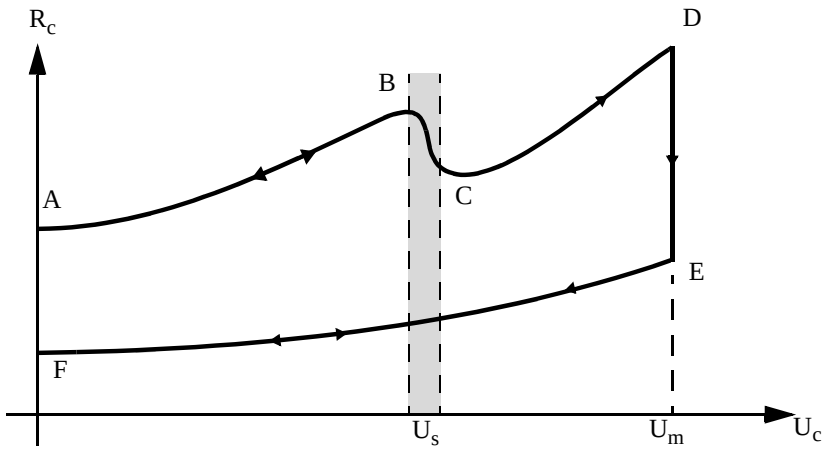

Figure 2.9: Schematic of R_c-U_c-characteristic for a contact. Reversible parts are indicated by double-arrows, U_s is the softening voltage , U_m is the melting voltage

2.1.6 The effect of material properties on electrical conductivity [12, p147]

The electrical conductivity σ of a metal is affected by atom-oscillations (temperature), by impurities, by alloying and by cold-working. All of the above result in a reduced conductivity, summed up in Matthiesen's rule as:

$$\rho = \rho_T + \rho_i \tag{2.23}$$

where ρ is the resistivity of a metal consisting of a part ρ_T depending on temperature and a temperature independent part ρ_i due to impurities, alloying and cold working. More detailed information is given in the following.

2.1.6.1 Influence of atom-oscillations

The decrease in conductivity with increasing temperature has already been stated in (2.20). This is in fact due to the Joule-heat causing the atoms in the crystal-lattice of the metal to oscillate with greater amplitude. An electron driven by an external electric field drifting through the metal is scattered more often then, i.e. the time between two scattering-processes τ_{sc} is reduced. This in turn reduces the mobility μ of the conducting electrons as

$$\mu = e\tau_{sc} / m_e \tag{2.24}$$

where e is the electron charge and m_e is the mass of an electron. From this it can be seen that the conductivity σ is decreased proportionally:

$$\sigma = en\mu \tag{2.25}$$

with n being the number of conducting electrons per unit volume.

2.1.6.2 Influence of impurities and alloying elements

Most metals contain impurities that stem from the production process. In commercially pure metals the amount of impurities is usually below 0.5%. The effect of impurities on electrical conductivity depends on their solubility in the solidified base-metal. The electrical conductivity decreases if the impurities form precipitates and have an atomic number that is very different from the atomic number of the base metal. This is caused by the distortion in the crystal lattice taking the wave-nature of the electrons into consideration. Non-conductive impurities such as oxides and the presence of vacancies or pores further reduce the conductivity by changing the geometry of the conductive path and might give rise to constrictions.

While metal alloys made from components that are not soluble in the solid state exhibit a linear conductivity-concentration relation (Fig. 2.10a), alloys where the components are completely soluble show a strongly non-linear conductivity-concentration relation. Conductivity often sharply decreases even with small deviations from absolute purity of the base metal (Fig. 2.10b).

It turns out that for an alloy with a low percentage of solute

$$\alpha_{base}/\sigma_{base} = \alpha_{alloy}/\sigma_{alloy} \tag{2.26}$$

with α as the temperature coefficient of resistivity as in (2.20).

2.1.6.3 The influence of cold working

When cold-working a metal this may cause an increase in hardness and a decrease in conductivity of up to 5%. This is explained by the additional dislocations as well as vacancies generated during cold-working. A conduction electron crossing a dislocation respectively vacancy cannot proceed with unaltered speed in the same direction due to scattering by the crystalline defect. This reduces its mobility and affects the conductivity of the metal as shown above in (2.25).

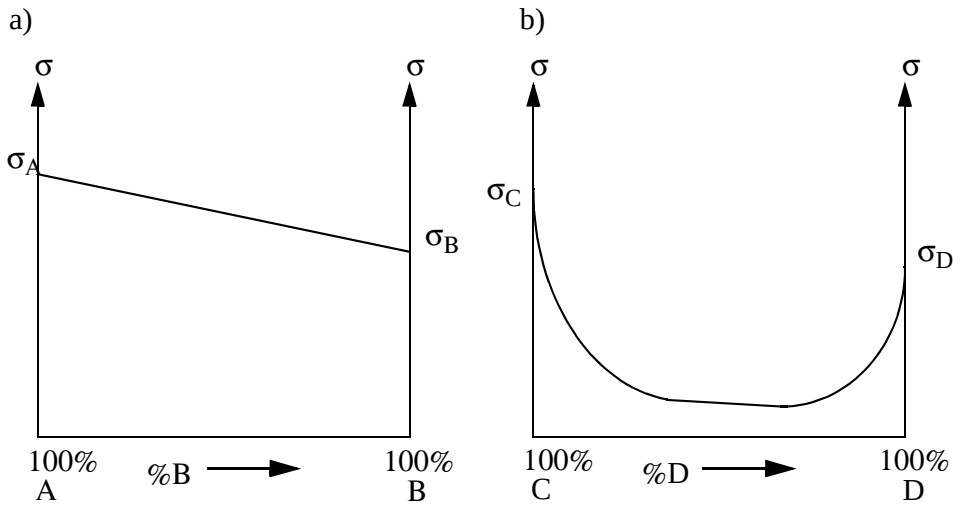

Figure 2.10: Conductivity-concentration relation
a) linear with non-soluble components
b) non-linear with completely soluble components

2.1.7 Deterioration of contact spots

Contact spot failure is rarely initiated by a single effect but rather expected to be the complex result of several deterioration mechanisms acting simultaneously. A review of various deterioration mechanisms in stationary electrical contacts in particular between aluminium conductors will be given in the following.

The dominating deterioration mechanism in many contacts is the oxidation of the contact surface [13], [14]. After having established a metal-to-metal contact by breaking the insulating oxide-layer the conducting contact spot area gradually re-oxidizes. Oxygen, respectively other gases in general, react with the metal at the periphery of the contact spot creating an insulating oxide-ring. The insulating oxide-layer slowly spreads inward until the conducting contact area gradually disappears, resulting in higher resistance. This process is accelerated by the elevated temperature of the contact spot.

Oscillatory micromotion, usually referred to as fretting corrosion, between the electrodes is another important degradation mechanism with stationary electrical contacts [15], [16]. Due to thermal expansion and contraction of the electrodes with varying temperature or due to external forces relative movement of the electrodes in the micrometer-range occurs. This causes the rupturing of the initially formed contact spots. In addition to this, a layer of oxide and metallic

particles is formed between the rubbing electrode surfaces. This reduces the size of the conducting paths and thus decreases conductivity which in turn results in increasing temperature followed by further thermal expansion, eventually leading to the destruction of the contact.

Electromigration has been shown to be a deterioration mechanism when DC is applied to the contact [17] - [19]. In this case the electric current itself causes the deterioration of the contact spots. The high current density and temperature in the constriction initiate a mass transport by electromigration from the cathode to the anode. Vacancies, which eventually cluster to voids and cavities, are left behind in the cathode. This is responsible for a decrease in electrical conductivity of the contact. Ultimately, the cathode becomes so heavily degraded in the contact spot zone that it cannot pass the high current density anymore. This initiates the generation of new current paths in the vicinity of the original contact spot. When no more current paths can be generated the contact eventually fails.

2.2 Theory of thermal fatigue of aluminium

2.2.1 Introduction

In the following sections the effect of thermal fatigue mechanisms as it is assumed to contribute to the deterioration of contact spots is explained. Thermal fatigue is the gradual deterioration and cracking of a material by alternate heating and cooling during which free thermal expansion is partially or completely constrained [20]. A substantial amount of research has been conducted on thermal stresses on make-and-break-contacts with short-circuit currents in order to investigate into contact welding phenomena or concerning contact erosion-phenomena due to arcing. Identifying the thermal stresses caused by temperature cycling within the constriction of a stationary contact as detrimental to the contact appears to be a new approach, which could not be found being described earlier.

2.2.2 The temperature of the constriction as a function of time

The first step to be taken when assessing the effects of thermal stresses in the constriction is to find the transient temperature response to the alternating current passed through the contact. There exists no complete analytical solution for this problem; for a review regarding the solution of the general problem refer to [21].

Holm presents an approximated solution based on a simplified model in [22, p49]. The current flow lines in the constriction are spherically symmetric and the electrical resistivity ρ as well as the thermal conductivity λ are assumed to be constant (see Fig. 2.11). The contact spot is represented by the surface of a sphere of radius b. The size of the sphere is related to the area of the contact spot as $b = 0.636a$. From this model a differential equation describing the time dependent temperature distribution in a half-space with spherical heat-source can be derived:

$$\frac{\partial^2 \vartheta}{\partial r^2} + \frac{2}{r} \cdot \frac{\partial \vartheta}{\partial r} + \frac{\delta}{r^4} = \frac{c}{\lambda_0} \cdot \frac{\partial \vartheta}{\partial t} \tag{2.27}$$

Here ϑ is the supertemperature (as shown in Fig. 2.6), r is the radius, λ_0 is the thermal conductivity at ambient temperature and c is the specific heat of the metal per unit volume.

The heat generated by the current passing through the constriction is represented in the parameter δ as

$$\delta = \frac{\rho_0 I^2}{4\pi^2 \lambda_0} \tag{2.28}$$

with ρ_0 being the resistivity of the metal at ambient temperature and I the current. The step response of the temperature in the contact spot Θ for $I = 0$ at $t < 0$ and $I = I_0$ at $t \geq 0$ according to (2.27) is given as

$$\Theta(t) = \Theta(\infty)\,[1 - \Psi(z)] \tag{2.29}$$

with

$$\Psi(z) = \frac{2}{\sqrt{\pi}} \int_0^{\infty} \left[f(2\beta\sqrt{z}) - e^{-2\beta\sqrt{z}} \int_0^{2\beta\sqrt{z}} f(\xi) e^{\xi} d\xi \right] e^{-\beta^2} d\beta \tag{2.30}$$

where

$$f(x) = 2 - \frac{1}{1 + x} \tag{2.31}$$

and the dimensionless time

$$z = \frac{\lambda_0}{c b^2} \cdot t \tag{2.32}$$

and the steady state temperature in the contact spot

$$\Theta(\infty) = \frac{\delta}{2b^2} \tag{2.33}$$

where (2.33) also may be derived from the Kohlrausch-equation (2.14). In Fig. 2.12a graphical representation of (2.29) is shown. By scaling the time-axis according to (2.32) an approximation of the temperature $\vartheta(t,r)$ in the contact spot and into the electrode-bulk can be obtained. The result is shown in Fig. 2.13 for an aluminium contact at ambient temperature [22, 17]. It can be seen from the plot that the thermal time constant τ of the contact spot is in the order of a few hundred

microseconds ($\Theta(3\tau) = 0.95\ \Theta_{max}$). The plot for the isothermal sphere-surface at r=4b represents the temperature development further into the electrode.

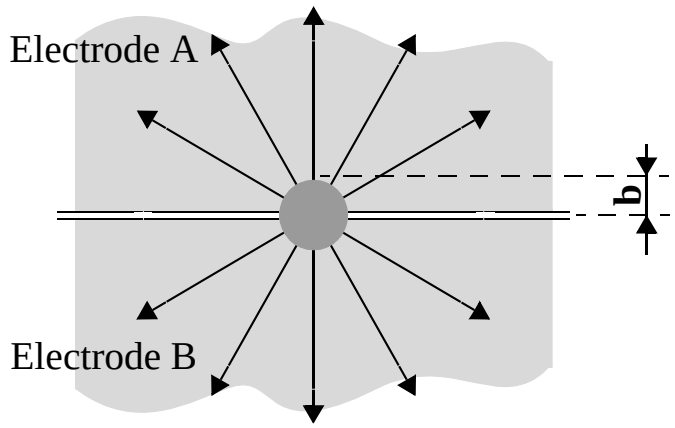

Figure 2.11: Simplified model of a constriction with radial current flow lines. The contact spot is approximated by a sphere of radius b [2]

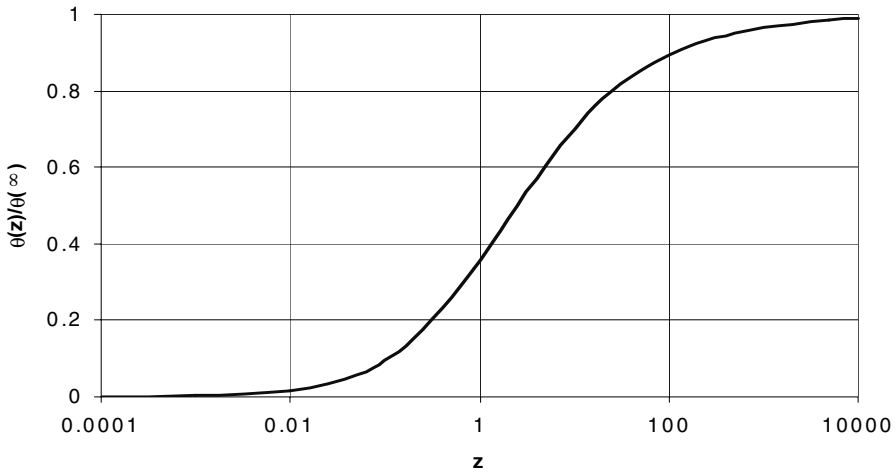

Figure 2.12: Temperature response of the constriction with current step $I = I_0$, $t \geq 0$ applied against dimensionless time z [2]

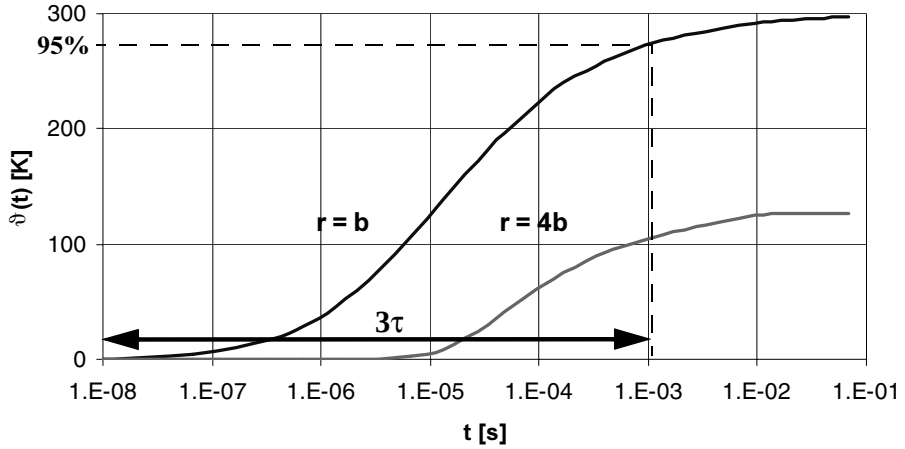

Figure 2.13: Temperature response of a contact between aluminium conductors [2] with a = 25μm, U = 150mV, c = 2.4·10^{6}JK^{-1}m^{-3} in the contact spot (r=b) and some distance from the contact spot (r = 4b), thermal time constant τ ≈ 300 μs

The small thermal time constant τ obtained from this approximate solution of the step response of the temperature allows the conclusion that the temperature in the contact spot ϑ(t,r = 0) follows any variation of the power dissipated in the constriction almost undelayed.

When passing sine wave AC through the contact the voltage across the contact U_c can be expressed as [23]

$$U_c(t) = 2\sqrt{\frac{\rho_0\lambda_0}{\alpha}}\tan\left(\sqrt{\frac{\alpha\rho_0}{\lambda_0}}\cdot\frac{i(t)}{2a}\right) \tag{2.34}$$

with

$$i(t) = I_0\cos(\omega t) \tag{2.35}$$

where ρ_0 and λ_0 are resistivity and thermal conductivity at a location distant from the contact spot at bulk temperature.

Assuming the resistivity ρ to be temperature dependent according to (2.20) and the thermal conductivity to be constant $\lambda = \lambda_0$ it can be shown for a geometry as presented in Fig. 2.6 that [9]

$$U_c^{\,2} = 8\rho_0\lambda_0\left[\Theta + \frac{1}{2}\alpha\Theta^2\right] \tag{2.36}$$

Solving (2.36) with respect to Θ, substituting U_c with (2.34) and using this new expression for Θ in (2.19), an expression giving the supertemperature as a function of the applied current i(t), the dimensionless position (z/a) along the direction of the z-axis and material parameters is obtained:

$$\vartheta(t, z) = \frac{\cos\left[\frac{2}{\pi}\operatorname{atan}\left(\frac{z}{a}\right) \cdot B(i(t))\right]}{\alpha \cdot B(i(t))} - \frac{1}{\alpha} \tag{2.37}$$

with

$$B(i(t)) = \sqrt{\frac{\alpha\rho_0}{\lambda_0}} \cdot \frac{I_0}{4a}\cos\omega t \tag{2.38}$$

Equ. (2.38) has no physical interpretation, it is introduced only to make (2.37) legible.

The absolute temperature T(t,z) in the contact spot and along the z-axis is obtained by adding the bulk-temperature T_0 of the electrodes to (2.37)

$$T(t,z) = \vartheta(t,z) + T_0 \tag{2.39}$$

This is shown in Fig. 2.14 for an aluminium contact where 125 A with 50 Hz are applied for different distances z into the electrode. The bulk temperature is set to 80 ^{o}C, the contact spot radius is 20 µm. It can be seen that the temperature in the contact spot oscillates with the double frequency as the current i(t). Further away from the contact spot into the electrode bulk the oscillations decrease in amplitude. This can be compared to Fig. 2.7. The phase-shift as it would appear between the curves shown in Fig. 2.14 due to the increasing thermal capacity along the z-axis into the electrode is neglected. The validity of this approach could be verified using a modified electro-thermal model as suggested by Veijola [24] for numerical solution. A qualitative representation of T(t,z) with phase-shift is shown in Appendix I.

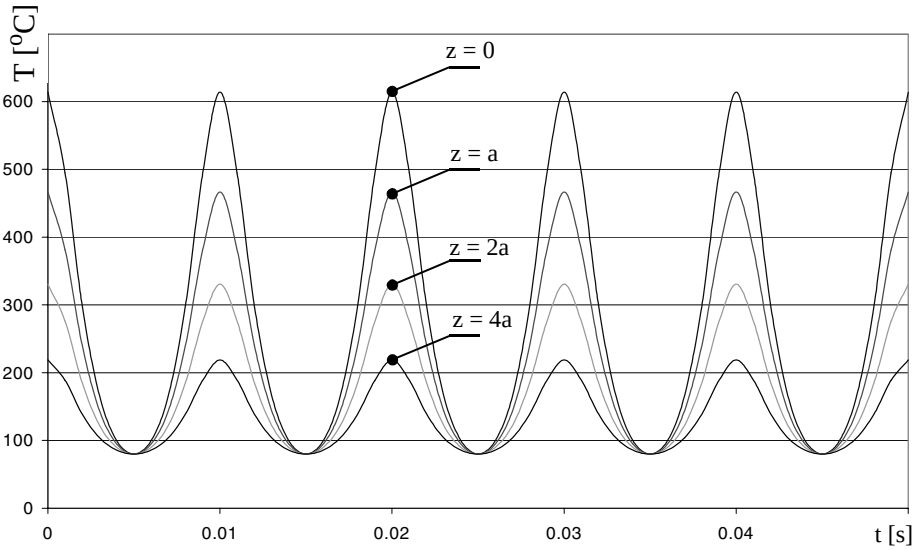

Figure 2.14: Temperature cycling with applied AC at various distances z from the contact spot into the electrode

2.2.3 Thermal fatigue due to temperature cycling

The thermal cycling of the heat affected zone close to the contact spot as described above imposes considerable stress on the metal which eventually leads to cracking. The mechanisms behind this will be described in the following.

Fig. 2.15 shows a cross section of a contact spot and the heat affected zone around it. If the heat affected zone was not constrained in the metal it would expand with rising temperature according to

$$V = V_0 [1+\gamma_v(T-T_0)] \tag{2.40}$$

with V being the volume of the heat affected zone at temperature T, V_0 being the volume of the heat affected zone at temperature T_0 and γ_v the coefficient of thermal expansion. But as the heat affected zone is constrained in the metal it cannot expand as described in (2.40). Instead the pressure from the thermal expansion generates considerable stress on the material surrounding the heat affected zone. A simplified model shown in Fig 2.16 is derived reducing the three-dimensional problem of a constrained volume in bulk metal to one dimension which is sufficient to describe the principles behind thermal fatigue cracking. A mathematical representation of the three-dimensional stresses can be found in [25].

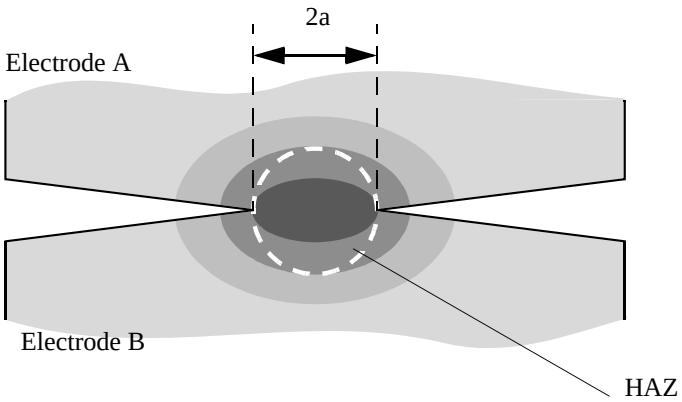

Figure 2.15: Schematic cross section of contact spot with heat affected zone, (dashed circle) of diameter 2a. Different shades of grey indicate different temperatures.

The heat affected zone in Fig. 2.16 would expand along the x-axis with rising temperature if it was unconstrained. Expansion in the z-direction is neglected. The linear thermal expansion is determined as:

$$l = l_0 [1+\gamma_l (T-T_0)] \tag{2.41}$$

where l is the length at elevated temperature T, l_0 is the length of the heat affected zone at temperature T_0 and γ_l is the linear thermal expansion coefficient. Because

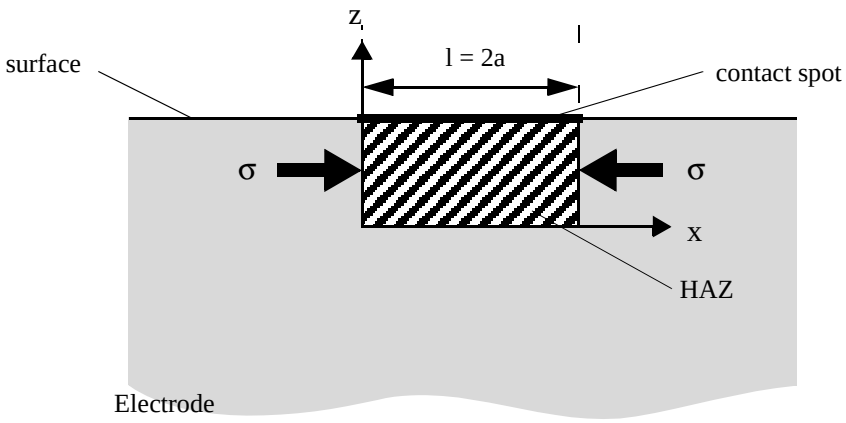

Figure 2.16: The heat affected zone HAZ being subjected to compressive stress due to thermal expansion

thermal expansion of the heat affected zone is not possible, the constraining bulk-metal around the heat affected zone generates a compressive stress σ with rising temperature as shown in Fig. 2.16 [26]

$$\sigma = E\ \gamma_l\ (T\text{-}T_0) \tag{2.42}$$

Where σ is the compressive stress and E is the Young's-modulus. The thermal expansion of the surrounding metal-bulk and any temperature variations across the HAZ are neglected. This is a reasonable assumption due to the temperature dependency of γ_l such that $\gamma_{l\ HAZ} > \gamma_{l\ Bulk}$ and as well bearing in mind the temperature gradient as shown in Fig. 2.7.

Taking the temperature cycling postulated in Section 2.2.2 and shown in Fig. 2.14 in the heat affected zone into account, the compressive stress becomes

$$\sigma(t) = E\ \gamma_l\ \vartheta(t,r = 0) \tag{2.43}$$

which is true in the elastic region of the stress-strain-diagram.

In Fig. 2.17 an engineering stress-strain diagram is shown with the characteristic material properties yield point σ_y, ultimate strength σ_m and rupture strength σ_r. When applying a stress below the yield strength the deformation of the material is purely elastic, above the yield strength the deformation has a plastic component. The yield strength in tension is here assumed to be equal to the yield strength in compression.

Stress-strain behaviour under cyclic strain is characterized by a stress-strain-hysteresis loop [27] as shown in Fig. 2.18. Strain hardening and the Bauschinger-effect are here neglected. Strain hardening increases the ultimate strength σ_m, whereas the Bauschinger-effect lowers the yield strength σ_y. In the following further simplifying assumptions for the idealised model are made:

- The Young's-modulus E and the linear expansion coefficient γ_l are constant.
- The stress σ is independent of strain rate $\dot{\varepsilon}$.
- The electrode material is isotropic.
- Creep-strain is neglected.
- Cyclic stress-strain-response is assumed to be identical to monotonic stress-strain-response.

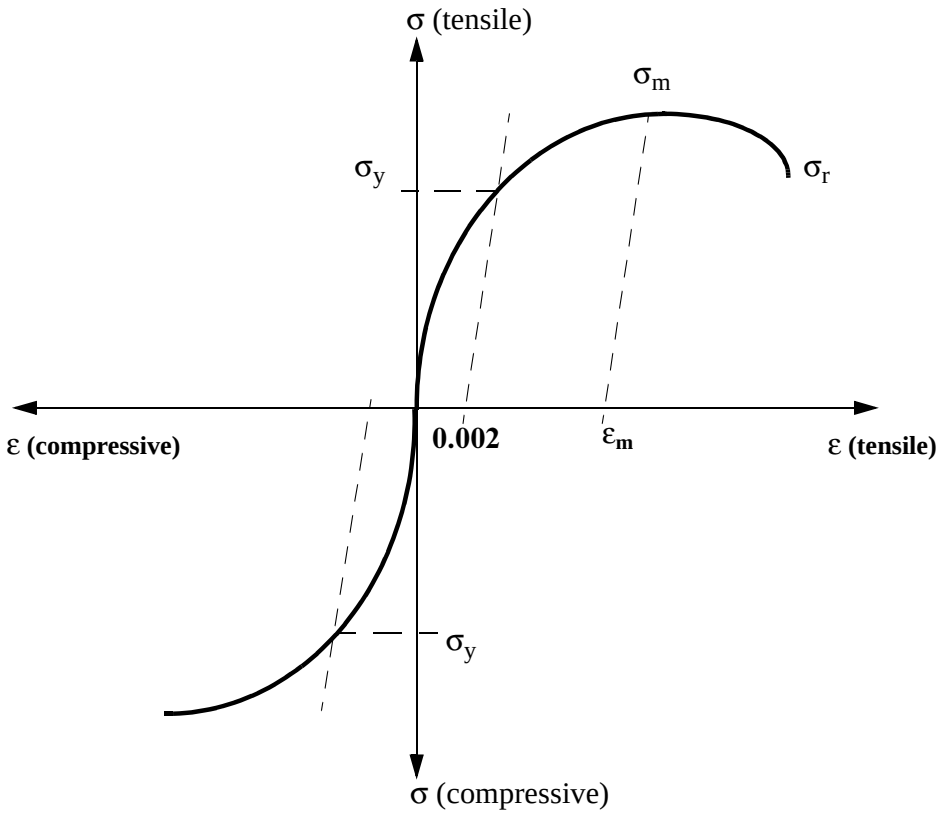

Figure 2.17: Engineering stress-strain-diagram with characteristic material properties yield strength σ_y at $\varepsilon = 0.2\%$, ultimate strength σ_m at ε_m and rupture strength σ_r

In [28] the stress-strain-relationship with thermal cycling for this idealised model of a constrained bar is described. This may be compared to the constrained heat affected zone subjected to thermal cycling. Figure 2.19 summarises the results.

The temperature cycling of the heat affected zone starts at A at ambient temperature. With rising temperature compressive stress is generated along ABC. Plastic flow is initiated at B when the compressive stress exceeds the yield strength. Because of strain hardening the stress continues to increase to C. At C the cooling cycle begins following the stress-strain-curve along CDE. The yield point of the cooling cycle is now at D, which has a lower absolute value than the corresponding yield point at B due to the Bauschinger-effect. When the initial temperature is restored, the state of the heat affected zone is at E. A tensile elastic strain at E is necessary to offset the compressive plastic flow that occurred along

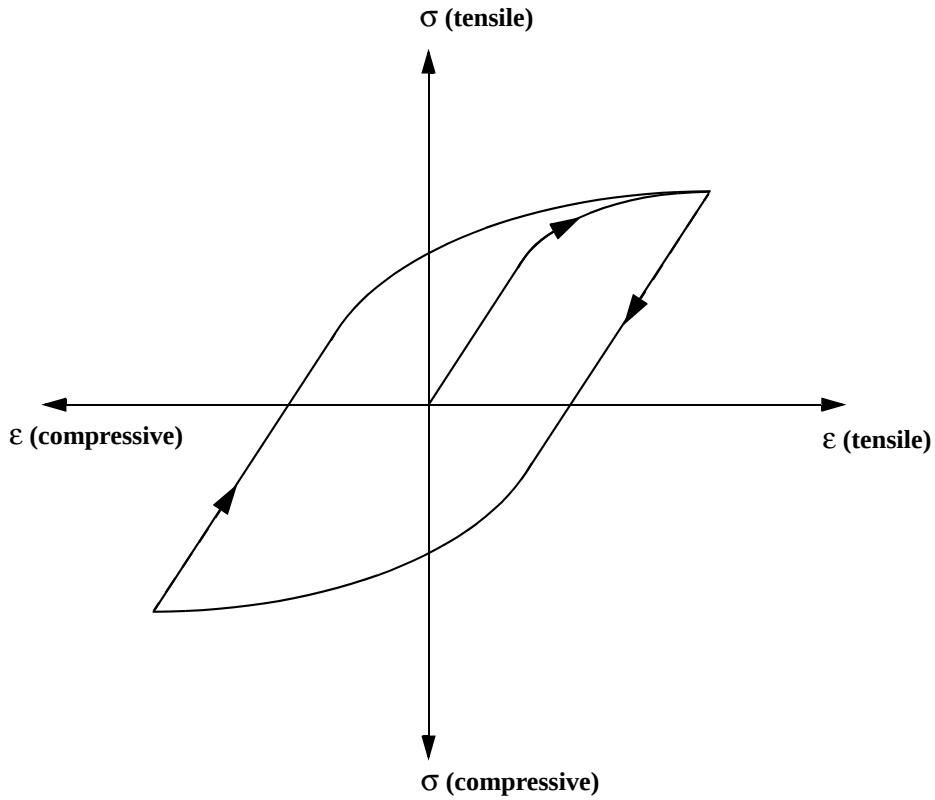

Figure 2.18: Stress-strain-hysteresis loop associated with cyclic strain that produces fatigue damage [27]

BC and thus the net strain of the heat affected zone is returned to zero. This tensile elastic strain introduces the tensile stress EA. When reheating the heat affected zone the stress-strain-curve proceeds along EF, accounting qualitatively for the Bauschinger effect and strain hardening. The stress-strain-response of most materials changes significantly with applied cyclic stresses in the beginning, but typically the hysteresis-loops tend to stabilise as is schematically represented in the GH-loop. The GH-loop shifts towards an compressive strain offset.

The above described one-dimensional stress-strain-relationships occurring with thermal cycling can be related to the stresses appearing with the three-dimensional thermal expansion of the heat affected zone of an electrical contact. The mechanism behind the appearance of the stress-strain-hysteresis-loops is the strain hardening due to the increase in dislocation-density in the metal with thermal expansion. The dislocation density is related to the following expression given in [29]

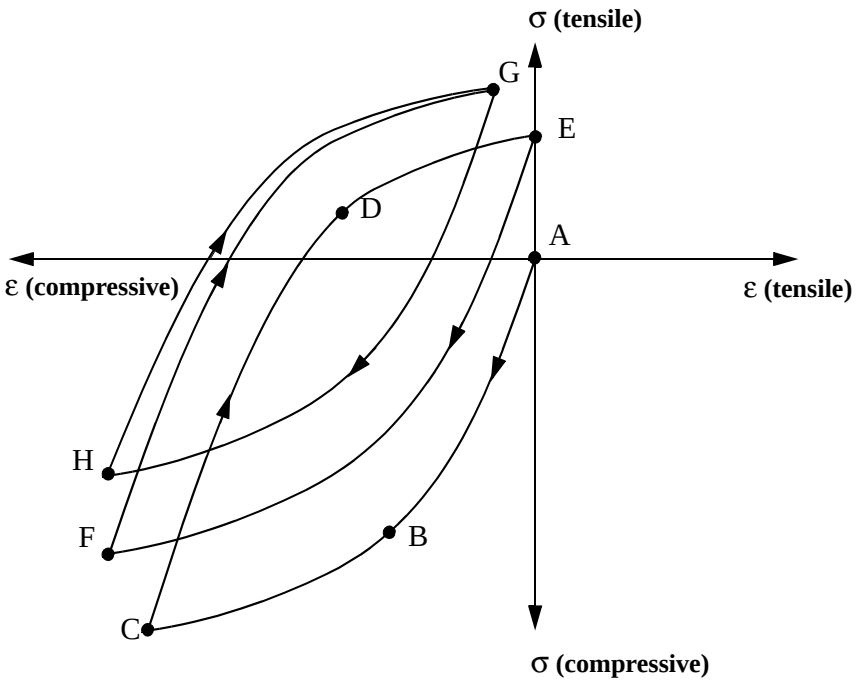

Figure 2.19: Stress-strain-hysteresis-loop [28] of the heat affected zone in an electrical contact when AC is applied, resulting in thermal fatigue and cracking

$$n = \frac{\Delta V}{a^2 b} \tag{2.44}$$

where n is the absolute number of dislocation loops generated per cycle, $\Delta V(T) = V - V_0$ is the change in volume per cycle as in (2.40), a is the contact spot radius and b is the Burgers-vector of the metal. For a contact spot between aluminium electrodes with a = 25 µm, b = 0.286 nm cycling through a temperature difference of ΔT = 300 K (2.44) yields $n = 10^3 \ldots 10^4$ new dislocation loops per cycle thus creating an entangled mess of dislocations within the heat affected zone [30].

The enthalpy of the heat affected zone increases with increasing dislocation density. In order to reduce the enthalpy the heat affected zone undergoes a cyclic recrystallisation-process. Many small grains are generated which subsequently grow until their boundaries meet. The recrystallisation-temperature T_R necessary for this is approximately

$$T_R \approx 0.4\, T_M \tag{2.45}$$

with T_M being the melting temperature in Kelvin. For aluminium T_R is determined to 200 ^oC. According to (2.18) this temperature is attained in the contact spot when a voltage of 125 mV is applied across the electrodes. At higher voltages also the metal distant from the heat affected zone is expected to recrystallise but due to the lack of cyclic thermal stresses the grains grow much larger than those in the heat affected zone. Such a discontinues grain-growth leads to further embrittlement and increases the probability for cracking [12, 31].

Any metal specimen exposed to cyclic stress-strain-loading above the endurance limit σ_g will crack after a certain number of cycles. This is commonly referred to as fatigue failure. How the above described processes of cyclic loading and recrystallisation contribute to this will be outlined in the following.

As shown in the Wöhler-diagram in Fig. 2.20 the ultimate strength σ_m for non-ferrous metals decreases to the endurance limit σ_g after about 10^8 load-cycles [32]. But since the Wöhler-curve for aluminium in particular continues to slope beyond 10^8 load-cycles it can be concluded that aluminium will always experience fatigue failure after a certain number of load cycles, even if the applied stress is below the yield strength in the elastic domain of the stress-strain-response [11]. This is due to the fact that some of the crystals in the specimen have slip

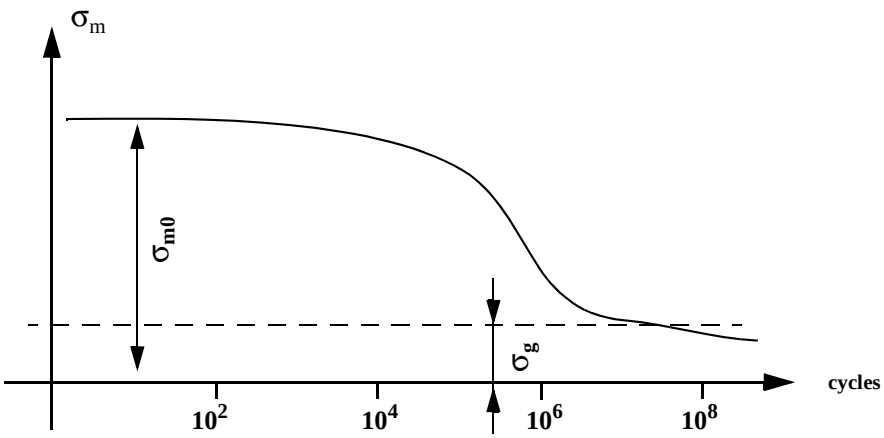

Figure 2.20: Wöhler diagram, the ultimate strength σ_m for non-ferrous metals falls below its endurance limit σ_g after 10^8 cycles [32, 33]. For aluminium at T = 20°C: σ_{m0} = 100 MPa, σ_g = 25 MPa [34]

planes more or less parallel to the direction of maximum shear-stress occurring in the specimen. The probability for the existence of such crystals increases with the number of crystals with different orientation. These crystals experience then plastic deformation while the other crystals are deformed elastically. When the stress is reversed plastic and elastic deformation are as well reversed. Thus each cycle causes plastic extension and compression in some crystals, which in the end results in cracks due to the separation of atomic planes. The orientation of a crack is perpendicular to the direction of the applied stress. The crack initiation in thermal fatigue is most likely to occur in the hottest region of the heat affected zone since the yield point is locally reduced there. In addition fatigue-cracks often originate at surface imperfections [35]. It has to be kept in mind that the contact spot itself is the most outstanding surface imperfection on the otherwise meticulously polished electrode surface.

3

Experimental Setup and Procedure

3.1 Introduction

The experimental method is to a large extent based on a procedure which has been described earlier in [17] and [36]. Setup and procedures were somewhat modified in order to allow for AC-experiments. The general working principle will be outlined in the following.

3.2 Specimen preparation and assembly

The current carrying areas of a contact surface are usually minute. In sum they only cover a small percentage of the apparent contact area. As it is believed that stability and reliability of a contact are strongly related to phenomena occurring within these small areas, a detailed knowledge of the contact spot configuration and behaviour under different operating conditions is of great importance and might thus contribute to better understanding of deterioration mechanisms in stationary contacts.

One important phenomenon is the high temperature which occurs in the contact spots, caused by the high current density in the contact spots. Similar to resistance-spot-welding the electrodes become permanently mechanically connected in the contact spots. However, the contact spot weld often has by far lower mechanical strength compared to an ordinary weld. When opening the contact by separating the electrodes, the contact-spot-welds break, leaving characteristic contact spot fracture areas behind on the electrode surface. Close examination of these contact spot fractures yields considerable information about the deterioration mechanisms.

The electrodes used in the experiments were made from pure aluminium (Al > 99.9%) and commercially pure aluminium (AA1350) as commonly used for electrical conductors, often cold worked. See Appendix II for further information on material properties. For some experiments 10% zinc was alloyed into the electrodes as a tracer material.

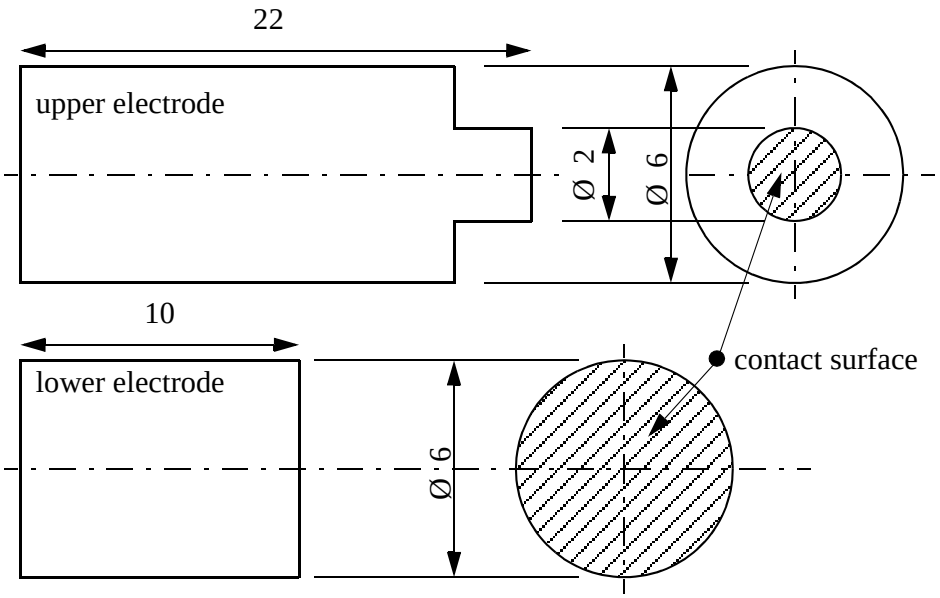

Figure 3.1: Size and geometry of the aluminium electrodes (in mm), the contact surfaces are shown to the right as shaded areas.

Both electrodes were machined out from the bulk material. Their geometry and size are shown in Fig. 3.1.

The electrodes were mounted in cylindrical aluminium holders, as shown in Fig. 3.2a. The purpose of these holders lies in the easier handling of the specimen, in particular when it comes to applying the sensors. The lower electrode was fastened to the holder with a screw. The upper electrode was mounted in the holder by using a special wax (Apiezon W). This wax is solid and reasonably strong at room temperature, but softens gradually from 40 ^{o}C and above, melting starts above 85 ^{o}C. The advantages of this will be explained later on.

While mounted in the holders the contact surfaces of both electrodes were polished with diamond paste down to a surface roughness of 1 µm. After that they were rinsed in alcohol in order to clean the contact surfaces from diamond paste. The holders, each with a fixed contact member, were then put together and secured with epoxy glue, (see Fig. 3.2b). An annular insulating plastic foil of approximately 15 µm thickness prevented the contact surfaces from touching each other during assembly. This ensured that no mechanical damage could be done to the polished contact surfaces.

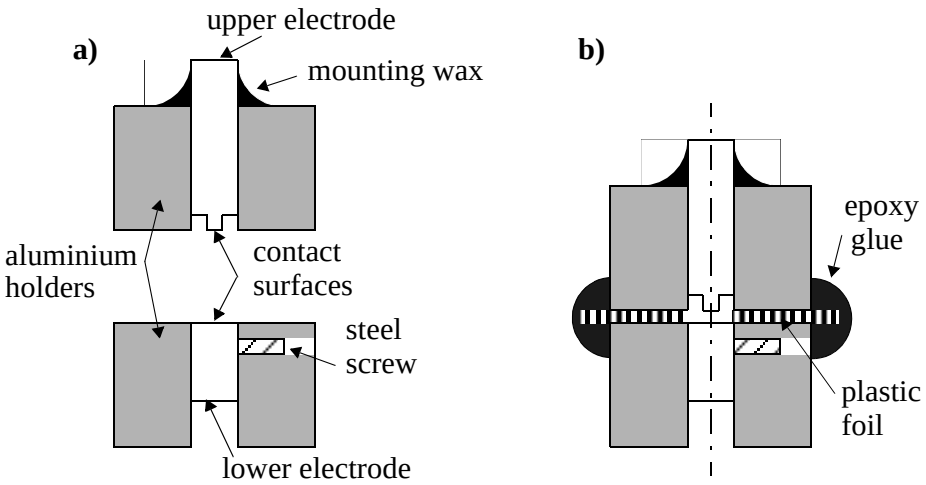

Figure 3.2: Cross section of the aluminium holders with electrodes before a) and after b) assembly

Using electrodes with polished surfaces in the experiments has several advantages compared to contacts made from rougher electrodes. The detection of the location of the contact spots on the electrode surface of the opened contact is made easier when examining the surface optically or by scanning electron microscope, because the contact spot fracture appears by far more distinct on a carefully polished surface. This aspect becomes particularly important when examining cross sectioned contact spot fractures. In addition to that polishing smoothens the surface asperities in a way that - upon carefully mating the electrodes - it is most likely to produce only one single metallic contact spot or none at all, when the protective oxide layer is not mechanically ruptured by protruding asperities.

The specimen was then placed in a rack where the contact force F from a mechanical load could be exerted onto the upper electrode, see Fig. 3.3. The power cables, temperature and voltage sensors were carefully connected to the holders, as shown in Fig. 3.4. The upper electrode was then loosened from the aluminium holder by heating the wax with hot air, making it soft. Mechanical load was applied to the upper electrode by slowly pouring water into the beaker. As the upper electrode sagged about 15 µm - corresponding to the thickness of the plastic foil between the aluminium holders - mechanical contact between the electrode surfaces was established. The load was then gradually increased to 20 N.

Using this procedure ensures careful mating of the electrodes and keeping them firmly together. The effects of lateral movement and mechanical shock on the

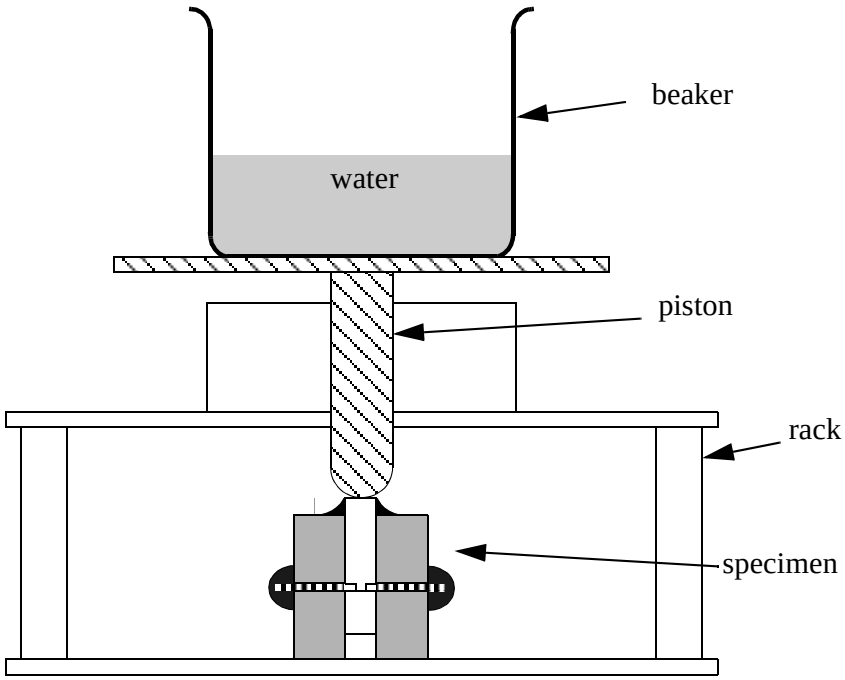

Figure 3.3: The rack for mounting the specimen and exerting contact force on the upper electrode

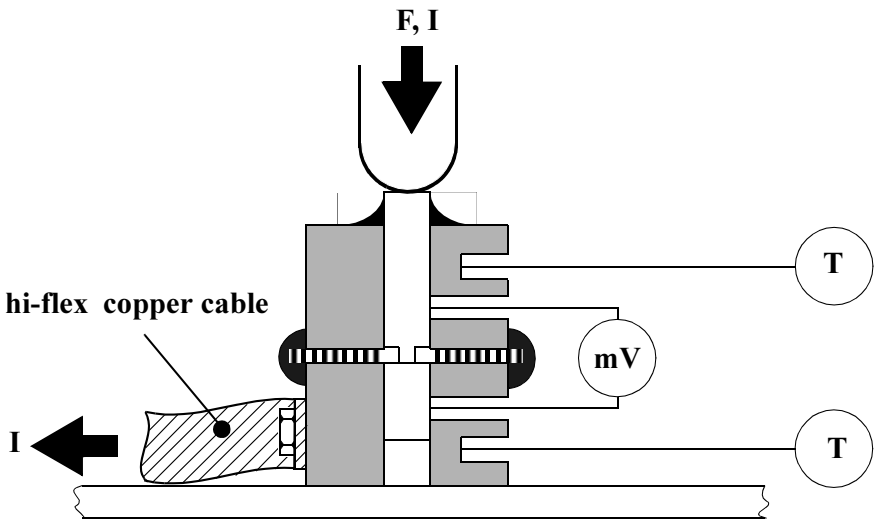

Figure 3.4: Schematic cross section of the specimen with contact force F = 20N applied to the upper electrode and temperature- and voltage-sensors as well as power cable connected.

contact were minimized. The bulk temperature of the specimen was sufficiently high during the experiments to keep the mounting wax soft, such that the upper electrode remained virtually loose. Upon terminating the experiment the specimen cooled and the wax solidified, fixing the upper electrode to the holder again.

3.3 Application of current

The experiments were performed applying 50 Hz sine-wave AC to the contacts. The circuit used is shown in Fig. 3.5. Up to 150 A_{RMS} could be passed through the contact. Due to the insulating plastic foil separating the electrode holders the current was forced to pass through the contact interface. The voltage drop across the contact, the current and the bulk temperature in the aluminium holders were continuously monitored by oscilloscope and recorded by data-logger. If not otherwise indicated all measurements of voltage and current are always given as peak values.

The power supply chosen was a 3 kW transformer with two 230V/10V windings connected in parallel. The transformer could supply up to 150 A_{RMS} to the circuit. The input voltage to the transformer was supplied by a variac and could be varied between 0 and 230 V_{RMS}. The output voltage could then be adjusted between 0 and 10 V_{RMS} accordingly. The series resistor R_s = 68 mΩ stabilized the current

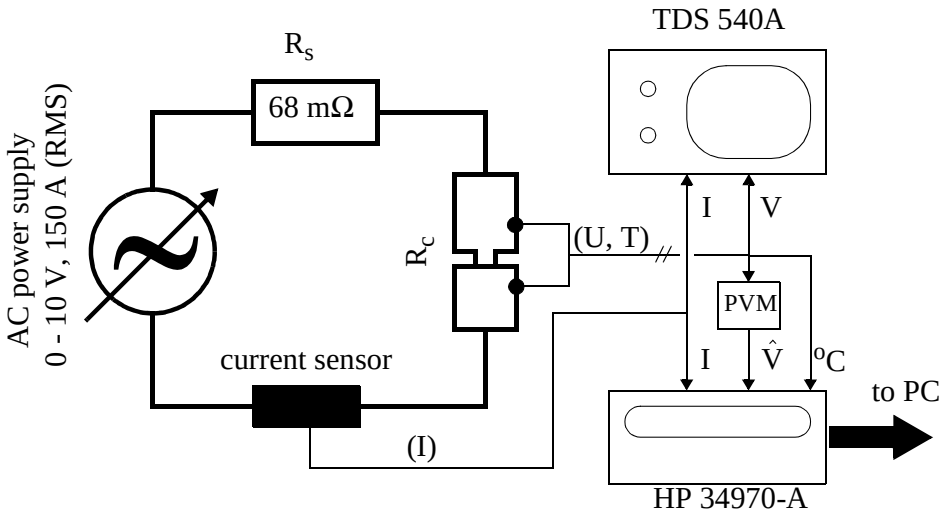

Figure 3.5: Schematic representation of the circuit used for the experiments. R_s minimizes current variations, the current sensor works by magnetic field compensation, the PVM returns the peak voltage $\hat{V}$.

through the contact against variations in the contact resistance R_c, with $R_s >> R_c$. The current was measured by a current sensor using magnetic field compensation (LEM LT-100S). The signal from the current sensor was fed into a 44-channel HP 34970-A data-logger and into a digital 4-channel oscilloscope (Tektronix TDS 540A). The voltage probes were connected to the oscilloscope as well and a peak volt-meter (PVM). The output signal of the PVM was a DC voltage directly proportional to the amplitude of the voltage across the contact. Electromagnetically induced voltages in the measuring circuits were not exceeding a few millivolt in amplitude and are neglected. The temperature probes were copper constantan-thermocouples directly connected to the data-logger. All data logged was immediately stored on a PC. A 1 Msample A/D digitizer (Analogic) connected in parallel to the oscilloscope was used to sample real-time measurings of voltage and current in 16 bit resolution when appropriate.

The experiment was started by slowly rising the voltage applied to the circuit. In those cases where a metallic contact was established when applying the load to the contact, the current started flowing immediately. If no metallic contact was established initially, the voltage across the contact was increased until the oxide film covering the electrodes broke due to fritting. This would typically occur for voltage amplitudes between 0.5 and 1.0 V. The voltage then immediately dropped to values around 150 mV with a current in the order of 10 A. Upon fritting it is most likely that only one single contact spot is produced because the voltage across the contact drops below the breakdown voltage of the oxide film (see Section 3.2) immediately after the fritting. The voltage, current and temperature recorded during the experiment can in this case then be directly related to the phenomena occurring in this particular contact spot.

The voltage was then further increased within a few minutes until the current had reached the desired level. During this process the voltage across the contact U_c was always in the range 150 mV to 300 mV, in order to avoid melting of the contact spot, but allowing the contact spot to gradually grow as the softened surface asperities sink together. The constriction resistance decreases accordingly,as described in Section 2.1.5. The contact resistance was determined from the peak values of voltage and current measured as

$$R_c = \frac{U_c}{I} \tag{3.1}$$

i.e. when the temperature in the contact spot was at its peak value. The duration of the experiments span from a few minutes to several days.

3.4 Examinations by SEM

The instrument used was a Jeol JSM T-330A scanning electron microscope (SEM) equipped with a LINK ANALYTIC 10/25S energy dispersive analyzer (EDA). The scanning signal was sent to a PC running SEMAFORE digitizing software. Accelerating voltages from 5 to 20 kV were used in the analysis. The spatial resolution for secondary-electron and backscattered-electron images with the SEM is typically 0.05 μm.

After completing the experiment the voltage and temperature sensors were disconnected and the specimen was carefully removed from the rack. The glued aluminium holders were broken apart, so that the surfaces of the electrodes mounted in the holders became visible, the annular plastic foil was removed and the contact holders with the electrodes were examined in the SEM.

A typical example of a contact spot fracture as it appears on the polished contact surface is shown in Fig. 3.6. In spite of their size the contact spot fractures are fairly easy to detect as surface irregularities of characteristic appearance.

In addition to the contact surface examinations some of the electrodes were cross-sectioned through the center of the contact spot, perpendicular to the electrode surface. This was done by removing the electrode from the aluminium holder and embedding it in transparent epoxy. The embedded electrode was then ground

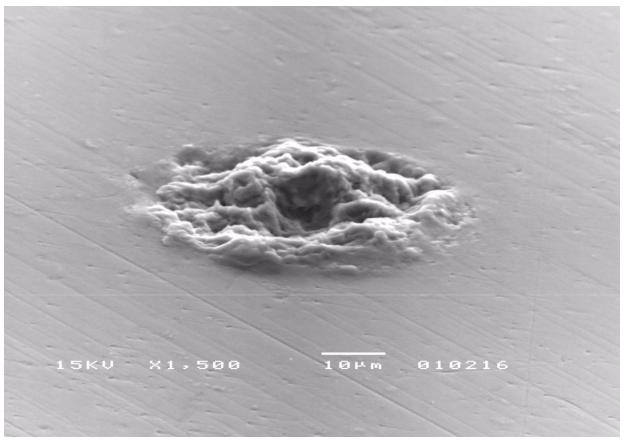

Figure 3.6: SEM secondary electron image of contact spot fracture on polished electrode surface seen from an angle of 30 ^{o} with the surface

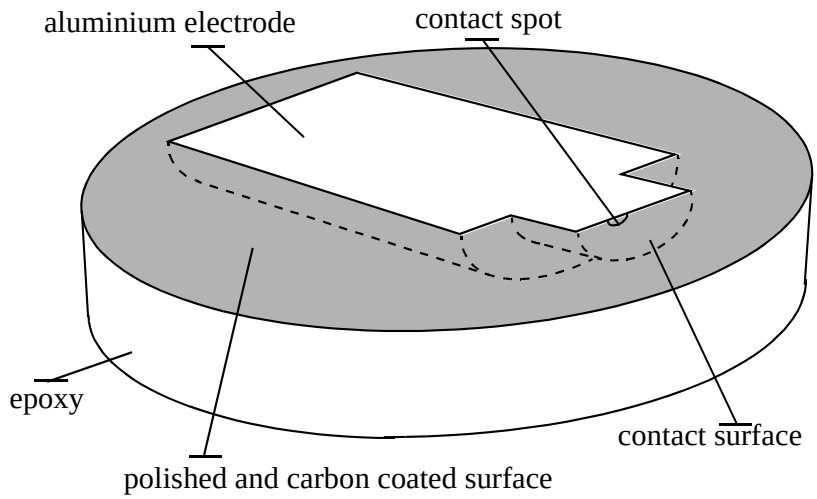

Figure 3.7: Cross sectioned electrode embedded in epoxy with carbon coated surface

down until the contact spot was reached, see Fig 3.7. This process required great care in the preparation of the cross section. In order to avoid that the contact spot fracture was irrevocably ground away the distance from the cross-sectioned surface to the contact spot fracture was estimated by observing the contact surface through the transparent epoxy with an optical microscope. The newly attained cross section was polished with polishing-emulsion to 0.04 µm surface roughness. The surface of the polished epoxy specimen was carefully cleaned and then made conductive by carbon-coating, so it could be examined by SEM. This made it possible to take a closer look on the appearance and structure of the aluminium within the electrode and directly under the contact spot fracture. When zinc-tracer had been alloyed into one of the electrodes of the contact, backscatter-electron-imaging revealed the zinc-distribution in the electrode-bulk (element-number-contrast).

A verification of the zinc-tracer distribution as observed by backscatter-electron imaging could be accomplished by the EDA. In addition, the EDA was used to identify impurities in the electrodes.

3.5 Examination by optical microscope

Metallographic images of the cross-sectioned electrodes were obtained by anodizing and examining the surface with an optical microscope. As described

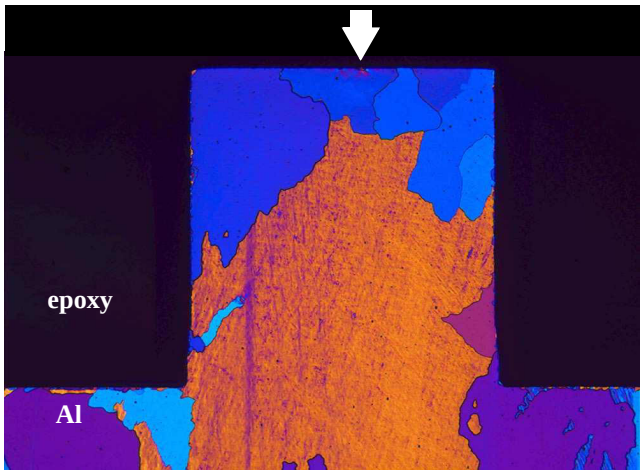

Figure 3.8: Metallographic image of cross-sectioned upper electrode. The cross-sectioned contact spot (under the arrow) is barely visible

before the cross-sectioned electrodes have to be polished with polishing emulsion. The polished aluminium was anodized by electrochemically growing an oxide-layer (Al_2O_3) on the surface. The thickness of this new oxide layer, generally in the order of 100 nm, depends on the orientation of the crystal lattice of the aluminium grain underneath. When illuminating the anodized surface with polarized light, the different grains can be distinguished because the different levels of the oxide on top of them appear in different colour hues. This effect is caused by interference contrast on the oxide layer and can then be observed by optical microscope. A typical example is shown in Fig. 3.8. A distinct contrast in colour of neighbouring grains usually indicates a greater difference in the angle of lattice orientation.

4

Examination of Conducting Spots in Aluminium-Aluminium Contact Interfaces

4.1 Introduction

In the following sections the experimental results from an extensive study of contact spots between aluminium conductors are presented. The results come from 69 experiments carried out according to the methods described in Chapter 3. The main emphasis was put on experiments where AC was applied to the contact, but some experiments were carried out using DC or rectified AC, so the effect of temperature cycling and current direction could be evaluated. Previously published work using the same experimental setup [17] only includes DC-experiments.

At first some typical examples of the voltage, current and temperature development recorded during the experiments are presented in Section 4.2. The next part (Section 4.3) gives an insight into contact spot fracture appearance with different current wave shapes applied to contacts made from various aluminium-alloys. In Section 4.4 follows a thorough examination of cross sectioned contact spots, focusing in particular on the cracks found in the electrodes close to the contact spots. Metallographic images presented in Section 4.5 show the effect of the temperature cycling on the electrode material. The results of experiments where zinc as a tracer was used in one of the electrodes are presented in Section 4.6. The examination of possible porosities in the contact spot region is described in Section 4.7 and irregularities in the contact resistance are documented in Section 4.8.

4.2 Voltage, current and temperature recording

The voltage across the contact U_c, the current I and the bulk temperature T_0 of the electrodes were recorded for each experiment. Fig. 4.1 shows the 50 Hz sine wave current and the voltage across the contact over a 40 ms time span as it could be observed on the oscilloscope. Voltage and current are in phase but the wave shape

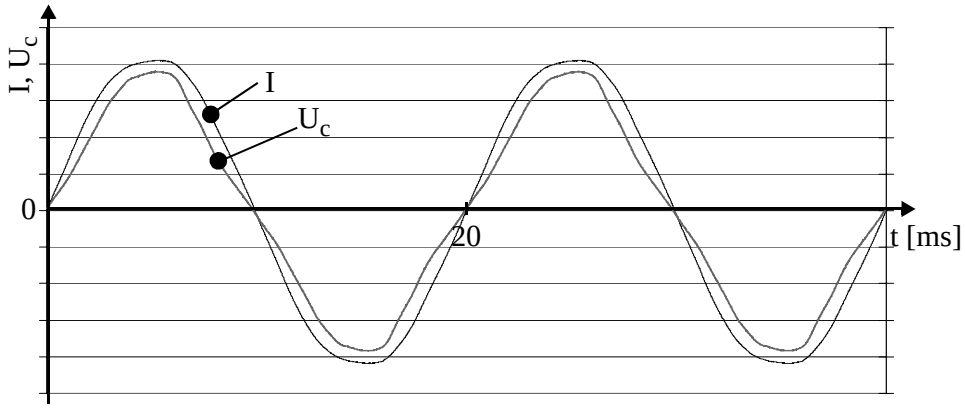

Figure 4.1: Sinusoidal current I and slightly distorted sinusoidal voltage across the contact U_c

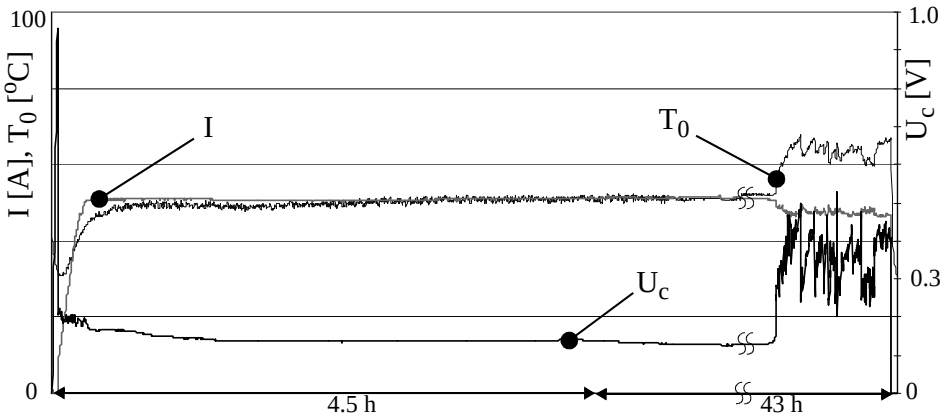

Figure 4.2: Current I, voltage Uc and bulk-temperature T_0 recorded in an experiment where 50 A AC were applied to pure aluminium electrodes for 48 hours

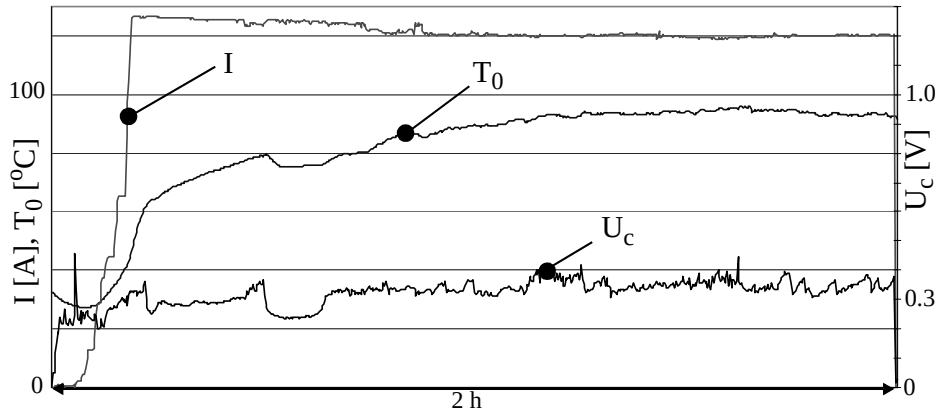

Figure 4.3: Current I, voltage Uc and bulk-temperature T_0 recorded in an experiment where 125 A AC were applied to technically pure aluminium electrodes for 2 hours

of the voltage is not perfectly sinusoidal as it has been discussed in Section 2.2. The value of the contact resistance is obtained from the peak values of voltage and current according to (3.1).

In Figs 4.2 and 4.3 the voltage, current and bulk-temperature as they were recorded by data-logger for two different experiments can be seen. Fig 4.2 shows the recorded curves for U_c, I, T_0 of an experiment where the contact was made from pure aluminium and carried I = 50 A AC for nearly 48 hours. The sampling rate f_s for the first 4.5 hours was set to once every ten seconds (f_s = 0.1 Hz) so that variations in U_c while increasing I to the desired level could be traced more accurately. For the remaining 43 hours the sampling rate was set to once every minute f_s = 0.016 Hz.

The voltage spike which can be seen at the start of the plot in Fig. 4.2 indicates the fritting voltage U_c= 0.95 V. No metal-to-metal contact has been established yet and the voltage is increased in small steps of ΔU = 50 mV per second until fritting occurs. The voltage then drops to U_c= 0.2 V, decreasing further while the current is slowly increased to its desired level of I = 50 A. This process takes approximately 15 minutes. Whenever the current is increased for another step ΔI = 500 mA the voltage U_c shortly rises approximately 10% and subsequently sinks back down to its initial value or even below as it was before the current was increased with ΔI. These variations in U_c while increasing the current are steady and take less than 10 seconds each.

Due to the heating of the electrodes during assembly the bulk-temperature T_0 is initially at T_0 = 40 ^oC, then falls slowly to T_0 = 30 ^oC upon which it again increases with increasing current to its steady state value of T_0 = 50 ^oC which is attained after approximately 30 minutes.

After the current is set to I = 50 A the voltage gradually sinks from U_c = 0.165 V to U_c = 0.13 V while the current remains constant at I = 50 A. From this the contact resistance can be determined to approximately R_c = 2.6 mΩ. After 41 hours the contact resistance increases as can be seen from the increase of the contact voltage. This is accompanied by a drop in the current to I = 45 A and an increase in bulk-temperature to T_0 > 60 ^oC. The contact becomes unstable as its resistance increases and decreases unpredictably during intervals of only a few minutes. The contact voltage rises above the melting voltage for aluminium (U_c > 0.3 V). Due to the low sampling rate it appears from Fig. 4.2 as if the variations of the contact resistance were abrupt and unsteady. This will be dealt with in detail later on in this section.

Fig. 4.3 shows similar to Fig. 4.2 the curves of voltage U_c, current I and bulk-temperature T_0 as recorded for another experiment. In this case the electrodes were made from commercially pure aluminium and the contact carried 125 A AC for 2 hours. The sampling rate was set to $f_s = 0.1$ Hz throughout the experiment. As in Fig. 4.2 the fritting voltage can be read from the peak at the beginning of the U_c-curve as $U_c = 0.45$ V and also the bulk-temperature is initially higher than the ambient temperature at $T_0 = 32^o$ C. The maximum bulk-temperature is attained after 90 minutes at $T_0 = 95\ ^oC$.

Apart from a period of only a few minutes approximately 30 minutes into the experiment, the contact voltage was above the melting voltage $U_c > 0.3$ V during almost the entire experiment. Also in this case the variations in U_c show the unpredictable rising and falling of the contact resistance during short intervals which is a sign for an unstable contact. The contact resistance has its minimum during the short period when there are nearly no variations in U_c at $R_c = 1.9$ mΩ.

The unpredictable and unsteady behaviour of the contact voltage U_c is documented more detailed in Fig. 4.4. On the left side the U_c-curve is shown over a five-power-cycle-interval (100 ms). A gradual increase of U_c during the first three cycles from 0.396 V to 0.406 V is observed, culminating in a 0.444 V peak and immediate drop to 0.339 V on the fourth cycle. This is shown in detail on the right side of Fig. 4.4. Already on the fifth cycle the contact voltage can again be seen to be rising gradually.

From Fig. 4.2 and Fig. 4.3 it can be seen that the contact resistance and bulk-temperature are not constant throughout the experiment. Consequently the values

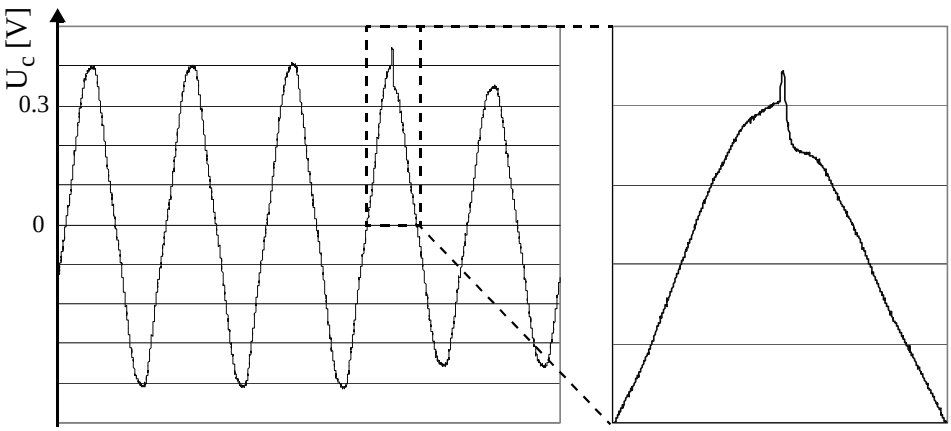

Figure 4.4: Gradual increase and abrupt drop of contact voltage U_c, five-cycle period (left), enlarged detail (right)

given indicate the order of magnitude of the contact resistance and the bulk-temperature respectively. For the majority of the experiments they were found to be in the order of magnitude as it can be derived from the curves shown in Fig. 4.2 and Fig. 4.3; the contact resistance R_c usually was a few milli-ohms while the bulk temperature T_0 was in the range from 30 ^oC to 130 ^oC.

Fritting as it was observed with the experiments described above occurred with 44 out of 69 experiments but it did not appear to have any effect on the subsequent behaviour of the contact.

4.3 Examination of the contact spot fractures

When separating the electrodes the metallic contact is ruptured and only fracture marks remain as a rough profile at the position of the conducting spot, clearly distinguishable on the otherwise polished surface. These fracture sites are commonly referred to as contact spot fractures.

In Fig. 4.5a contact spot fracture on the polished contact surface of an upper electrode is shown in different magnifications. The images were taken by SEM using secondary electron emission. The contact spot was generated by passing 125 A AC for 3 hours through the contact. The electrodes were made from commercially pure aluminium AA1350 as commonly used for electrical conductors. The contact spot fracture as it appears on the polished contact surface, the apparent contact area, is shown in Fig. 4.5a. Figure 4.5b gives an impression of the surface texture of the contact spot fracture, which again is shown in greater detail in Fig. 4.5c. It can be seen that the contact spot fracture does not have a very distinct profile in that only small protrusions and pits of similar height and depth are distributed rather uniformly across the fracture surface. The height of the most outstanding protrusions is only a few micrometer above the contact surface. The appearance of a contact spot fracture as shown in Fig. 4.5a-c is characteristic for aluminium contacts where AC was applied to. It was observed in 51 of the 54 experiments where AC was applied.

A typical DC contact spot fracture is shown in Fig. 4.6. The contact spot was made by passing 90 A DC for 9 days through the electrodes. On the anode (left side) the characteristic protrusion can be seen as it is found with all DC contact spot fractures. The corresponding pit as it appears in the cathode is shown on the right side of Fig. 4.6. When separating the electrodes the metal-to-metal contact

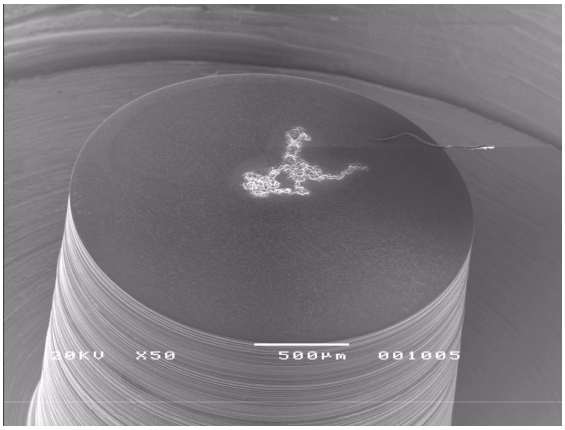

Figure 4.5a: SEM image of contact spot fracture on the polished surface of an upper electrode after passing 125 A AC, seen at an angle of 45^{o}

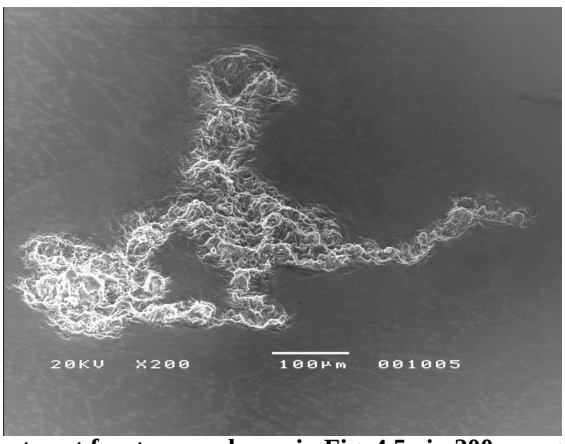

Figure 4.5b: Contact spot fracture as shown in Fig. 4.5a in 200x magnification. The surface texture is characteristic for AC contact spot fractures

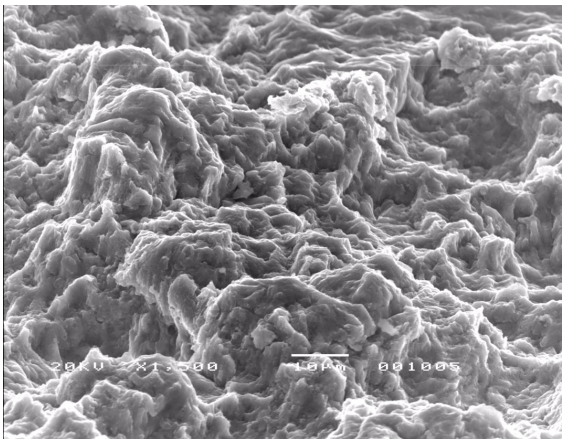

Figure 4.5c: Contact spot fracture as shown in Fig. 4.5a in 1500x magnification. The profile of the fracture can be examined in detail

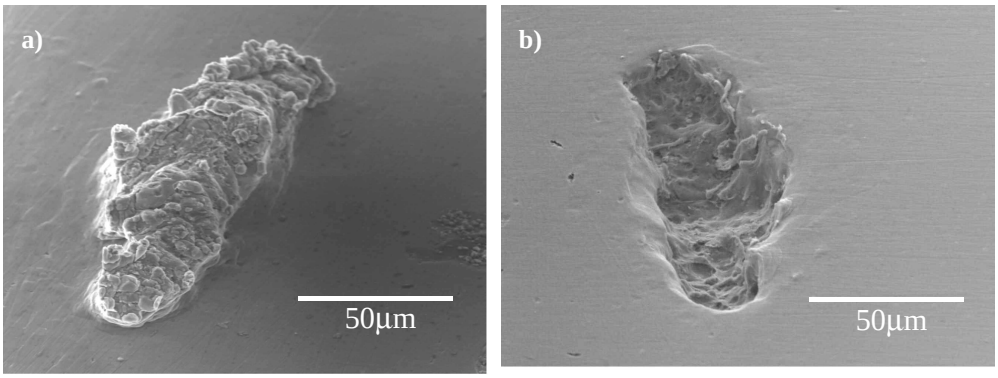

Figure 4.6: SEM image of DC contact spot fracture, the anode with the typical protrusion (a), the cathode with the corresponding pit viewn from an angle of 45^{o} (b)

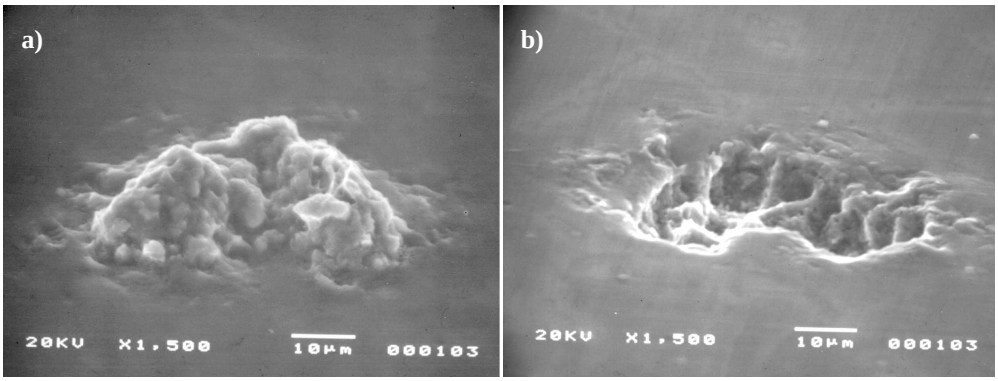

Figure 4.7: SEM image of contact spot fracture as it appears when rectified AC was applied to the contact, a) anode, b) cathode.

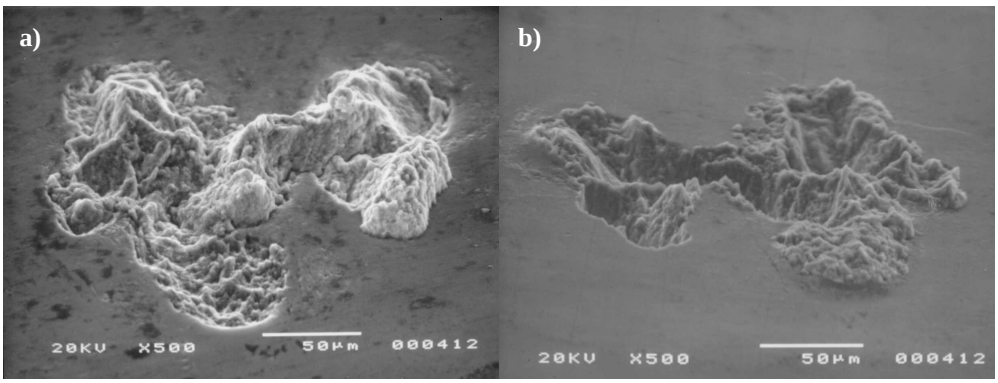

Figure 4.8: Contact spot fracture after applying 100 A AC to a contact where one electrode was made from pure aluminium (a) , the other electrode contained 10% zinc (b).

fractures always inside the cathode, resulting in the protrusion on the anode and the pit in the cathode as shown.

A contact spot fracture with similar protrusion/pit-appearance as the one described above is shown in Fig. 4.7. However, this one has not been generated by passing continuous DC through the contact, but in this case rectified AC was applied. In order to do this the 50 Hz AC supplied from the power supply was rectified with a rectifier bridge, so that the current wave shape consisted of sinusoidal semi-cycles pulsating with 100 Hz frequency. The amplitude of the current was 50 A. On the left side of Fig. 4.7 the characteristic protrusion on the anode-surface is shown, the right side shows the corresponding pit in the cathode.

When conducting experiments with contacts where one electrode was made from AlZn10-alloy, the contact spot fractures observed with AC and rectified AC experiments were of similar appearance as those found on electrodes made from commercially pure aluminium. A severely aged AC contact spot fracture is shown in Fig. 4.8. The contact carried 100 A AC for 4 days. On the left side the electrode made from pure aluminium can be seen, the electrode containing 10% zinc is shown on the right side. The contact spot fracture exhibits the same characteristics as described before (ref. Fig. 4.5b), though the profile is considerably more distinct in this case, i.e. the pits are deeper and the protrusions are higher.

The contact spot fracture shown in Fig. 4.9 stems from a contact spot which carried 40 A rectified AC. Both electrodes of this contact were machined from pure aluminium. Fig. 4.9 shows a secondary electron SEM image of the cathode. This contact spot fracture does not exhibit the characteristic protrusion-pit-appearance as it would have been expected with a contact where rectified AC was applied and as it always is observed when applying continuous DC to pure aluminium electrodes. Its appearance resembles rather a typical AC contact spot fracture as shown for example in Fig. 3.6 and Fig. 4.5b.

Fig. 4.10 shows a contact spot fracture which carried 100 A rectified AC for 2 hours. On the left side the anode with the characteristic protrusions can be seen. The contact spot fracture appears like an irregular mesh of tracks all over the electrode surfaces. In this case the anode had 10% zinc alloyed into it. The protrusions are the result of material transport from the cathode made from pure aluminium. This is made visible in Fig. 4.10b where a part of the contact spot fracture is shown as an element-contrast image made by using the backscatter-electron detector of the SEM. The light areas are zinc-enriched where the dark grey areas of the contact spot fracture are deposits originating from the pure

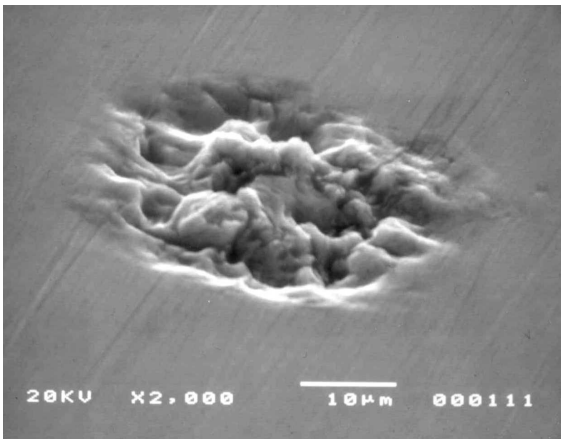

Figure 4.9: Contact spot fracture on electrode of pure aluminium where 40 A rectified AC were applied with AC contact spot appearance (cathode is shown)

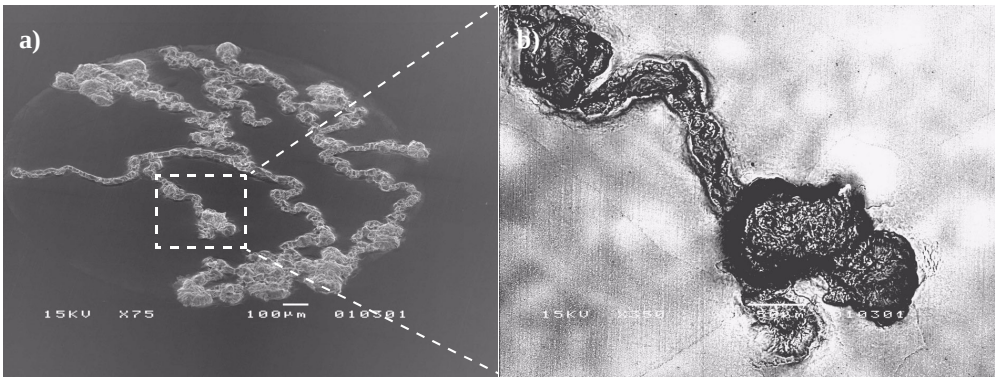

Figure 4.10: Contact spot fracture that carried 100 A rectified AC, the anode (a) contained 10% zinc, the cathode was made from pure aluminium. The element-contrast SEM-image (b) shows in 750x magnification the protrusions (dark grey) on the zinc-enriched surface (white)

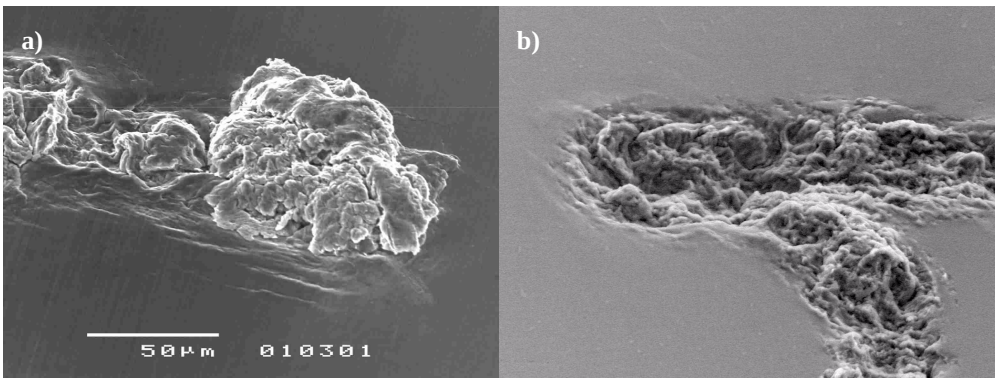

Figure 4.11: Enlarged detail of Fig. 4.10 with small ridges bordering the contact spot fracture (a), AC contact spot fracture with similar ridges around its contour (b)

aluminium cathode. However, the protrusions were not of pure aluminium, but contained approximately 5% zinc, as determined by EDS.

In Fig. 4.11 two different contact spot fractures can be seen. On the left side an enlarged detail of the contact spot fracture shown in Fig. 4.10 is shown. It can be seen that the protrusion at the end of a track is bigger and definitely more distinct than the rest of the track leading towards it. In addition to that small ridges are found on the electrode surface in close vicinity around the fracture. Fig. 4.11b shows a part of a typical AC contact spot fracture, which also has small ridges along the contour of the fracture. These ridges are a few micrometer in height and can only be observed on carefully polished contact surfaces. They have been observed with AC as well as with rectified AC contact spot fractures. It does not appear as if they were caused by the mechanical forces present when separating the electrodes, but have been there already before. The ridges are always found on both electrodes (upper and lower) but not in corresponding positions i. e. independently from one another. However, these ridges have not been observed with DC contact spot fractures.

In Figs. 4.12 to 4.14 several AC contact spot fractures of various size and of more or less distinct characteristic appearance are shown. All contacts were made from commercially pure aluminium apart from the one shown in Fig 4.14b, which was made from pure aluminium.

The contact spot fracture shown in Fig. 4.12a carried 125 A AC for 1 minute. Its diameter is approximately 60 µm. In comparison to that the contact spot fracture shown in Fig. 4.12b carried 75 A AC for 9 days. The area of its contact spot fracture is approximately 5 times smaller than the area of the contact spot fracture shown in Fig. 4.12a.

The contact spot fractures shown in Fig. 4.13a and b are of considerably larger size than those shown in Fig. 4.12. The contact spot from Fig. 4.13a carried 125 A AC for 4 hours. The contact spot fracture seen in Fig. 4.13b is of similar appearance and size. It carried 140 A AC for 24 hours. Both fractures show initial stages of tracks as they were already observed in Fig. 4.10.

In Fig. 4.14 two contact spot fractures of severely deteriorated contacts can be seen. The contact spot fracture shown in Fig. 4.14a carried 125 A AC for 2 hours. The profile of this fracture is more distinct as it is with the contact spot fractures shown in Fig. 4.12 and Fig. 4.13. The protrusions are higher and the pits are deeper. Furthermore the protrusions can be seen to be partly disconnected from the electrode as small cracks appear underneath them. This becomes particularly

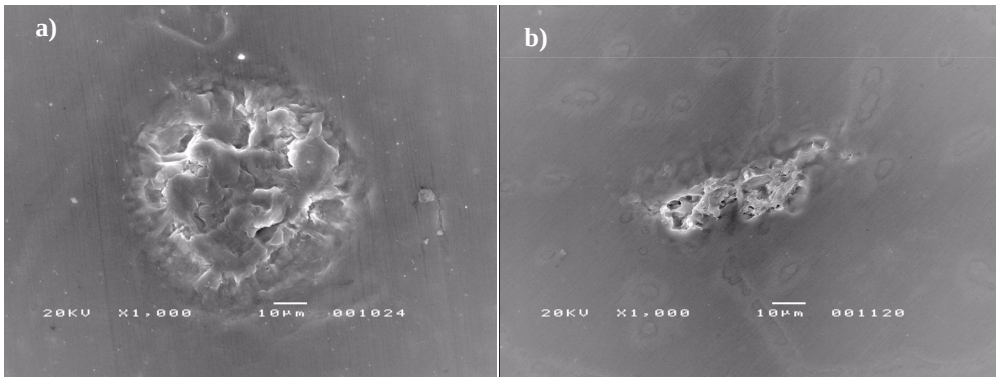

Figure 4.12: AC contact spot fractures on commercially pure aluminium
a) carried 125 A AC for 1 minute
b) carried 75 A AC for 9 days

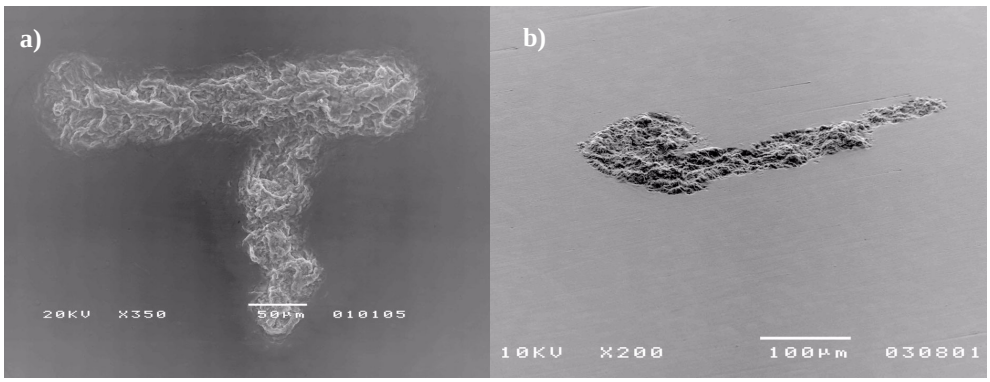

Figure 4.13: AC contact spot fractures on commercially pure aluminium
a) carried 125 A AC for 4 hours
b) carried 140 A AC for 24 hours

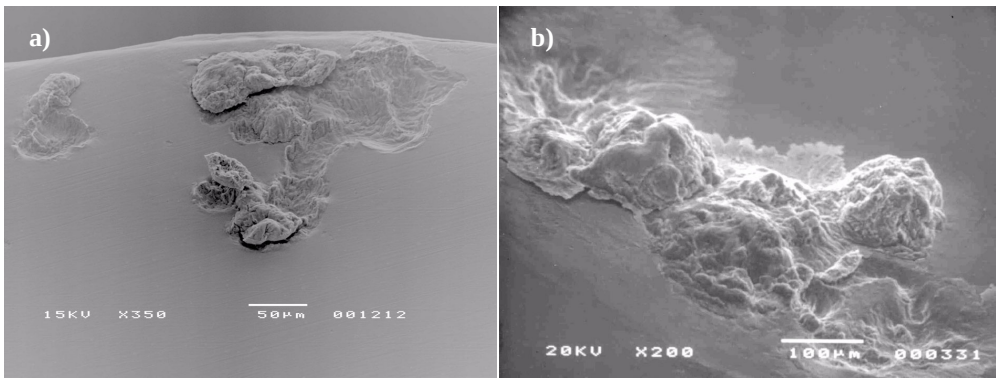

Figure 4.14: Severely deteriorated AC contact spot fractures
a) commercially pure aluminium, carried 125 A AC for 2 hours
b) pure aluminium, carried 50 A AC for 36 hours

visible when regarding the lens-shaped bit of metal in the center of Fig. 4.14a which became nearly ripped out of the surface when the electrodes were separated.

Figure 4.14b shows a contact spot fracture which carried 50 A AC for 36 hours. Its appearance with particularly high protrusions and deep pits in the surface is similar to the fracture shown in Fig. 4.14a. In addition to this flakes of apparently molten and subsequently solidified aluminium spreading from the fracture onto the electrode surface can be detected.

When comparing the contact spot fractures shown in Fig. 4.12 to Fig. 4.14 it can be seen that the size of the fracture depends on the amplitude of the current passed through the contact as well as on the duration by which it was applied to the contact. Furthermore it can be stated that the profile of severely aged AC contact spot fractures becomes more pronounced, as the characteristic pits and protrusions are larger.

Another finding regarding the appearance of contact spot fractures which can be derived from the images shown above is that with DC contact spot fractures always a pit with corresponding protrusion will be found on the contact surface, whereas an AC contact spot fracture typically has a less well defined and distinct profile. These findings are widely independent of the electrode material used.

4.4 Examination of cross sectioned contact spots by SEM

In the following some results of SEM examinations of cross sectioned contact spots are presented. The epoxy-embedded electrodes were ground down to the contact spot fracture as described in Chapter 3 in order to study of the region beneath the contact spots. SEM images of cross sections of AC-, DC- and rectified AC- contact spot fractures are shown.

Figs. 4.15a - f show SEM images taken with secondary electron detection of an AC contact spot fracture and its cross sections. This contact carried 107 A AC for 2.5 hours. The contact spot fracture can be seen on the polished electrode surface in Fig. 4.15a. The dashed line indicates the orientation of the cross sections as they are shown in the other images. The part of the electrode to the lower right of the dashed line was ground away, leaving the part to the upper left of the dashed line in the epoxy. In Fig. 4.15b the typical appearance of a cross-sectioned AC contact spot fracture can be seen. The profile of the fracture can clearly be distinguished against the carefully polished surface.

Figs. 4.15c - f each shows a new cross section of the contact spot fracture, beginning with Fig. 4.15c followed by Figs. 4.15d - f which lie deeper within the embedded electrode. The spacing between each of the cross sections is only a few micrometer. By doing so the small cracks appearing in the fracture surface can be traced into the material. The detection of these cracks in the fractures requires careful polishing also of the cross-section prior to SEM examination. In some images stripes across the cross sectioned metal surfaces can be seen. These stem from the grinding and polishing process.

Cross sectioning of an AC contact spot fracture allows detailed analysis of the shape of the pits and protrusions visible on the electrode surface. In this case rifts and cracks of approximately 20 µm length extending into the electrode could be discovered. They were not visible on the electrode surface. The small crack visible to the right of the cross sectioned fracture separates a tiny chunk of aluminium almost completely in Fig. 4.15f. However, in the preceding cross sections it could be seen that it still is connected to the electrode. Small cracks bordering the fracture and occasionally separating tiny aluminium chunks from the electrode could often be observed when the contact resistance showed unstable behaviour during the experiment.

The embedded aluminium particle above the fracture in Fig. 4.15f is a remnant from the protrusion at the center of Fig. 4.15e. The white line separating the epoxy and the aluminium in Fig. 4.15f owes to static negative charges from the electron

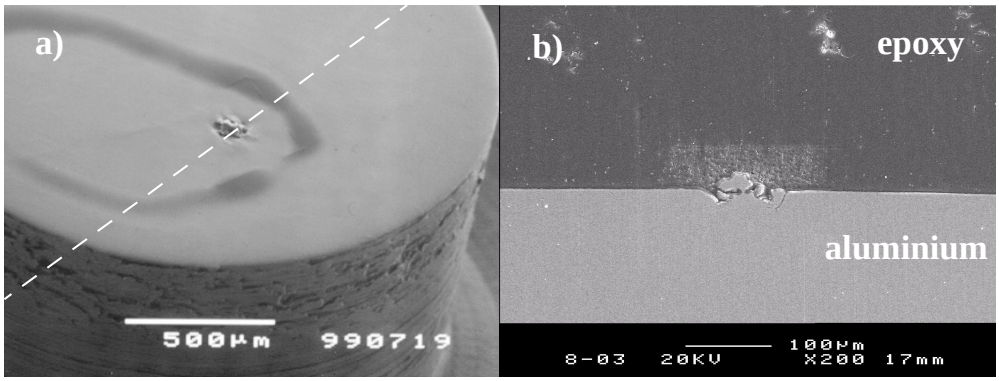

Figure 4.15: a) AC contact spot fracture on polished electrode surface, the dashed line indicates the orientation of the cross section
b) Cross section of an AC contact spot fracture, the profile can easily be distinguished against the polished electrode surface

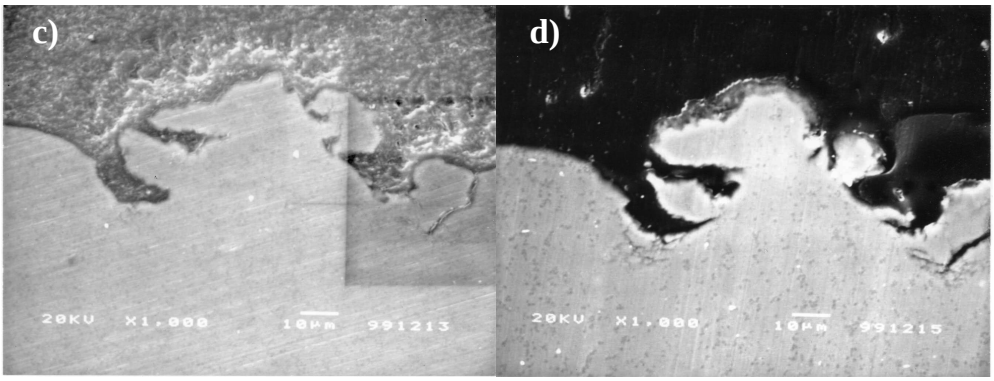

Figure 4.15: c) SEM image of the cross section along the dashed line of the contact spot fracture shown in a)
d) Same as c) but a few micrometer deeper into the electrode

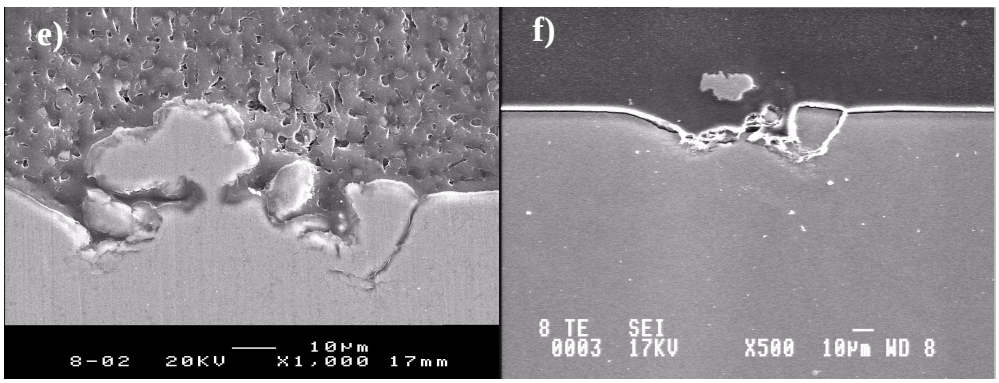

Figure 4.15: e) Further cross section of a), deeper into the electrode than d) and magnification of b)
f) Same as e) but deeper into the electrode

beam of the SEM due to edge imperfections in the carbon-coating, impeding the charges to be removed.

In Figs. 4.16a and b another AC contact spot cross section is shown. It is a cross section through the track visible to the very right on the contact spot fracture shown in Fig. 4.5b. Figure 4.16a was taken using the secondary electron detector, Fig. 4.16b is an image of the same cross section taken with the backscatter electron detector of the SEM. Comparing Fig. 4.16a with b it can be seen that the cracks which appear underneath the protrusion are easier detected in b. The cracks do not completely engulf the protrusion: it still has a mechanical connection to the electrode. In addition to that the black dots in the metal underneath the contact spot fracture are only faintly visible in Fig. 4.16a but become more distinct and more numerous in Fig. 4.16b.

The cross section of a contact spot fracture similar to the one shown in Fig. 3.6 can be seen in Fig. 4.17a. The contact carried 65 A AC for 36 hours. The contact spot fracture has a low profile which is difficult to detect against the cross sectioned electrode surface. The pits and protrusions are only a few micrometers in depth and height. No cracks or any other sign of material deterioration could be detected in the metal underneath the contact spot fracture by the SEM examination.

In Fig. 4.17b a cross section of one part of the contact spot fracture shown in Fig. 4.10 is shown. The contact carried 100 A rectified AC and the characteristic protrusion can be seen to be approximately 20 µm in height above the polished anode surface. Also in this case cracks are clearly visible underneath and as well within the contact spot fracture separating the protrusion from the anode apart from a narrow mechanical connection at the center.

The cross sectioned contact spot fracture shown in Fig. 4.18a is from the anode of the DC contact spot fracture shown in Fig. 4.6, and Fig. 4.18b is the corresponding cross section of the cathode contact spot fracture. It can be seen that the characteristic protrusion rises approximately 30 µm above the anode surface. The depth of the pit in the cathode is accordingly. No cracks can be detected underneath the protrusion or the pit. The opening which appears to the right of the cross sectioned pit is not a crack as those described above, but it originates from the pit extending further to the right in the cathode being only partly cut away during the cross sectioning. The white dots and lines which can be seen in the metal are Al_3Fe-precipitates which formed within the grains and along the grain boundaries.

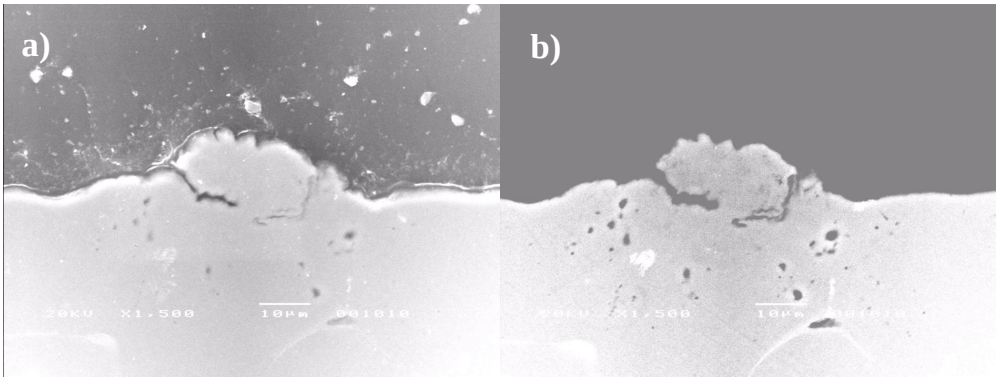

Figure 4.16: Image of cross section of an AC contact spot taken by
a) secondary electron detection and
b) by backscatter electron detection (cf. Fig. 4.5a)

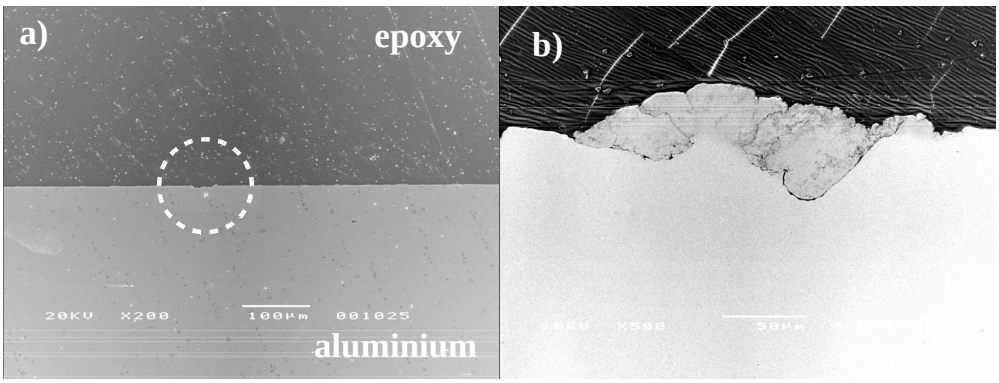

Figure 4.17: a) Cross section of an AC contact spot fracture with low profile
b) Cross section of a rectified-AC contact spot fracture with several cracks underneath and within the protrusion (ref. Fig. 4.10)

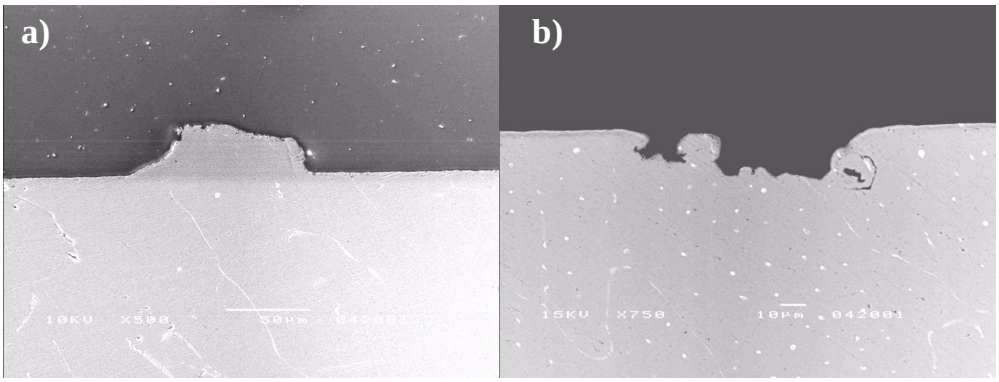

Figure 4.18: a) Cross section of DC contact spot fracture (anode)
b) Cross section of corresponding fracture on cathode

The images presented above were chosen from the 25 out of 69 contacts that were successfully cross sectioned. Many of these were cut in several planes in order to obtain tomographic pictures of the contact spot fracture as in Fig. 4.15. It could be observed that cracks exclusively were found in fracture cross sections where the pits and protrusions were particularly distinct, i. e. with more or less severely deteriorated contacts, which again could be linked to unstable electrical behaviour as described in the previous sections. The cracks were always located underneath a protrusion, there were no cracks observed in the electrode underneath the corresponding pits. No cracks were found with cross sectioning of DC contact spot fractures. In general it can be said that all the cracks apparently had their origin at the contact surface.

The development of cracks appears to be independent of the alloy used for the electrodes: cracks were observed in electrodes made from pure, commercially pure and zinc-enriched aluminium as well.

The fine cracks become more visible when examining the cross section using the backscatter detector of the SEM. This is due to the fact that the backscattered electrons give an element-contrast image, where elements with an atomic number lower than aluminium appear darker and elements having a higher atomic number appear lighter, according to the number of backscattered electrons detected. Directly at a crack in the metal and also in its close vicinity, considerably less electrons become scattered back to the detector so that the crack appears dark black and also wider than with secondary electron detection. In addition to that the backscattered electrons originate from greater depth into the metal compared to secondary electrons, allowing the detection of particles, pores and cracks hidden under the cross section surface.

The different shades of grey in a cross sectioned protrusion and as well the black dots observed underneath it will be dealt with later on.

4.5 Metallographic images of cross sectioned contact spots

The purpose of the metallographic examination of the specimens is to make its internal microscopical structure visible and determine its properties as for example the grain size. Metallographic images give information about the manufacturing conditions of the metal as well as its behaviour when exposed to various stresses. In the following metallographic images of cross sectioned and anodized aluminium electrodes will be presented.

The metallographic image of the cross sectioned AC contact spot fracture shown in Fig. 4.19 is nearly identical to the cross section shown in the SEM-image in Fig. 4.15. The embedded electrode was ground down a few more micrometers in order to remove the carbon coating prior to anodizing. The crack is faintly visible to the right of the cross sectioned contact spot fracture. The neighboring grains in the metal can be distinguished by their different colours. It can be seen that the contact spot fracture and the metal in immediate vicinity are characterized by many small adjacent grains embedded within one large grain. The small grains vary in size from approximately 1 µm to 20 µm. They cluster around the contact spot fracture so that there is no smooth transition in grain size with increasing distance from the fracture into the metal.

In Fig. 4.20 another metallographic image of a cross sectioned contact spot fracture is shown. An enlarged view of this cross sectioned electrode was presented in Fig. 3.8, the surface of the fracture was shown in Fig. 4.8. The contact carried approximately the same current as the one described above. But the duration of this experiment was four days compared to 2.5 hours as above. However, the appearances are similar. Also in this case the small grains vary in size from approximately 1 µm to 20 µm and are clustered around the fracture and they are embedded within one large grain (size approx. 0.5 mm). It can be seen more clearly that the protrusion is made up from many small grains. The transition in grain size from small grains to large grains is rather abrupt as observed above in Fig. 4.19.

The contact spot fracture shown in cross section in the metallographic image presented in Fig. 4.21 is identical to the one seen in Fig. 4.12a. Whilst the amplitude of the applied current can be compared to the current applied with the two previously described contacts, the duration of this experiment was only one minute. It can be seen that even with a relatively short time span of AC application the metallographic image of the contact spot fracture cross section shows the characteristic appearance of a great number of small grains embedded into a larger grain. In this particular case the cluster of small grains extends into a second large

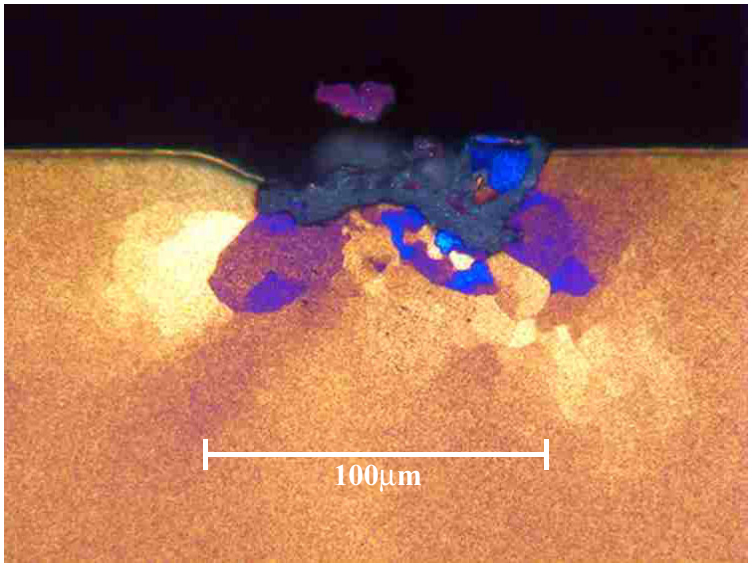

Figure 4.19: Metallographic image of the AC contact spot cross section shown in the SEM-image Fig. 4.15f. This contact carried 107 A AC for 2.5 hours.

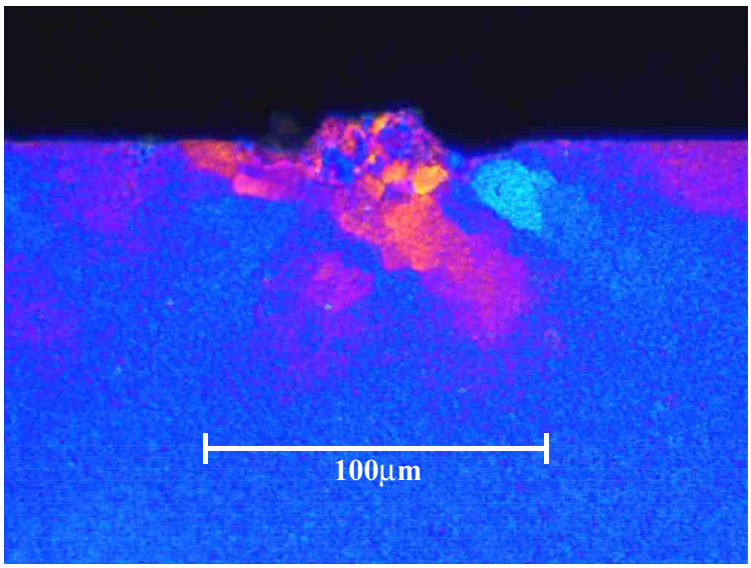

Figure 4.20: Metallographic image of AC contact spot cross section that carried 100 A AC for four days

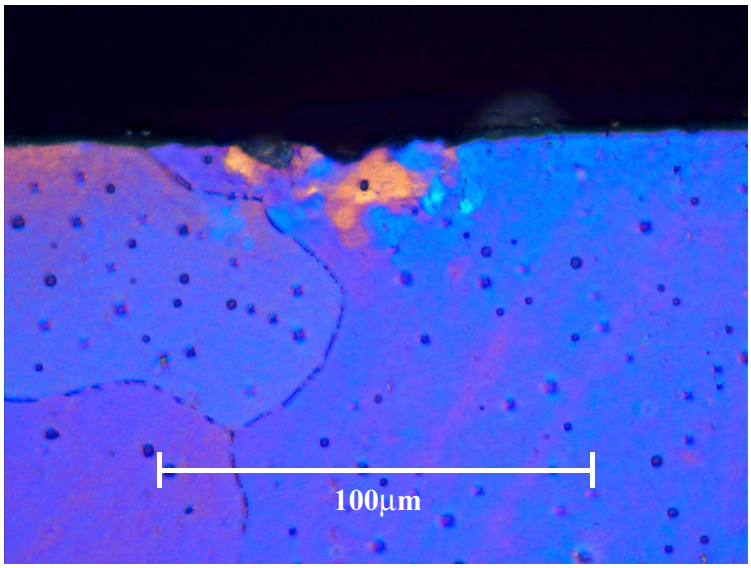

Figure 4.21: Metallographic image of AC contact spot cross section that carried 125 A AC for one minute

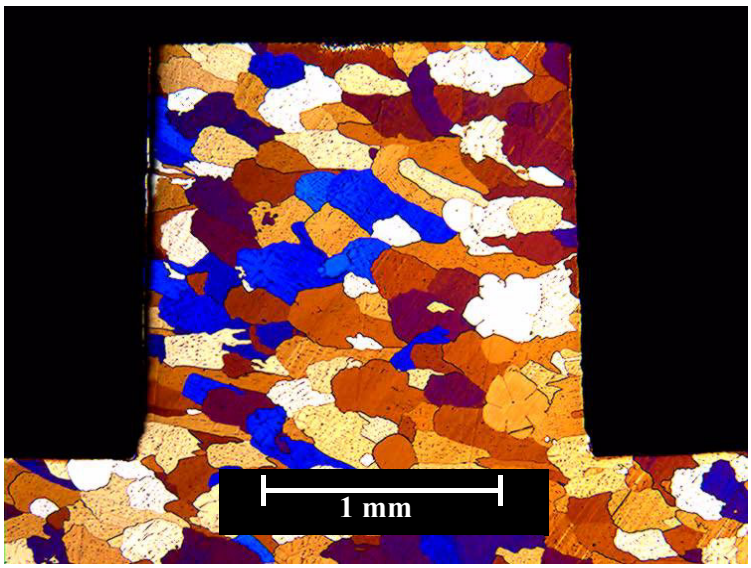

Figure 4.22: Anodized aluminium electrode made from cast aluminium AA1350, the cluster of small grains visible at the top indicates the location of the cross sectioned contact spot fracture

grain in immediate vicinty. The grain boundaries of the large grains appear as black lines. The black dots visible all over the anodized metal surface are Al_3Fe-precipitates. The spread in the average size of the small grains in this contact spot is approximately the same as in those described above.

Figure 4.22 shows the metallographic image of a larger portion of an electrode. As before a cluster of small grains visible at the top center of the anodized metal surface indicates the location of the contact spot fracture. SEM-images of this fracture where shown earlier in Figs. 4.5a and 4.16. It can be seen that the grain size distribution across the electrode is unaffected by the contact spot and that a cluster of small grains as it typically is found around the contact spot fracture is not observed anywhere else. The appearance of the large grains seen in the electrode bulk is characteristic for cast aluminium.

The metallographic image shown in Fig. 4.23 is a cross section of the contact spot fracture on the electrode opposite to the one described in the preceeding paragraph. From this it can be seen that the clusters of small grains are found on both electrodes, having nearly identical appearance. This is usually observed with contact spot fractures with low profile, i. e. where no extraordinary protrusions and cracks, as described in Section 4.4, were observed. By comparing Fig. 4.23 with Fig. 4.24 it can be shown that the appearance and clustering of small grains close to the contact spot fracture is independent of the degree of deformation of the metal. The cross sectioned and anodized electrode that can be seen in Fig. 4.24 was made from cold worked aluminium AA1350. This is indicated by the flattened and elongated appearance of the larger grains. A SEM-image of the surface of the contact spot fracture was shown earlier in Fig. 4.13b.

Figs. 4.25 and 4.26 show metallographic images of the cross sectioned protrusion appearing on the anode and a pit as it is found on the cathode of a contact which carried rectified AC. The cross section shown in Fig. 4.25 is the same as it was shown in Fig. 4.17b. The cracks observed earlier can clearly be distinguished and as with AC contact spots, small grains cluster close to the fracture. The protrusion consists entirely of small grains. Regarding the anodized cross section of the corresponding pit in Fig. 4.26 it appears as if the majority of the small grains remained with the protrusion upon separating the electrodes and only a few were left in the cathode. However, also the pit is embedded within a large grain as it was observed with the clusters of small grains before.

In Figs. 4.27 and 4.28 metallographic images of the cross sectioned DC contact spot fracture already presented on SEM images in the previous Sections in Fig. 4.6 and Fig. 4.18 are shown. An overview of the general appearance of the grains in

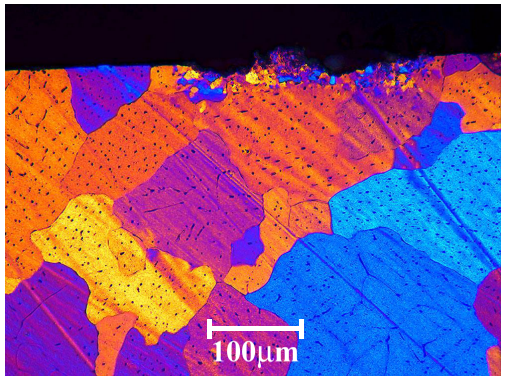

Figure 4.23: Metallographic image of the cross section of the contact spot fracture found on the electrode opposite to the one shown in Fig. 4.22

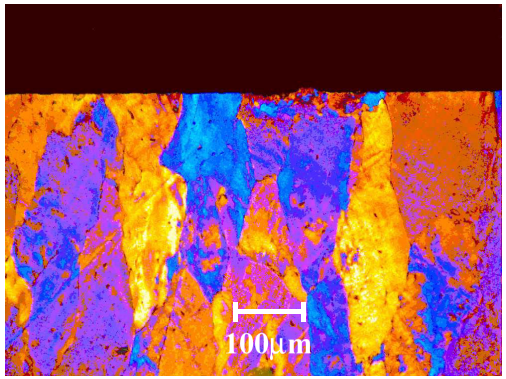

Figure 4.24: Anodized cross section of a contact spot fracture as it appears on a cold worked aluminium electrode. This contact carried 140 A AC for 24 hours.

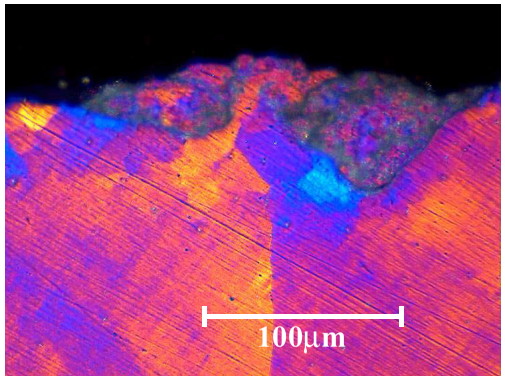

Figure 4.25: Metallographic image of the anode of a cross sectioned contact spot fracture which carried 100 A rectified AC

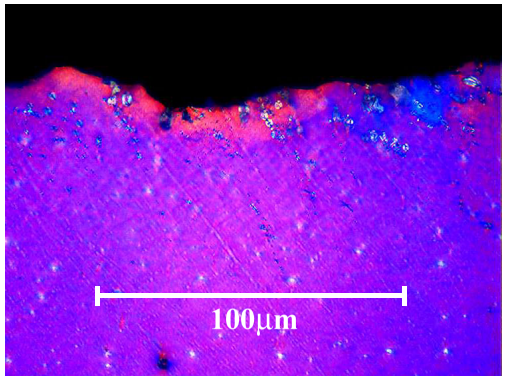

Figure 4.26: Metallographic image of the cross sectioned pit found on the cathode corresponding to Fig. 4.25

the electrodes regarding their size and structure is given in Fig 4.27a (anode) and Fig. 4.28a (cathode). While some very large grains, to 1 mm wide, are found in the anode, the cathode appears similar to the electrode shown in Fig. 4.22. It can very well be seen that the protrusion as well as the pit are part of respectively are embedded within larger grains. Figures 4.27b and 4.28b show enlarged images of the protrusion and the pit. Neither with the protrusion nor with the pit small grains clustering close to the contact spot fracture could be detected. The lighter areas on top of the protrusion and similarly the light spot visible to the right in the pit are likely to be due to an edge effect.

Before these specimen could be anodized the carbon coating, which was needed for the SEM examinations described in the previous section, had to be removed. As a result of this the cross sections shown here are a few micrometer deeper into the electrode as those presented in Fig. 4.18. This verifies that the crack visible to the right of the pit in Fig. 4.18 is in fact a part of the pit itself, as stated, because in Fig. 4.28b the pit emerges at the location where the crack could be seen before.

The metallographic images of cross sections of AC-, rectified AC- and DC-contact spot fractures presented in this section show that the electrode bulk distant from the contact spot is largely unaffected of any processes occurring in or in close vicinity of the contact spots. This behaviour is not only independent of the wave shape of the applied current, but also independent of the aluminium alloy used for manufacturing the electrodes as well as the degree of cold working respectively the tempering. However, it could also be seen that the conditions are considerably different when regarding the structure of the metal in immediate vicinity of a cross sectioned contact spot fracture. Small grains clustering around the fracture were detected when AC or rectified AC were applied. This could not be observed when examining the cross section of a DC contact spot fracture. The cluster of small grains appears to be embedded into the larger grains of the mainly unaffected bulk, extending approximately one contact spot radius a into the bulk, measured from the center of the contact spot fracture.

It is also observed that cracks not necessarily constitute a boundary for the cluster of small grains, but it usually does not extend much further beyond. Clusters of small grains are found with the contact spot fracture on both electrodes of a contact when the fracture had a generally low profile. In the case of a contact spot fracture with distinct pits and protrusions, as typically found with unstable contacts upon separation of the electrodes, the protrusion consists entirely of small grains whereas only a few grains could be seen with the pit on the opposite electrode.

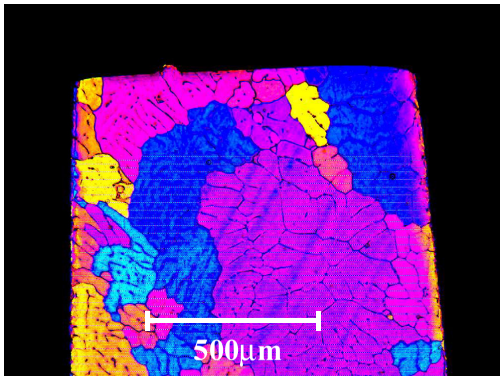

Figure 4.27a: Metallographic image of DC contact spot fracture cross section (anode). This contact carried 90 A DC for 10 days.

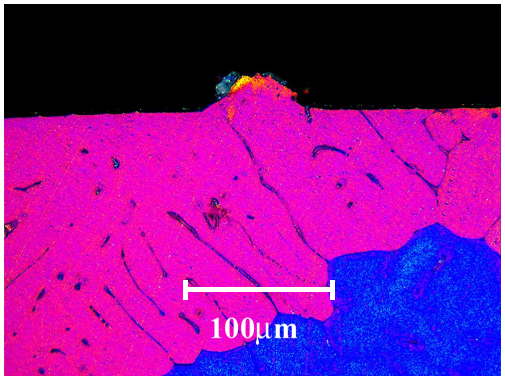

Figure 4.27b: Enlarged detail of the image shown in Fig 4.27a

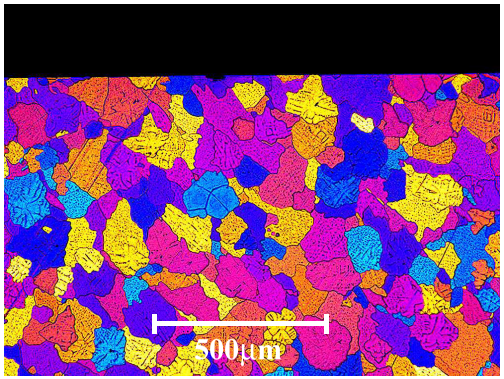

Figure 4.28a: Metallographic image of the cathode corresponding to the anode shown in Fig. 4.27a.

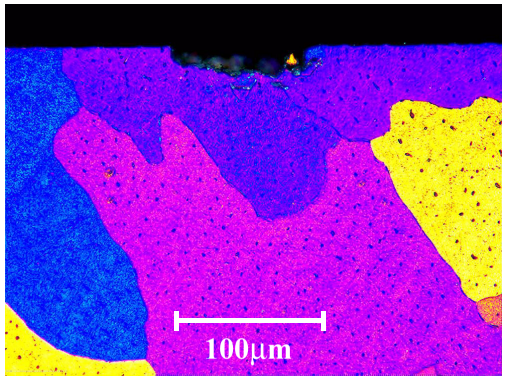

Figure 4.28b: Appearance of the cross sectioned pit as an enlarged detail from Fig. 4.28a.

4.6 Examination of tracer distribution in cross sectioned contact spots

This Section presents SEM-images of cross sectioned contact spot fractures, where 10% zinc was alloyed into one of the aluminium electrodes. All images were taken in backscatter electron detection mode, where zinc appears brighter than aluminium. Thus the zinc distribution in the electrode respectively the contact spot area could be examined. First some SEM backscatter images are shown followed by an EDA-examination of the zinc content of the cross sectioned specimen. Only experiments where AC and rectified AC was applied to the contact were conducted. No experiments with DC were carried out because extensive research on this has already been done by Runde [17].

The element contrast image of a cross sectioned AC contact spot fracture shown in Fig. 4.29 can be compared to the metallographic image Fig. 4.20 from the same contact presented in the previous Section. The aluminium electrode bulk appears dark grey against the lighter protrusions which contain zinc. The epoxy used for embedding the electrodes appears black. Immediately below both zinc-enriched protrusions it appears as if the zinc propagated along the grain boundaries approximately 20 µm into the bulk. Due to this the contours of some of the small grains as described in Section 4.5 become visible. The black dots found isolated within the bulk as well as within the protrusions are SiC grains from the polishing and grounding process. Disregard the white spot between the protrusions.

Fig. 4.30 shows the cross section of an AC contact spot fracture that carried 140 A AC for four hours. In this case the zinc-enriched AlZn10-electrode is shown. Against the white electrode bulk the protrusions appear darker because they contain less zinc. Some cracks can clearly be distinguished partly separating the protrusion from the electrode bulk. The cracks apparently constitute a barrier to the zinc because it can be observed that the zinc concentration changes abruptly across the crack. But also the transition in zinc concentration from the electrode bulk to the protrusion where there are no cracks is rather abrupt, no gradual depletion of zinc from the electrode bulk towards the protrusion can be seen.

The backscatter electron detector SEM-image presented in Fig. 4.31 shows a greater part of a cross sectioned electrode with one contact spot fracture. Here the aluminium electrode is seen. The contact carried 50 A AC for 25 days. The location of the cross sectioned contact spot fracture is the white area of approximately 80µm width on top of the electrode indicated by the arrow. The bright appearance of the contact spot fracture is due to its zinc content originating from the opposite electrode of the contact, which was made from AlZn10. As

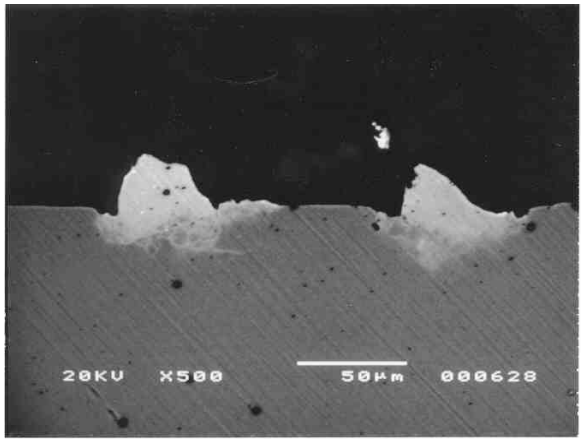

Figure 4.29: SEM-image using element contrast of a cross sectioned AC contact spot fracture. The protrusions contain zinc-tracer

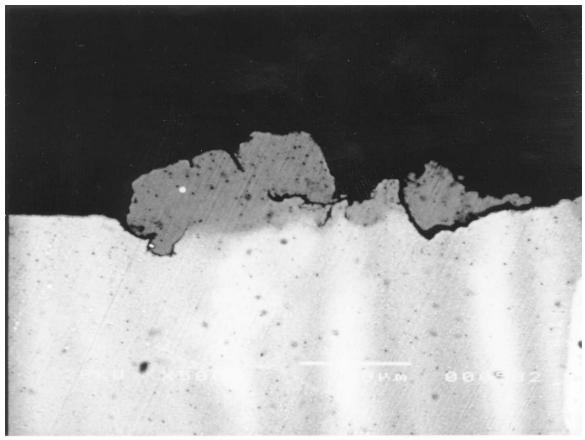

Figure 4.30: Cross section of an AC contact spot fracture on an AlZn10-electrode with protrusions of reduced zinc concentration

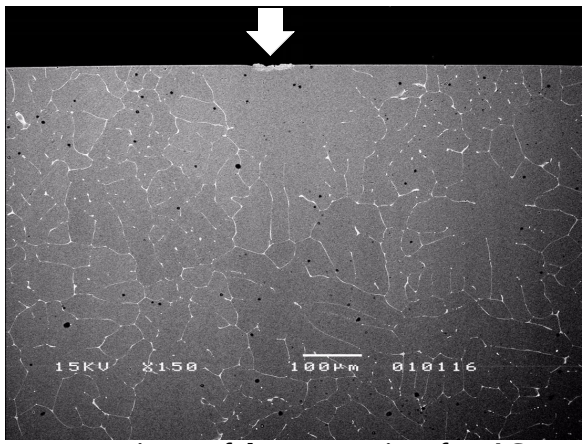

Figure 4.31: Element contrast image of the cross section of an AC contact spot fracture containing zinc (arrow)

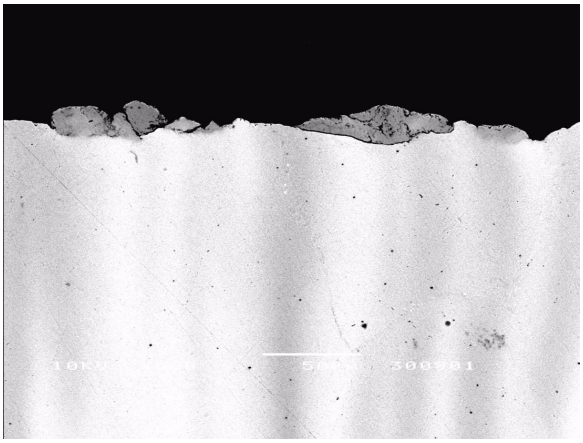

Figure 4.32a: Cross sectioned contact spot fracture which carried rectified AC (AlZn10-anode). The element contrast shows that the protrusions contain less zinc.

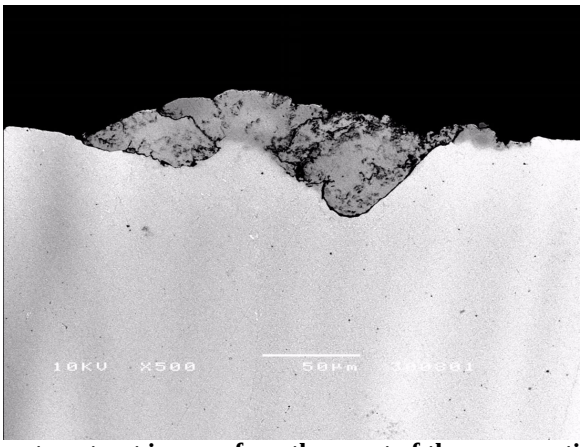

Figure 4.32b: Element contrast image of another part of the cross sectioned electrode shown in Fig. 4.32a

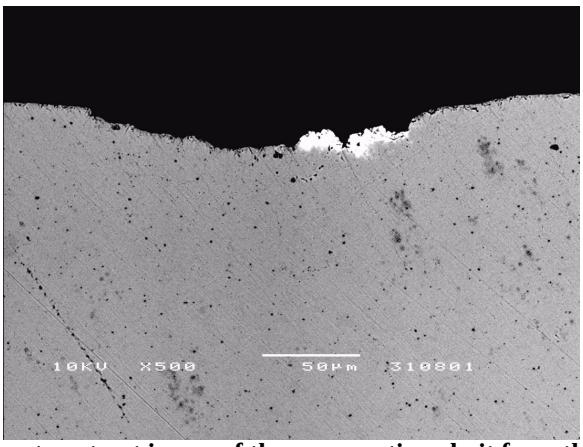

Figure 4.32c: Element contrast image of the cross sectioned pit from the cathode corresponding to the images shown above

observed in Fig. 4.31 the transition in zinc concentration from the contact spot fracture to the electrode bulk is rather abrupt. The white lines within the electrode are Fe-precipitates along the grain boundaries. From this it can be assumed, that the contact spot fracture is embedded within one single large grain of approximately 300 μm diameter. This is similar to what has been observed with the metallographic images in Section 4.5.

In Figs. 4.32a and b the anode and in Fig. 4.32c the cathode of a contact already examined earlier (cf. Fig. 4.10, Fig. 4.17 and Fig. 4.25) are seen in cross section in backscatter electron detection mode with the SEM. The characteristic protrusions on the AlZn10 anode can be seen to have lower zinc content than the electrode bulk. The cracks visible constitute clear boundaries between areas of relatively high and areas of relatively low zinc concentration. But also where there are no cracks the zinc concentration does not show any gradual transition from a relatively high to a relatively low concentration. As described with the AC contact spot fracture the change in concentration is abrupt. This is valid for both the anode as well as the cathode, as can be seen in Fig. 4.32 c, where a cross section of the pit in the cathode is shown. Small areas containing zinc in the pit appear white against the electrode bulk made of pure aluminium. The black dots all over the aluminium are SiC grains from the polishing process.

All the cross sectioned contact spot fractures from experiments where one of the electrodes was made from AlZn10 were carefully examined with the EDA. In order to determine the zinc distribution across the electrode the intensity of the AlKα- and the ZnKα-radiation were recorded in a number of points. Each of the points examined had a surface area of approximately 25 μm^2. The depth into the metal surface from which the radiation was detected depends in this case mainly on the acceleration voltage chosen for the electron beam. With the acceleration voltage set to 15 kV the depth becomes approximately 2 μm. The intensity of the ZnKα-radiation measured when scanning the surface area of each single point is proportional to the zinc concentration in the corresponding volume. The zinc concentration in the bulk of an AlZn10-electrode is known to be 10%. The intensity of the ZnKα-radiation measured in a point on the bulk of an AlZn10-electrode usually was twice the ZnKα-radiation-intensity recorded in a point located in a protrusion. Provided otherwise identical conditions, it can thus be concluded that the alloy in the protrusion is AlZn5. No significant changes in zinc concentration could be found when examining various locations in the protrusions or in the bulk.

The observations described above were independent of the wave-shape of the current applied to the contact as well as of the duration of the experiment.

Moreover it could be seen from the element contrast examinations of the cross sectioned Al-AlZn10-contacts that the cracks act as a barrier between areas of different zinc concentration.

4.7 Possible porosities in contact spot cross section

On some of the SEM images in Section 4.4 as well as on metallographic images in Section 4.5 dark areas, previously referred to as dark spots respectively shaded areas, could be seen close to the cross sectioned contact spot fracture and also within the protrusion (cf. Figs. 4.16 and 4.25). In the following the significance of these dark areas is evaluated in some detail.

The SEM-image shown in Fig. 4.33a is of the cross section of the contact spot fracture shown before in Fig. 4.14. The image was taken using the backscatter electron detector. The white lines and dots visible across the electrode are Al_3Fe-precipitates within the grains and along the grain boundaries. The profile of the contact spot fracture with pits and protrusions can be clearly distinguished. Apart from the cracks under the protrusions also shaded areas within the protrusion and black spots under the fracture are detected. It can be seen that the shaded areas and in particular the black spots are without exception only found in the HAZ at the contact spot.

In Fig. 4.33b the protrusion seen in Fig. 4.33a to the left of the cross sectioned fracture is shown in greater magnification. The image was taken using a CCD-camera connected to an optical microscope. The crack under the protrusion can clearly be seen as well as the shaded areas in the protrusion. These areas seem to consist of many small dots with an average diameter below 1 µm. The appearance of these small dots is as if they were porosities in the contact spot fracture. The larger black spots located under the fracture could be only faintly detected with optical examination. The thin stripes visible all over the metal in various directions come from the polishing process.

The protrusion shown in Fig. 4.33b can be seen as a SEM-image using secondary electron detection in Fig. 4.33c. The crack under the protrusion as well as the white Al_3Fe-lines and -dots can very well be seen. In addition to that the black spots located under the fracture and some polishing stripes can be detected. The black spots are equally distributed over the area immediately under the fracture. The shaded areas in the protrusion can hardly be seen. No additional black spots were found examining the electrode bulk using secondary electron detection mode with the SEM.

Fig. 4.33d is an element contrast image of the cross sectioned protrusion shown in Fig. 4.33c. Here, the crack, the shaded areas and the black spots under the fracture can be seen very well. As before also the white Al_3Fe-lines and -dots as well as the polishing stripes are visible. From this image the diameter of the black spots

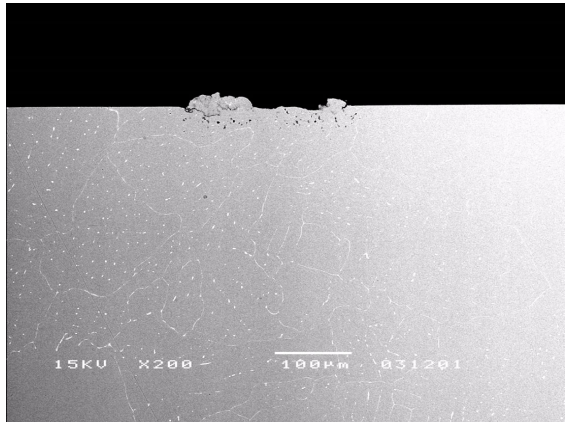

Figure 4.33a: Backscatter image of a cross sectioned contact spot fracture with cracks and dark areas

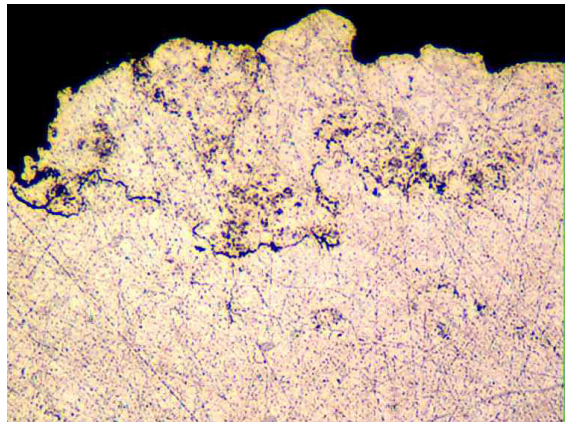

Figure 4.33b: optical CCD-image of the protrusion seen in Fig. 4.33a

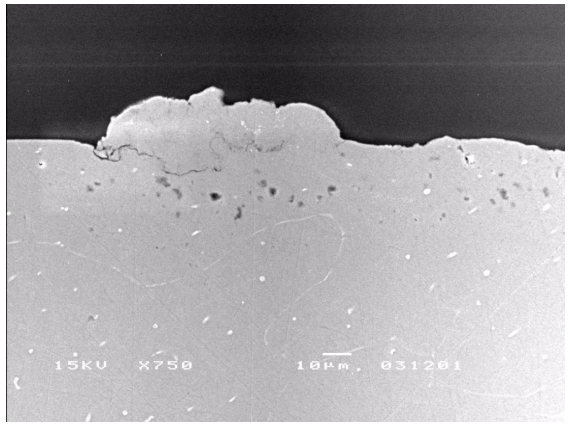

Figure 4.33c: Secondary electron image of the protrusion shown in Fig. 4.33a

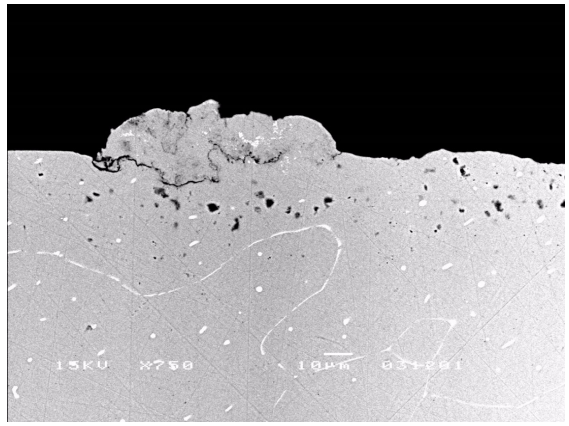

Figure 4.33d: Backscatter image showing the protrusion from Fig. 4.33a in greater magnification

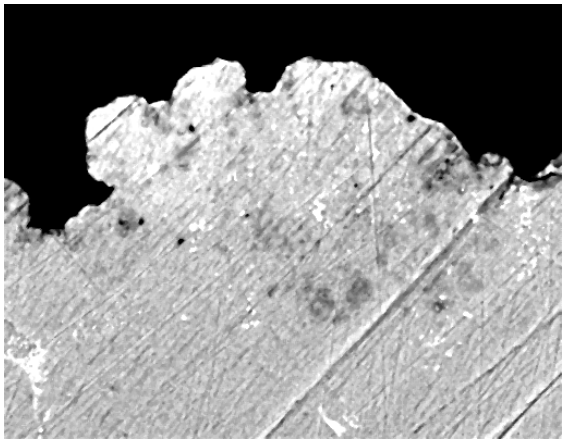

Figure 4.34a: Backscatter electron image of a cross sectioned contact spot fracture with shaded areas

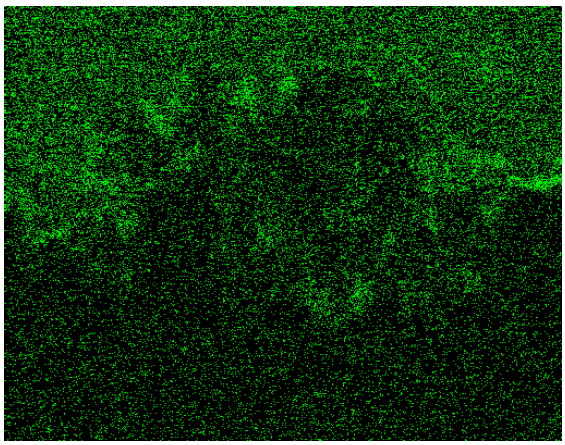

Figure 4.34b: Oxygen-mapping of the cross section shown in Fig. 4.34 a

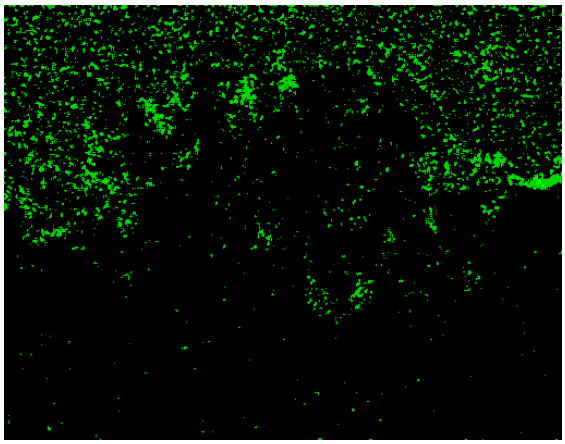

Figure 4.34c: Oxygen-mapping of the cross section shown in Fig. 4.34 a with low intensity areas filtered out

can be determined ranging from 1 µm to 5 µm approximately. The black spots can be characterized in their appearance as if they were pores in the electrode following the description given above for the shaded areas.

In Fig. 4.34a a SEM-image of another cross sectioned protrusion is shown. The corresponding contact spot fracture has been presented earlier in Fig. 4.5a. Shaded areas, polishing stripes and Al_3Fe-precipitates can clearly be distinguished in this element contrast image.

In Figs. 4.34b and 4.34c an EDA-mapping of oxygen which is found on the cross section surface is shown. The epoxy used for embedding the electrode has a high oxygen content which is represented in the image by a high density of bright dots. Against this the contour of the protrusion can be distinguished because the aluminium has less oxygen on the surface, which results in a lower dot-density. However, comparing Figs. 4.34a and 4.34b reveals that in particular those areas that appeared shaded in Fig. 4.34a show higher oxygen content than the surrounding aluminium-surface. This effect appears enhanced in Fig. 4.34c where the signal from areas of low oxygen content was filtered out. The contour of the protrusion can still be distinguished.

The dark areas described above were usually found with contacts where unstable electrical behaviour was observed during the experiment. Dark areas could be seen with contacts that carried AC as well as rectified AC. No black spots or shaded areas were found on cross sectioned DC contact spot fractures.

The dark areas only occurred close to the contact spot fracture and were observed independently of the aluminium alloy used for the electrodes. Hence these dark areas are probably connected to the ageing process in the contact spot and might be an indication of material degradation. Further discussion regarding the origin and nature of the dark areas is presented in Chapter 5.

4.8 Observation of irregularities of the contact resistance

Some of the contacts where unstable electrical behaviour as described in Section 4.2 was observed, had a contact resistance which was very much different from the contact resistance as it usually is observed with the voltage across the contact $u_c(t)$ and the current i(t) according to Fig. 4.1.

In Fig. 4.35 the voltage across the contact $u_c(t)$, the current i(t) and the contact resistance $R_c(t)$ from an experiment where the contact carried 100 A rectified AC are shown. The corresponding contact spot fracture can be seen in Fig. 4.10. The upper part of Fig. 4.35 is a hardcopy of the oscilloscope screen taken during the experiment. The rectified voltage $u_c(t)$ and current i(t) and the respective smoothed curves U_c and I can be seen over one half power cycle. The smoothed curves represent the data recorded by the data-logger as it is obtained from the PVM (cf. Fig. 3.5). The lower part of Fig. 4.35 shows a plot of the contact resistance as it is determined from the oscilloscope hardcopy above (plot I) compared to the contact resistance as it usually occurs in a contact when the shape of the voltage and current is as shown in Fig. 4.1 (cf. plot II). The data for the latter curve was determined from data recorded with the same experiment, before the contact became unstable. The variation of the contact resistance with temperature according to (2.20) can be observed in plot II.

The voltage $u_c(t)$ can be seen to rise steeper than usual, i.e. with approximately $\Delta u_c/\Delta t = 207$ V/s instead of $\Delta u_c/\Delta t = 107$ V/s, until it reaches 0.3 V, where the curve bends sharply and continues to rise with approximately $\Delta u_c/\Delta t = 36$ V/s. This is followed by a voltage peak of 0.447 V, whereupon the voltage suddenly drops to 0.4 V. From there on the voltage slopes to 0 within 4.5 ms. The corresponding contact resistance $R_c(t)$ is shown in the lower diagram of Fig. 4.35 (plot I).

Another set of curves is shown in Fig. 4.36. The plots were recorded with the AD-converter during an experiment, where 125 A AC was applied to a contact for 48 hours. In this case the irregularities of the contact resistance occur when the current approaches its peak value. This was recorded as what can be described as a protrusion on the positive as well as negative peaks of the voltage curve. All three plots shown have in common, that the irregularity appears nearly unchanged on several power cycles consecutively. Next to each of the plots the voltage $u_c(t)$ and the current i(t) of one half-cycle are shown in detail with the contact resistance $R_c(t)$ as it was determined from the recorded data.

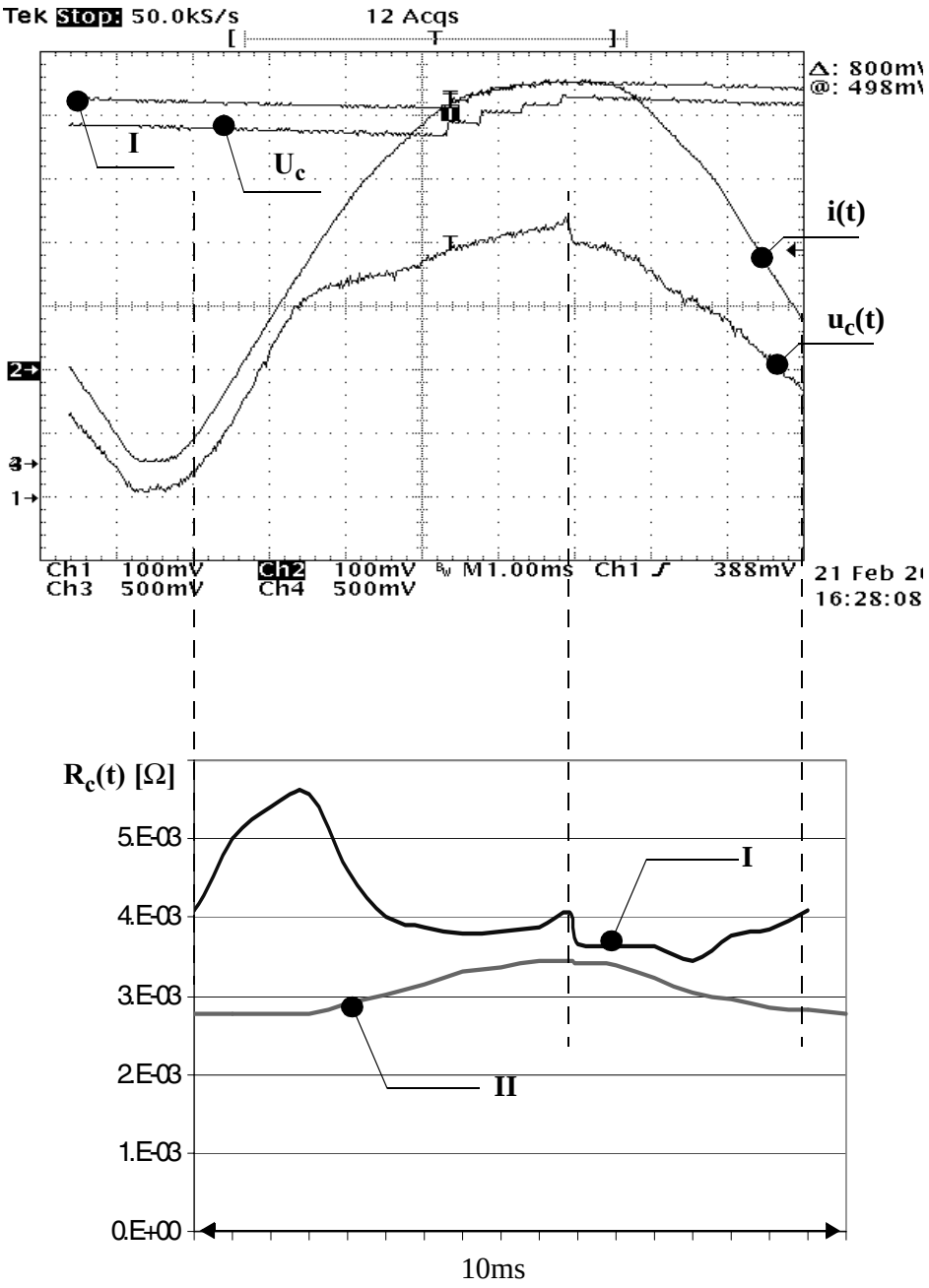

Figure 4.35: Voltage across the contact $u_c(t)$, current i(t) and contact resistance $R_c(t)$ during an experiment where rectified AC is applied to the contact. The upper graph is a hardcopy of the oscilloscope screen where the traces of $u_c(t)$, i(t), U_c and I can be seen. In the lower diagram the contact resistance $R_c(t)$ as determined from the recorded data seen above (plot I) and an additional curve showing the usual shape of $R_c(t)$ (plot II) are presented.

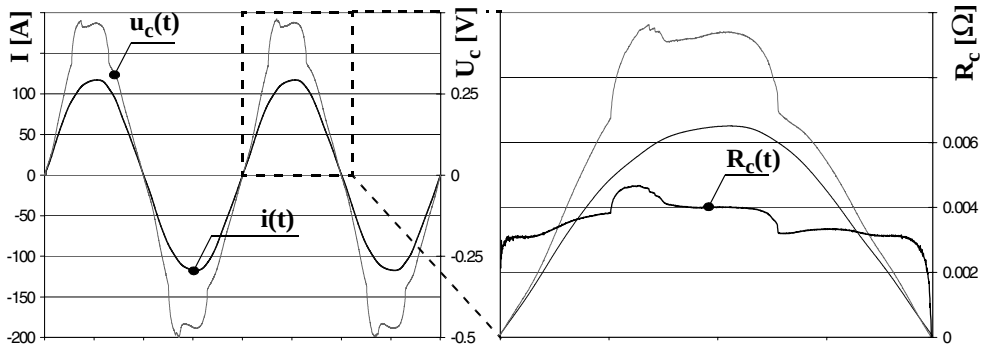

Figure 4.36a: Voltage across the contact $u_c(t)$ and i(t) recorded via AD-converter. One half cycle is shown in greater detail with the contact resistance R_c added in the diagram to the right. R_{cmax} = 4.6 mΩ.

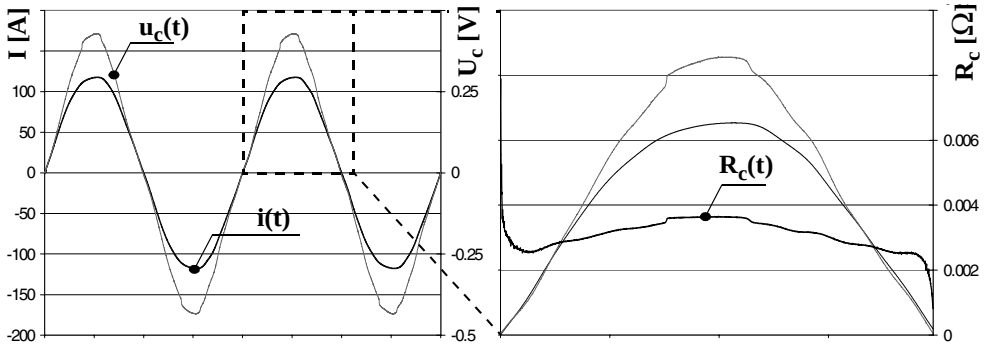

Figure 4.36b: Voltage across the contact $u_c(t)$ and i(t) recorded via AD-converter. One half cycle is shown in greater detail with the contact resistance R_c added in the diagram to the right. R_{cmax} = 3.64 mΩ

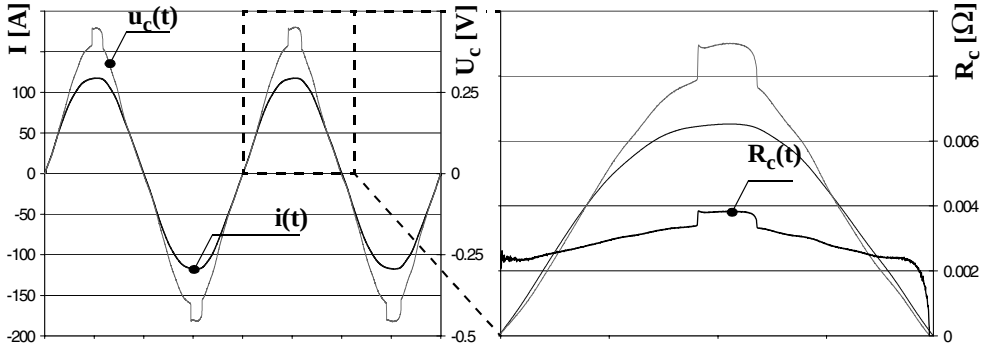

Figure 4.36c: Voltage across the contact $u_c(t)$ and i(t) recorded via AD-converter. One half cycle is shown in greater detail with the contact resistance R_c added in the diagram to the right. R_{cmax} = 3.84 mΩ

In the detailed plot in Fig. 4.36a it can be seen that the contact resistance R_c suddenly rises from R_c = 3.8 mΩ to R_c = 4.6 mΩ when the voltage reaches u_c = 0.343 V. Due to this the voltage rises with sinussoidally increasing current accordingly to u_c = 0.47 V. In a similar manner as the contact resistance suddenly rose it drops from R_c = 3.9 mΩ to R_c = 3.2 mΩ with the voltage at u_c = 0.343 V as before. From then on the contact resistance follows approximately the usually observed curve until the end of the half cycle.

The appearance of the curve of the contact resistance R_c as shown in Figs. 4.36b and c is essentially similar to the one presented in Fig. 4.36a. Initially following the usually observed curve the contact resistance changes abruptly to a higher value. In Fig. 4.36b the contact resistance jumps from R_c = 3.4 mΩ to R_c = 3.6 mΩ, synonymous to a step in the voltage from u_c = 0.390 V to u_c = 0.402 V. The contact resistance remains then fairly constant at R_c = 3.6 mΩ for approximately 1.8 ms. Then it drops back to R_c = 3.4 mΩ at u_c = 0.405 V sloping to R_c = 2.5 mΩ towards the end of the half cycle.

The curve for the contact resistance shown in Fig. 4.36c has an even more distinct discontinuity than the one shown above. It can be characterized by a rise in resistance from R_c = 3.4 mΩ to R_c = 3.8 mΩ and a corresponding voltage step from u_c = 0.397 V to u_c = 0.445 V. The contact resistance remains for approximately 1.3 ms at this elevated level. Then it drops back to R_c = 3.3 mΩ (u_c = 0.380 V) sloping to R_c = 2.3 mΩ towards the end of the half cycle.

This irregular electrical behaviour of the contact resistance was observed with AC- as well as with rectified AC-experiments. It could not be seen with DC-experiments. These irregularities of the contact resistance were exclusively observed with experiments where the contact can be characterized as unstable according to Section 4.2. The discontinuous electrical behaviour of the contact resistance could be seen occurring at several consecutive power cycles, each time having approximately the same appearance. The voltage across the contact $u_c(t)$ was at the start of the discontinuity of R_c observed to be of approximately the same magnitude at the end of the discontinuity of R_c.

5

Discussion

5.1 Introduction

The experiments where the procedure and the results have been described in detail in the previous chapters were done with the main purpose of documenting the deterioration of contact spots between aluminium contacts. Particular emphasis was put on the close examination of single contact spots that carried AC, focusing on thermo-mechanical effects occurring in the contact. These effects in turn are due to the current cycling. Experiments on single contact spots between aluminium conductors carried out by Runde [17] using a similar experimental setup and procedure showed electromigration being a current induced deterioration mechanism when applying DC to a contact. Other work on the deterioration of stationary electrical contacts due to thermo-mechanical effects and subsequent cracking has been done by Braunovic and Aleksandrov [37] on bimetallic Cu-Al-contacts, stating the embrittlement of the contact interface due to the formation of intermetallics at elevated temperatures being the cause for impaired mechanical and thus electrical integrity. Thermal stress cracking in electrical contacts has also been reported amongst others by Wingert [38] and Kang et al. [39], where the erosion of electrodes in switching contacts is described due to thermal shock in the case of arcing between the electrodes.

To the author's knowledge the development of cracks in the contact spots of stationary symmetric Al-Al-contacts caused by thermal fatigue has not been reported as a deterioration mechanism before.

5.2 Experimental method

The experimental arrangement as described in Section 3 is kept extremely simple. Basically the circuit is an ohmic conductor, whose stray inductances and capacitances are negligible, connected to the secondary winding of a transformer. The aluminium electrodes in their holders could easily be removed from the circuit. The electrodes remained upon separating in their respective holder during

the SEM surface examinations. For cross sectioning they were taken out of the holder, which then could be reused for a new contact.

The most important advantage of this contact configuration is that usually only one single contact spot is created. This contact spot occurs then at some arbitrary location on a comparatively large, polished surface. The fact that all the current applied to the contact passes through one single contact spot allows for detailed monitoring of the electrical stresses experienced in this particular contact area. Alternating current with a peak value of up to 140 A was applied. This current produces in the interface between aluminium electrodes with a 0.2 V voltage drop a contact spot with a diameter in the order of 50 µm. It is not complicated to cross section a contact spot of this size and study the profile of the contact spot as well as its metallographic appearance.

The unstable electrical behaviour of aluminium contacts with AC applied compared to DC-experiments which was reported in [17] could be verified when electrodes made from pure aluminium were used. However, the instabilities became fewer and the experiments more consistent when electrodes made from aluminium of greater hardness were used. Most experiments were carried out with electrodes of cold worked pure aluminium or of commercially pure AA1350.

Even if this experimental method proved very well suitable for studying single contact spots on polished electrodes under laboratory conditions, it has to be pointed out that practical contacts are rougher and form several contact spots upon mating. Hence, this very simple experimental setup is useful for fundamental studies of the physics of microscopic contact spots exposed to extreme and alternating current densities, but it is not suitable for evaluations of the properties of macroscopic contact devices.

5.3 Electrical behaviour

The electrical behaviour of the aluminium contacts as it is determined from the data recorded during the experiments is generally comparable to the behaviour observed with practical contacts. Except for that mostly single spot contacts were examined in the experiments, the main difference is that the voltage U_c is approximately one or two orders of magnitude lower in a good practical contact. The implications regarding this are discussed later on. The contact resistance can be seen to rise after having been constant for some time. This rise in resistance occurs completely unpredictable and is usually followed by a sudden decrease in

resistance. This process is repeated in irregular intervals. Williamson refers to this phenomenon as self-healing [40]. The rising contact resistance indicates ageing and gradual deterioration of the electrical conductivity in the contact spot region.

The contact resistance was determined from the current and voltage measurements as described earlier. While the LEM-shunt used for the current measurement yields an output signal of several volts and is thus less susceptible to disturbances coupled electromagnetically into the leads to the data-logger, this had to be verified for the measurements of the voltage across the contact. A continuous background noise of a few millivolt could be detected on the signal, probably due to aerial HF-radiation. No distortion in the signal could be connected to the current in the experimental circuit. The magnetic flux density caused by the current was determined to be approximately 100 μT at the voltage measuring leads. Therefore it was assumed that any voltage induced into the measuring leads due to the current in the experimental circuit could be neglected. In addition the melting voltage for pure-aluminium electrodes was verified to be 0.3 V. The melting voltage for other aluminium alloys used in the experiments was about the same: the effect of a slightly higher resistivity in the alloys is cancelled out by their lower melting point.

With unstable contacts that showed signs of severe ageing when regarding the contact spot fractures it was found that the voltage across the contact exceeded the melting voltage very often and remained at an elevated level above it. This particularly unusual behaviour was not observed with DC experiments. An example for this has been given in the voltage, current and temperature recording shown in Fig. 4.3. The corresponding contact spot fracture and its cross section were presented in Figs. 4.14 and 4.33 respectively. It is important to note, that no sign of melting is obvious from the appearance of the contact spot fracture. Furthermore it was shown in Chapter 2 that the voltage measured across the contact and the temperature in the contact spot are in phase and related to each other via the Kohlrausch equation (2.14) as if DC was applied, i.e. the voltage measured above the melting voltage is not due to a time-lag in the transient temperature response.

From the cracks visible it can safely be assumed that the current flow lines can not pass the constriction as shown in Fig. 2.2. Cracks underneath the contact spot will lead to additional constrictions in the current flow lines in this region and the model used in Chapter 2 does not apply in these experiments. While the resistivity in this region is expected to increase even further than the already elevated temperature in the contact spot suggests, the thermal conductivity does not necessarily decrease accordingly. Some of the heat generated in the constrictions

might be dissipated across the narrow cracks, i.e. not all the heat follows the current flow lines. This contradicts the basic requirement for the validity of the Kohlrausch equation, resulting in a temperature level in the contact spot below the one obtained when applying (2.14). Thus the voltage recordings above the melting voltage without any signs of melting visible in the contact spot fracture can be explained. The variations in the voltage across the contact observed in Fig. 4.3 are to a certain extent due to the dynamic nature of the deterioration process in the contact spot caused by unpredictable crack development. This makes it virtually impossible to describe the thermal behaviour more exact.

The gradual rising and sudden decrease of the contact resistance as a characteristic sign for contact deterioration as it has been mentioned in the beginning of this Section is documented in Fig. 4.4. Of particular interest is the voltage- and resistance peak that was recorded immediately before the voltage drop. Assuming that the melting temperature is reached in the constriction immediately before the peak, this causes the resistivity of the molten aluminium to increase by a factor of 2.46 [41]. The voltage across the contact rises accordingly to its peak value of 0.444 V and drops thereafter to 0.339 V. The voltage drop can be explained by a self-healing process occurring in the contact spot. Cracks present in the contact spot region can intensify this process by at first accelerating the temperature rise in the constriction because thermal conductivity is reduced in the contact spot region. The power dissipated in the constriction cannot be conducted away into the cooler electrode bulk across the cracks as good as if there were no cracks. Then, when the melting temperature is reached in the constriction, the contact resistance is reduced not only because the contact spot widens with the molten metal spreading, but it can also be assumed that molten metal partly infiltrates the cracks in the contact spot region and thus reduces the electrical resistance and increases thermal conductivity simultaneously. Similar behaviour has been observed earlier by Wingert [38].

The discontinuities in the contact resistance documented in the diagrams shown in Section 4.8 are due to the abrupt increase in resistivity of aluminium in the contact spot when its temperature reaches the melting point. The effect of reduction of contact resistance can be observed twice in Fig. 4.35. The only reduction of contact resistance detected in the diagrams in Fig. 4.36 is due to the increase in conductivity of aluminium upon solidification. In spite of the contact spot temperature reaching the melting point repeatedly in each half-cycle over a time span lasting several seconds no immediate widening of the contact spot can be deduced.

The contact in the experiment, where the voltage and current recordings of one half cycle are presented in Fig. 4.35, is apparently already of unusual high resistance right from the beginning of the power cycle shown. When the melting voltage of $U_C = 0.3$ V is reached the resistance is effectively reduced in accordance with the process described above. However this reduction is not sufficient to avoid the voltage to increase further above the melting voltage with rising current. This then results in a resistance-peak followed by an immediate drop similar to the one shown in Fig. 4.4.

Another approach explaining this behaviour is by comparing these curves to those published by Mau [42] for copper contacts exposed to short circuit current as they are presented below in Fig. 5.9. Then the first change in resistance observed at $U_C = 0.3$ V would be due to the fact that the softening temperature of aluminium ($T_S = 150\ ^{O}C$, $U_{CS} = 0.1$ V) is reached in the constriction, similarly causing a reduction of the resistance by widening of the contact spot. The second change in resistance as observed would then be associated with the melting point being reached in the contact spot. However, softening happening at the melting voltage $U_C = 0.3$ V would then have to be considered coincidental.

Thus it appears that the processes occurring in aluminium contact spots subjected to AC that are causing its gradual deterioration involve a complex interaction of a number of events in very short sequence.

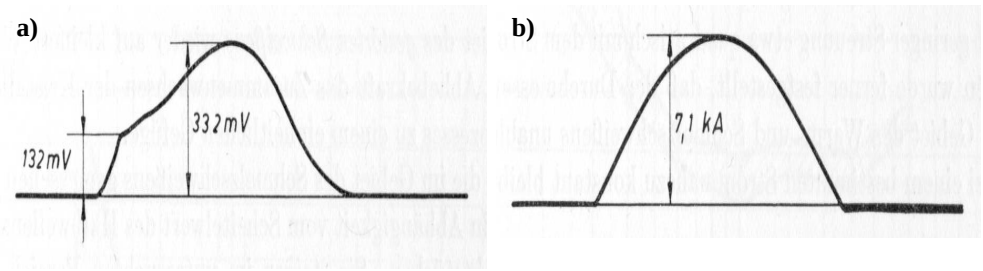

Figure 5.9: Voltage across a contact from copper-electrodes (a) and corresponding current (b) taken from Mau [42]. The softening voltage of copper is reported to be $U_{CS} = 0.120$ V [4], here softening is observed at $U_{CS} = 0.132$ V

5.4 The aluminium-aluminium contact interface

When separating the electrodes the contact spots are ruptured leaving a characteristic fracture on the polished contact surface. These contact spot fractures were then examined by SEM. In the following the various observations regarding the appearance of the contact spot fracture are discussed.

The typical appearance of an AC contact spot fracture as it was shown in Section 4.3 is an area several tens of micrometers in diameter having a pattern of protrusions and pits distributed across it. A corresponding pattern is always found on the opposite electrode. When comparing AC contact spot fractures with DC contact spot fractures it can be seen that the appearance of the fracture surface regarding details in its texture is similar whilst the profile of the respective fracture is very different. The fracture of a DC contact spot is always along weakened areas within the cathode. The deterioration mechanism behind this has been identified as elecromigration [17]. The similar texture of the fracture surface of AC- and DC-contact spots leads to the assumption, that the AC contact spot fracture is along weakened areas within the electrodes as well.

Similarly to DC contact spots these weakened areas in the contact spot region of AC contact spots are likely to locally reduce the electrical conductivity. This explains the comparatively large contact spot fractures with contacts that showed signs of severe ageing during the experiment: Once the electrical conductivity of the original contact spot decreases, its conductive surface increases according to (2.4) in combination with self-healing processes. It can be assumed that this enables the current to take a new undisturbed path of lower resistance in immediate vicinity to the original contact spot. As soon as the electrical conductivity of the new path decreases again this process is repeated and thus the contact spot becomes larger. This contact spot expansion apparently occurs often along tracks as it can be seen in the images presented in Section 4.3. It is important to note, though, that most likely only a small part of this enlarged contact spot contributes to the conduction of the current at a time.

The expansion of a contact spot during an experiment due to ageing as described above can be seen when comparing the contact spot fractures presented in Figs. 4.12 and 4.13. The contact shown in Fig. 4.12 carried 125 A AC for one minute, the contact shown in Fig. 4.13 carried 125 A AC for four hours under otherwise identical experimental conditions. Following the theory presented in Chapter 2, in particular using (2.4) and (2.22) with the data recorded during the respective experiment, the theoretically expected size of each of the contact spots A_t, as it would appear if no ageing mechanisms had reduced the conductivity in

the contact spot, can be related to the size of the fracture A_e. The higher the A_e/A_t-ratio the more the contact spot is deteriorated. The results of this comparison are presented in the table below:

Table 5.1: Comparison of contact spot fracture sizes

contact spot	I [A]	$R_{c\Theta}$ [mΩ]	duration	$\frac{R_{c0}}{R_{c\Theta}}$	a [µm]	A_e [µm^2]	A_t [µm^2]	$\frac{A_e}{A_t}$
Fig. (4.12)	125	1.8	1 min.	0.45	20.0	3421	1256	2.7
Fig. (4.13)	125	1.5	4 hours	0.5	23.3	25454	1705	14.9

As expected, the theoretical size of the contact spot A_t can be seen to be about the same in both contacts. The A_e/A_t-ratio represents the degree of enlargement of the contact spot due to ageing. Only little ageing can be determined in the first contact whilst the latter contact spot grew to nearly 15 times its original size in four hours. The example given above represents the general appearance of AC contact spot fractures as they were obtained according to the experimental procedure described in Chapter 3: considerable enlargement of the fracture was often observed already after only a few hours.

Thin flakes of aluminium bordering the contact spot fracture are clear signs of melting in the contact spot. The molten metal was squeezed from the contact spot into the narrow space between the electrodes where it subsequently solidified shaped as a flake. The solidified aluminium did not necessarily contribute to the conduction of current as it may have been separated from the electrodes by the insulating oxide-layer covering them. Often no signs of melting were found with the contact spot fracture even when the voltage measured across the contact exceeded the melting voltage. A possible explanation for this was given in Section 5.3.

The contact spot fractures from experiments where rectified AC was applied to the contact appeared to have both AC- as well as DC-characteristics at the same time. The fractures had large A_e/A_t-ratios as described above and generally had a protrusion on the anode with corresponding pit on the cathode. The electrical behaviour was less stable as found with DC contacts. In addition, small ridges bordering the contact spot fracture were found with contacts that carried AC as

well as rectified AC. The ridges appear as if the metal underneath has been compressed and bulged out due to repeated plastic deformation.

The outcome from the comparison between AC- and DC-contact spots is that electromigration is not the dominating mechanism in the deterioration of AC contact spots. The ageing probably owes to a mechanism connected to the repeated rising and decreasing of the current and thus also temperature. The existence of ridges bordering the contact spot fractures, the accelerated ageing of AC-contacts as well as the deterioration of a contact spot in such a way that the voltage across it can exceed the melting voltage all point towards a deterioration mechanism related to thermo-mechanical processes in the contact spot rather than electromigration. The experiments using rectified AC revealed that the current reversal is not a crucial factor. This assumption is supported by results from experiments with rectified AC applied to electrodes machined from pure aluminium. Here the deterioration mechanism connected to the pulsating current apparently was dominating yielding contact spot fractures similar to those found in ordinary AC experiments.

The hypothesis that the deterioration mechanism behind this is thermal fatigue due to the temperature cycling as a consequence of the AC applied to the contacts will be discussed in detail in the next Section.

5.5 Thermal fatigue in the contact spot region

Any metal specimen subjected to a repetitive mechanical stress will fail at a stress below its ultimate tensile strength after a certain number of loading-cycles. This kind of failure occurring under conditions of dynamic loading is referred to as fatigue failure, respectively, when occurring after the repeated application of thermal stress, thermal fatigue. Characteristic for (thermal) fatigue is the formation of minute cracks usually initiated at surface discontinuities and gradually spreading over the cross section of the specimen. Fatigue failure is caused by a critical localized tensile stress which is very difficult to evaluate. Because of this any relationship of stress applied over time to a criterion indicating actual failure of the specimen is largely based on empirical data. In addition to this the term failure in this context conventionally designates mechanical failure. The ability of the specimen subjected to repetitive stress to carry electrical current is not an integral part of this concept: small cracks may decrease the electrical conductivity considerably while they pose no imminent threat to mechanical reliability.

The cracks that could be observed underneath the contact spot fracture when examining cross sectioned electrodes are most likely a result of thermal fatigue in the contact spot region. The temperature cycling with AC applied to the contact causes stresses due thermal expansion and contraction of the HAZ. The simplified one-dimensional model of an expanding HAZ beneath the contact spot introduced in Chapter 2 can only serve as an approximation when analyzing the thermal stresses induced. But it incorporates several essential aspects of thermal fatigue damage in a contact spot:

- the cracks are localized beneath the bordering rim of the contact spot,

- the cracks propagate perpendicular to the direction of the applied stress,

- the volume undergoing appreciable thermal cycling is comparatively confined.

The contact spot fractures shown in Figs. 4.12 and 4.13 will be taken as an example in order to estimate the thermal stresses present in the respective contact spot region. Some of the experimental data has already been presented in Table 5.1. From this the temperature in the contact spot can be calculated according to (2.18) as $T_\Theta = 353\ ^oC$, setting $T_0 = 80\ ^oC$. The linear thermal expansion corresponding to this temperature is then determined using (2.41) to $\Delta l = 0.311\ \mu m$ with the coefficient of linear thermal expansion $\gamma_l(600^oC) = 28.5 \cdot 10^{-6}\ K^{-1}$. This yields a true strain of $\varepsilon = 0.0077$. The thermally

induced strain is above the yield point at $\varepsilon = 0.002$, so (2.42) can not be used here. Instead the exponential representation of the stress-strain-curve in the plastic domain is employed:

$$\sigma = K\varepsilon^n \tag{5.1}$$

with material parameter K = 180 MPa and strain hardening coefficient n = 0.3 [35] the stress corresponding to the strain determined above is $\sigma = 42$ MPa being well above the yield strength of $\sigma_y = 28$ MPa.

Already from this it can be seen that a considerable amount of plastic deformation would be expected in the contact spot region with every cycle due to thermal expansion and contraction. Considering that the yield strength σ_y decreases with increasing temperature, strain-rate and number of loading-cycles the effects of repetitive thermal stresses are intensified further. In addition to that the probability of cracks occurring is increased with the amplitude of the thermal stress because the critical resolved shear stress defining the beginning of plastic deformation in a single aluminium crystal is about $\tau_{crss} = 0.79$ MPa [30]. Taking the Schmid-factor for fcc-crystals as SF = 0.322 [30] this corresponds to a (thermal) stress of $\sigma = 2.4$ MPa, being well below the amplitude of the thermal stress determined above, and thus enhancing the tendency of the material to crack.

The number of load cycles to cracking under the above described conditions can be estimated using an approach presented by Johnson [43]:

$$\sigma_{max}\Delta\varepsilon = \frac{2\sigma'^2_f(2N_f)^{2b}}{E} + 2\sigma'_f\varepsilon'_f(2N_f)^{(b+c)} \tag{5.2}$$

with the parameter values above taken from [33] and [44]

stress amplitude	$\sigma_{max} = 42$ MPa
strain range	$\Delta\varepsilon = 0.0077$
fatigue strength coefficient	$s'_f = 95$ MPa
fatigue ductility coefficient	$e'_f = 0.022$
fatigue strength exponent	$b = -0.088$
fatigue ductility exponent	$c = -0.328$
Young's modulus	$E = 35$ MPa ($T = 350\ ^oC$)
cycles to mechanical failure	N_f

Using (5.2) the number of cycles to mechanical failure is determined to $N_f \approx 1000$ corresponding to approximately 10 seconds of AC application to the contact at this voltage drop. In this context it is important to note that the thermal stresses determined above and the number of cycles to failure predicted from this are approximate results. This owes to the fact that the exact values of the stress amplitude σ_{max} and the strain range $\Delta\varepsilon$ present in the contact spot under temperature cycling are not known. When assuming the strain range to be half of what was determined above, this would result in a 20-fold increase of the number of cycles to failure N_f, respectively approximately 3 minutes of AC application.

Moreover mechanical failure occurring in the contact spot does not necessarily cause electrical failure of the contact. Mechanical damage and microcracks can assumed to be present underneath the contact spot already before the critical number of cycles N_f is reached. As stated above this is likely to increase the electrical resistivity of the contact spot. This again will accelerate the mechanical deterioration process due to the subsequent rising of the temperature in the contact spot. But this will not interrupt the current flow: the current is going to take a new path of lower resistance close to the deteriorated, high resistance contact spot region. This is most likely the process behind the enlargement of contact spots as discussed in the previous Section.

The contact spot shown in Fig. 4.12a carried 125 A AC for 1 minute which corresponds to N = 6000 thermal cycles. Considering the inaccuracy of the prediction method used this is well within the limits where only little mechanical damage in the contact spot region is expected. This is also represented in the low A_e/A_t-ratio for this contact spot (cf. Table 5.1). The SEM-image of the cross section of this contact spot fracture in Fig. 5.2a shows no cracks and a low fracture-profile as it is typical for contact spots that carried current for only a short time. The contact spot shown in Fig. 4.13 on the other hand carried 125 A AC for 4 hours which corresponds to $N = 1.41 \cdot 10^6$ cycles. This exceeds the critical number of cycles N_f by far and a comparatively high degree of mechanical damage is expected in the contact spot, which is represented in its rather high A_e/A_t-ratio. The cross section of this contact spot fracture is presented in Fig. 5.2b and shows clear signs of cracking as well as a pronounced protrusion as it is usually found with electrically unstable contacts.

It can be assumed that when separating the electrodes, the contact spot ruptures along weakened areas, leaving the characteristic profile on the electrode surface behind. In the case of contact spots that did not experience severe ageing this rupture occurs close to the electrode surface as it would happen with resistance spot welds of low quality. On the other hand, contact spots that experienced severe

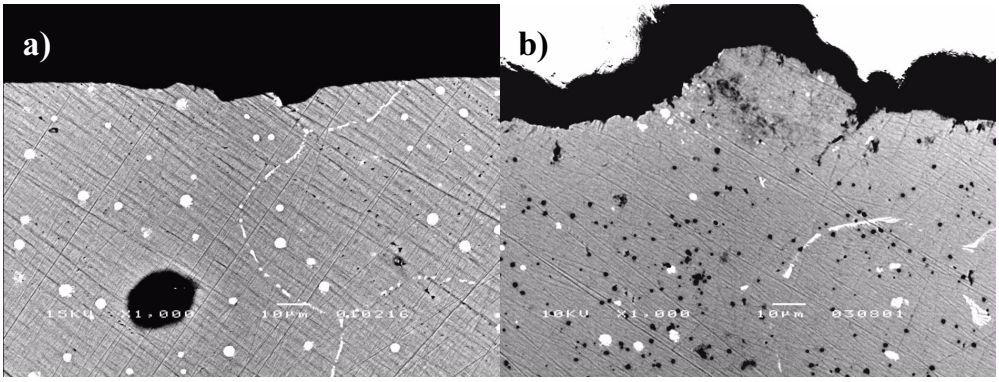

Figure 5.2a: Backscatter SEM-image of the cross section of the contact spot fracture shown in Fig. 4.12 with low fracture profile

Figure 5.2b: Backscatter SEM-image of the cross section of the contact spot fracture shown in Fig. 4.13 with pronounced protrusion and cracks

ageing due to temperature cycling with subsequent cracking will most likely rupture along these cracks upon separation. Since the cracks extend perpendicularly to the direction of the thermal stresses, this results in distinct protrusions and corresponding pits on both electrodes at the fracture.

Furthermore the ridges observed on the polished electrode surface close to the contact spot fracture might also be caused by repetitive thermal stresses in the contact spot. The pressure due to thermal expansion generated in the contact spot region forces the metal to bulge out, facilitated by the possibility of the temperature in close vicinity to the contact spot being above the softening temperature of aluminium T_S = 150 ^oC. It can be imagined that two ridges on opposite electrodes touch and thus, provided the oxide-film covering them is broken, form an electrically conductive metal-bridge between the electrodes. This process would then contribute to the enlargement of ageing contact spots.

Another aspect of thermal fatigue in contact spots is documented by the metallographic images presented in Section 4.5. Many small grains were observed in the HAZ of the contact spot surrounded by large grains in the electrode bulk. The small grains are supposed to have appeared as a result of a recrystallisation process under repeated thermal stress as it has been outlined in Section 2.2. The abrupt change in grain size at the transition from HAZ to electrode bulk is probably due to the steep temperature gradient and subsequent decrease of thermal stresses further into the electrode. Both, the recrystallisation of many small grains and the abrupt change of grain size increase the probability of cracking. Similar observations of a zone of recrystallised small grains under the contact spot on

copper electrodes are reported by Heiner in [45], with the difference that the stationary copper contacts examined carried the current only for one half power cycle.

Neither cracks, nor ridges, nor recrystallisation have been observed with DC contact spots where no temperature cycling occurs. This further supports the hypothesis of thermal fatigue due to temperature cycling being the dominating deterioration mechanism in the AC contact spots from the experiments discussed here.

The backscatter images of cross sectioned contact spot fractures with contacts where one electrode contained zinc clearly show that cracks effectively constitute a barrier for zinc migration. From this it can be assumed that the cracks appeared during the experiment and are not a result of tensile forces occurring in the contact spot region when separating the electrodes. However, it can be imagined that the existing cracks become enlarged under separation. The tracer distribution would be expected to be less uniform on both sides of the crack if it had occurred under separation (cf. Figs. 4.30 and 4.32). Signs of zinc had to be found in the bulk of the pure aluminium electrode also across the crack, as it can be seen in the cross section shown in Fig. 4.29, where zinc migrated along the grain boundaries into the electrode bulk. Grain boundary diffusion is possible even at temperatures too low for appreciable volume diffusion through the grains [31].

The dark spots respectively apparent porosities described in Section 4.8 are only found in cross sectioned AC contact spots, not in cross sectioned DC contact spots. Their existence also points to some physical change occurring in the contact spot region, which might very well be related to thermal fatigue. In particular because the porosities were found exclusively with severely aged and electrically unstable contacts. The pores (larger dark spots) and the porosities (dark dots, micropores) could both be detected on backscatter SEM-images. The porosities could hardly be seen with secondary electron SEM-images, whilst the pores were nearly invisible when optically examining the cross sectioned contact spot. This suggests that pores and porosities are of different nature. The oxygen-mapping of the cross sectioned surface revealed that the porosities have a higher oxygen content than the surrounding aluminium.

Several possible explanations may be found for the existence of pores and porosities close to the contact spot fracture. Pores due to gas inclusions, with aluminium in particular hydrogen, are a well known phenomenon from welding, but can usually be detected fairly easy optically or by SEM in a cross sectioned weld [46]. However, the comparison to welding presupposes melting in the

contact spot, which, as outlined before, can not always be expected. On the other hand, partial melting of the Al_3Fe-precipitates located on the grain boundaries might occur due to their melting point below that of pure aluminium; without leaving visible signs of melting on the contact spot fracture. The solidifying Al_3Fe contracts, leaving microvoids behind. Since there are many small grains in the contact spot also a great number of microvoids located on the grain-boundaries are expected. But again, this approach does not explain that the porosities are difficult to detect using secondary electron imaging. Another attempt of interpreting the observed pores includes the coalescence of microvoids prior to thermal fatigue cracking [44] possibly in combination with polishing agents being deposited there during polishing.

None of the above can be taken as a qualified explanation regarding the origin and the nature of the apparent pores or porosities. This is mostly due to the ambiguous and mutually contradicting observations. But, since nothing comparable was noticed with DC contact spots, it can be assumed that this phenomenon is related to repetitive thermal stresses in the contact spot as well.

5.6 Summary

Some concluding remarks regarding the relevance of the experiments and findings discussed above will be given in the following: Stationary aluminium contacts are usually designed in a way that upon mating not only one single contact spot but possibly hundreds are made. To a large extent this is due to the by far higher degree of surface roughness of practical aluminium electrodes. As shown in Chapter 2 this then results in a lower contact resistance subsequently meaning a lower contact voltage. In fact, the contact voltage across practical aluminium contacts is about one or two orders of magnitude below the voltage recorded during the experiments described in the previous chapters. This in turn implies a much lower peak temperature in each of the contact spots. Furthermore, the diameter of each of the many contact spots formed on the interface of practical contacts is assumed to be one or two orders of magnitude smaller than the diameter of the single contact spots examined in this work. As it could be seen in Chapter 4 contact spots carrying lower current are less prone to grow over time due to ageing (cf. Figs. 4.12 and 4.13). Hence considerably less thermal stresses are expected in contact spots in practical contacts. From this it may be assumed that thermal fatigue as a deterioration mechanism in practical stationary aluminium contacts is of lower significance when compared to other deterioration mechanisms as for example oxidation or fretting. However, comparing the

electrical behaviour of practical stationary contacts with the recordings of the contact voltage shown in Section 4.2, it may very well be assumed that thermal fatigue contributes to the accelerated ageing as it is often observed later in the life of stationary contacts and that this process is likely to be inititated immediately with current being passed through the contact.

6

Conclusion

The present work deals with ageing mechanisms in stationary aluminium contacts carrying AC. The main conclusions that can be drawn from the experimental and theoretical work in this study are as follows:

- The location, size and shape of a contact spot on the polished surface of an aluminium electrode can be found by examining the appearance of its characteristic fracture.

- The characteristic fracture of AC contact spots is different from the one of DC contact spots.

- The temperature in an AC contact spot cycles with the power dissipated in it, causing cyclic thermal stresses to occur in the contact spot region.

- The repetitive thermal stresses may eventually cause thermal fatigue cracking in the contact spot region, mechanically weakening this region.

- Upon separation of the carefully mated electrodes the contact spot fractures along the cracks inside the electrodes. If no cracks are present in the electrodes the contact spot fractures close to the electrode surface.

- The cracks lead to a reduction of the electrical conductivity in the contact spot region. The contact resistance is maintained by increasing the size of the contact spot.

- Plastic deformations of the contact surface in immediate vicinity of the contact spot indicate the existence of considerable repetitive mechanical stresses occurring in the contact spot.

- SEM-images of the cross sectioned contact spot fractures facilitate the verification of thermal fatigue occurring in the contact spot region.

- Metallographic images of the cross sectioned contact spot fractures support the theory of thermal fatigue being a deterioration mechanism.

- The use of zinc as a tracer metal in some of the experiments further confirms the theory of thermal fatigue when examining its distribution in a cross sectioned contact spot fracture.

- Thermal fatigue is shown to be a deterioration mechanism with stationary electrical aluminium contacts under the laboratory conditions of the present investigation.

- Regarding practical stationary contacts thermal fatigue is expected to contribute to the accelerated ageing process observed later in the life of a stationary contact.

Appendix

I

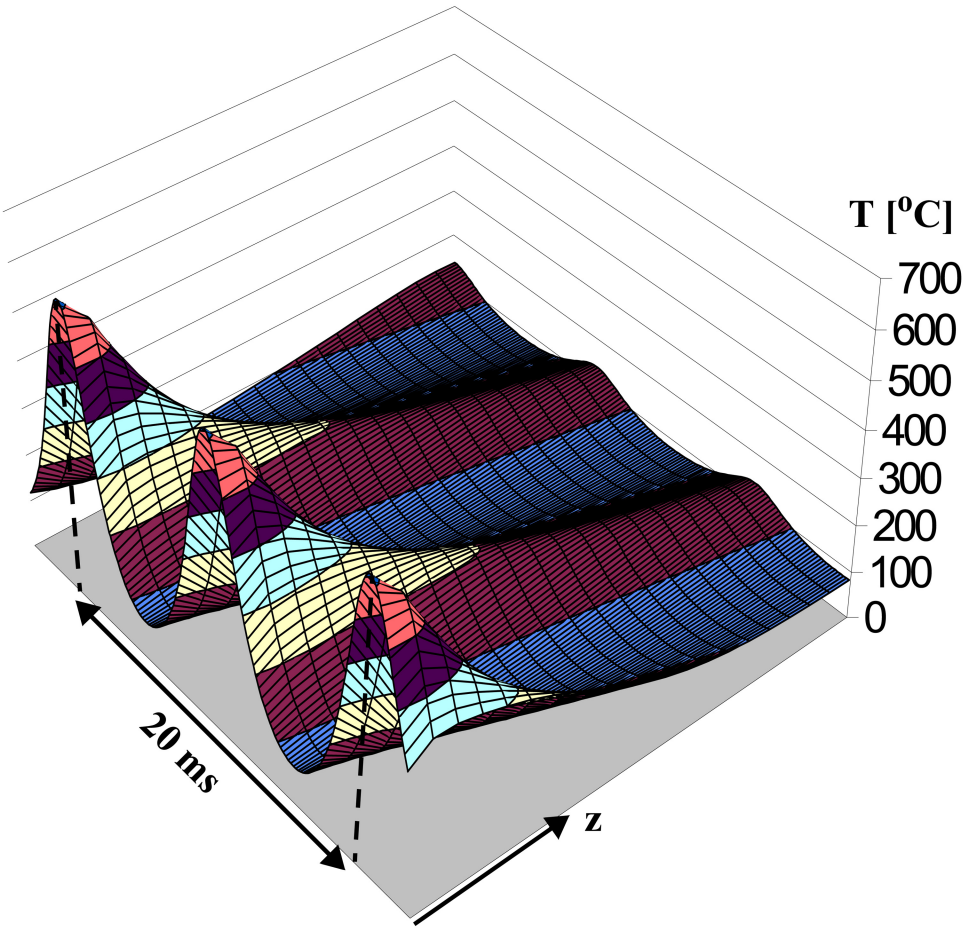

Qualitative representation of T(t,z) with phase shift into the electrode (cf. Figs. 2.13 and 2.14)

II

Material properties of pure (Al 99.99) and commercially pure (AA1350) aluminium taken from [47] if not otherwise indicated

Material properties of aluminium (pure and AA1350)

		Al 99.99	AA1350	
Density	ρ	2.6989	2.705	g/cm^3
Softening temperature [22]	T_S	150	150	^oC
Softening voltage [22]	U_S	0.1	0.1	V
Melting point	T_M	660.4	657	^oC
Melting voltage calc. meas [4]	U_m	0.302 0.3	0.281 0.3	V V
thermal conductivity	λ	247	234	$Wm^{-1}K^{-1}$
Coefficient of thermal expansion (20 to 300 ^oC)	γ_l	25.5	25.5	$\mu mm^{-1}K^{-1}$
Modulus of elasticity	E	62	69	GPa
Tensile strength	σ_m	40 ... 100	83 ...97	MPa
Yield strength	σ_y	20 ... 60	28 ... 83	MPa
Hardness (meas.)	H	30.5	37.7	HV
Resistivity	ρ	26.5	28.2	nΩm
Temperature coefficient of resistivity	α	0.0043	0.0035	K^{-1}

References

[1] C. Ruppert, M. Runde, “Ageing of aluminium contact spots - comparison between alternating and direct current”, Proc. 20th Int. Conf. on Electrical Contacts ICEC, 2000, Stockholm

[2] R. Holm, Electric Contacts, Berlin/Heidelberg/New York, Springer, 1967

[3] J. B. P. Williamson, “The microworld of the contact spot”, in Proc. Holm Conf. Electrical Contacts, Chicago: Ill. Inst. of Technol. , 1981, pp1 - 10

[4] R. S. Timsit, “Electric Contact Resistance: Fundamental Principles” , Chapter 1 in IEEE Publication "Electric Contacts: Principles and Applications", 1999

[5] M. Nakamura, “Computer Simulation for the Constriction Resistance Depending on the Form of Conducting Spots”, IEEE Transactions CPMT - Part A, Vol. 18, No.2 June 1995

[6] H. Kongsjorden, “Electric Contacts between Aluminum Conductors”, Dr.-ing. thesis, Trondheim, Norway, Norw. Inst. of Technol. 1977

[7] R. Holm, “Über Metallische Kontaktwiderstände”, Wiss. Veroff. Siemens-Werk Bd. 7/2 , 1929

[8] L. Fechant, “Echauffement des Strictions de Contact”, Chapter 3 in SEE publication “Le Contact Electrique”, Hermes, Paris, 1996

[9] J. A. Greenwood and J. B. P. Williamson, “Electrical Conduction in Solids, II - Theory of Temperature-Dependant Conductors”, Proc. Roy. Soc. , Vol. A246, pp 13 - 31, 1958

[10] E. v. Rziha, “Starkstromtechnik”, Wilhelm Ernst und Sohn, Berlin, 1960

[11] K. Reiersen, “Sveiseboka”, Universitetsforlaget, Oslo, 1995

[12] M. Merkel, K.-H. Thomas, “Taschenbuch der Werkstoffe”, FV Leipzig, 2000

[13] W. Rieder, “Hot Contacts Occuring on Switches and Bus-Bars”, CIGRE, Paris, Session 1956

[14] J. B. P. Williamson, “Deterioration Processes in Electriccal Connectors”, Proc. 4th intern. Conf. on Elec. Cont. Phen., Swansea, 1968, pp30 - 34

[15] J. Kulsetås, J. Sletbak, H. Kongsjorden, “Degradation of Electrical Contacts Caused by Oscillatory Micromotion Between the Contact Members”, IEEE Trans. Components, Hybrids, Manuf. Technol., CHMT-2 (1979), pp32 - 36

[16] M. Braunovic, “Power Connections”, Chapter 4 in IEEE Publication "Electric Contacts: Principles and Applications", 1999

[17] M. Runde, “Material Transport and Related Interfacial Phenomena in Stationary Aluminium Contacts”, Dissertation, Trondheim, Norway, Norw. Inst. of Technology, 1987

[18] M. Runde, E. Hodne, B. Tøtdal, “Current-induced aging of contact spots”, IEEE Holm Conference on Electrical Contacts (35 : 1989 : Chicago, Ill.)

[19] Å. Øberg et al. ,”The ageing physics of electrical contacts subjected to DC current”, Proceedings of the 42. IEEE Holm Conference on Electrical Contacts, 1996, pp 189 - 194

[20] D. A. Spera, “What is thermal fatigue?”, Thermal Fatigue of Materials and Components, ASTM STP 612, 1976, pp 3 -9

[21] M.M. Yovanovich, “Transient Heat Flow from a circular disk”, Progress in Astronautics and Aeronautics: Radiative Transfer and Thermal Control, Vol.49, p419, 1976

[22] R. Holm, “Die technische Physik der elektrischen Kontakte”, Springer, 1941

[23] M. Runde, A. Gjelsvik, a. Rein, “Method for Detecting Degraded Contacts in Gas Insulated Substations”, International Conference on Electrical Contacts, Nagoya 1994, pp 699 - 706

[24] T. Veijola, “Model for Thermal Spreading Impedance in GaAs MESFETS”, Electronics, Circuits, and Systems, 1996. ICECS '96., Proceedings of the Third IEEE International Conference on , Volume: 2 , 1996 , Page(s): 872 -875

[25] B. Hetnarski, “Basic Equations of the Theory of Thermal Stresses”, Thermal Stresses, Vol. I, North Holland, New York, 1986

[26] R. W. Hertzberg, “Deformation and Fracture Mechanics of Engineering Materials”, John Wiley, New York, 1995

[27] M. Kutz, “The Mechanical Engineers Handbook”, John Wiley &Sons, New York, 1998

[28] S. S. Manson, “Thermal Stress and Low-Cycle Fatigue”, McGraw-Hill, New York, 1966

[29] A. Kelly, R.B. Nicholson, “Strengthening Methods in Crystals”, Elsevier, Amsterdam, 1971

[30] J. D. Verhoeven, “Fundamentals of Physical Metallurgy”, John Wiley & sons, New York. 1975

[31] G. Gottstein, “Physikalische Grundlagen der Materialkunde”, Springer, Berlin, 1998

[32] W. v. Münch, “Werkstoffe der Elektrotechnik”, B. G. Teubner, Stuttgart, 1985

[33] A. Neumann, “Schweisstechnisches Handbuch für Konstrukteure”, DVS-Verlag, Düsseldorf, 1993

[34] Chr. Boller, T. Seeger, “Materials Data for Cyclic Loading”, Part D, Elsevier, 1987

[35] Almar-Naess, A., “Metalliske Materialer”, 3rd Edition, Tapir, 1993

[36] M. Runde, H. Kongsjorden, J. Kulsetås, B. Tøtdal, “Detection of a-spots in aluminium contacts”, IEEE Trans. Comp., Hybrids, Manuf. Techn. Vol. CHMT-9, pp 77 - 85, 1986

[37] M. Braunovic; N. Aleksandrov, ” Effect of electrical current on the morphology and kinetics of formation of intermetallic phases in bimetallic aluminum-copper joints”, 1993. Proceedings of the 39th IEEE Holm Conference on Electrical Contacts, pp.261-8

[38] P. C. Wingert, “Testing of the thermal-stress-cracking characteristics of silver-refractory contacts”, 1995. Proceedings of the 41st IEEE Holm Conference on Electrical Contacts, pp.338-45

[39] S. Kang, C. Brecher, “Cracking mechanisms in Ag-SnO_2 Contact Materials and their Role in the Erosion Process”, 1988, Proceedings of the 34th IEEE Holm Conference on Electrical Contacts,pp32-38

[40] J.B.P. Williamson, “The self healing effect: Its implications in the accelerated testing of connectors”, in Proc. Int. Conf. Electric Contact Phenomena, Budapest, 1980

[41] S. Flügge, “Electrical Conductivity”, Springer, Berlin, 1956

[42] H.-J. Mau, “Über die Schweisshaftkraft von ruhenden Kontakten bei Belastung durch einen Halbwellenstrom”, in “Kontakte der Elektrotechnik”, Akademie-Verlag, Berlin 1965

[43] T. M. Johnson, “Fatigue Life Prediction of Automotive-Type Load Histories”, Fatigue under complex loading, SAE 1977

[44] R. W. Hertzberg, “Deformation and Fracture Mechanics of Engineering Materials”, John Wiley & Sons, 1995

[45] H. Heiner, “Verschweissfestigkeit und Gefügeausbildung an der Berührungsstelle ruhender Starkstromkontakte bei hohen Strömen”, XI. Internat. Wiss. Koll. TH Ilmenau, 1966

[46] H. B. Cary, “Modern Welding Technology”, Prentice Hall, New Jersey, 1994

[47] Metals Handbook, Vol 2, ASM, Ohio, 1979